Transient, seasonal and inter-annual gravity changes

from GRACE data: Geophysical modelings

by

Ryoko Ogawa

Contents

List of Figures

List of Tables

Abstract

The Earth's gravity field reflects mass re-distribution on and in the Earth related to various processes related to hydrology, glaciology, seismology, oceanography, and so on. So far these gravity changes have been studied with gravity measurement at points on the ground, with relative gravimeters, absolute gravimeters, superconducting gravimeters, etc. . In contrast, satellite gravity observations make it possible to measure global gravity field with uniform accuracy. GRACE (Gravity Recovery and Climate Experiment) satellites, which were launched on March 2002, are composed of two identical satellites, and precise range measurements between them provide information on the gravity field. Because GRACE can measure global gravity field in a relatively short time, we can study its temporal variation.

GRACE mission has been producing scientific results on mass variations on seasonal and inter-annual timescales, e. g. seasonal terrestrial hydrological cycles in low latitude regions, melting of ice sheet and glaciers in high latitude regions. In this thesis, I discuss several kinds of gravity changes which have not been well investigated so far, and explore new possibilities of satellite gravity observations. With the results summarized below, I demonstrate that satellite gravimetry can be a new sensor for not only lithospheric dynamics but also for hydrospheric and cryospheric processes. This "new eye" to see time-variable gravity will help us solve complex geophysical phenomena in various time and spatial scales in the future.

(1) Co- and postseismic geoid height changes due to the 2004 Sumatra-Andaman Earthquake

The great Sumatra-Andaman Earthquake, 2004 December 26, ruptured the eastern boundary of the Indian Plate extending > 1000 km from Sumatra to the Andaman Islands. This earthquake has been studied with various approaches such as observations with seismometers, tsunami observations with tide gauges, crustal movement with Global Positioning System (GPS), and so on. Earthquakes generally cause gravity and geoid height changes by mass per-

turbations. Coseismic gravity/geoid changes due to the 2004 Sumatra-Andaman Earthquake were detected by satellite gravimetry, but little has been known on the geoid behavior after the earthquake. In this chapter, I mainly discuss postseismic geoid height changes found by our analysis. The change was characterized by a slow uplift with time constant of ~0.6 year. Postseismic gravity/geoid height changes are considered to be caused by three mechanisms; afterslip, viscous mantle relaxation, and pore fluid diffusion. The obtained postseismic geoid height changes cannot be explained with simple afterslip or viscous relaxation of Maxwellian upper mantle. In this study, the major mechanism is suggested to be the slow relaxation of coseismic dilatation and compression by the diffusion of supercritical H_2O abundant in the upper mantle.

(2) Acceleration terms in GRACE time-variable gravity and climate changes

Most of the past GRACE studies have modeled inter-annual gravity changes with linear variations, and little attention has been paid on the existence of quadratic terms, i.e. acceleration/deceleration of the gravity changes. Here I study such quadratic gravity changes and their link with the continental hydrological mass variations. On continents, time-variable gravity mainly originates from changes in soil moisture, which is the time integration of water fluxes, such as precipitation, evapo-transpiration and runoff. If these fluxes have linear trends, soil moisture would include quadratic changes. Hence temporal acceleration in gravity field provide information on climate changes, which is of grave importance in understanding the present-day global warming and in predicting the future. Here I solved for quadratic terms in the mass variations worldwide using the seven years of GRACE gravity data. Comparison of geographical patterns of the quadratic terms in GRACE data and hydrological model outputs showed intriguing agreement in major areas, which provides independent assessment as to the quality and validity of such hydrological models in inter-annual timescales.

(3) Seasonal and inter-annual gravity changes in Siberian permafrost from GRACE

Global warming causes gravity decreases in many places due to present-day melting of glaciers and ice sheets. Such changes in the ice mass on land, in turn, would cause global sea level rise. Recent warming is also known to degrade permafrost distributed over an extensive area in the central and eastern Siberia. Lena, Yenisei and Ob are the three largest Eurasian Arctic rivers running through that region. Hydrological dynamics in permafrost regions are peculiar because of the impermeability of frozen soil. Here I discuss gravity increases in the Lena, Yenisei, Ob river basins, comparing GRACE gravity data with observations of precipitation and river run-off in seasonal and inter-annual time scales. Significant inter-annual mass increases, comparable to a half of the glacial mass loss in Alaska, is found to occur in the three river basins over the last 7 years. It was found that the increase in precipitation is directly responsible for the increasing soil moisture there. The expanding water capacity in the permafrost might also be indirectly contributing to the gravity increase by making it possible to accommodate increasing water in soil. While the melting of glaciers and ice sheets on land contribute to sea level rise, Siberian permafrost might play a role to partially suppress this process by holding large amount of water.

Abstract

2002   3   17   GRACE (Gravity
Recovery And Climate Experiment)

GRACE

GRACE

(1) 2004
2004   12

GRACE

a

b   c

GRACE 1)

2) 0.6 (c)

(2)

GRACE

GRACE

GRACE

GRACE

GRACE

(3)

GRACE

30.7 Gt

GRACE

(   )

Acknowledgment

I would like to express my heartfelt gratitude to everyone who has helped and has encouraged me throughout the course of my study. First of all, my deepest appreciation goes to my supervisor, Prof. Kosuke Heki for valuable discussions, guidance, constant encouragement and patience all the time. He also assisted me to study in National Central University, Taiwan. During my stay in Taiwan, I always received his continued support.

Also, I would like to appreciate Prof. Benjamin F. Chao in National Central University, Taiwan for his guidance and valuable suggestions. I think that a lot of experiences in Taiwan have helped me to grow. I would like to thank Prof. Junji Koyama, Prof. Makoto Murakami, Prof. Kiyoshi Yomogida, Dr. Masato Furuya, Dr. Kazunori Yoshizawa and Dr. Youichiro Takada for their constructive comments. I have learned hydrology from many discussions with Prof. Ryuji Ikeda, Dr. Kazuhisa Chikita, Mr. Nobuto Nakatsukasa and Mr. Tomoyuki Wada. As for the study about Siberian permafrost, I received a lot of valuable comments from discussions with Prof. Atsuko Sugimoto (Graduate School of Environmental Science in Hokkaido Univ.). I am very grateful to Dr. David Garcia-Garcia, Dr. Haoming Yan and Dr. Zi-Zhan Zhang (National Central University, Taiwan) for valuable discussions. Also, I would like to appreciate all my colleagues in Earth Dynamics laboratory in National Central University and Space Geodesy laboratory in Hokkaido University for discussions and warm support.

I would like to thank JSPS fellowship for a grant that makes it possible to complete this study. I wish that this environment that Ph.D. students concentrate on their research without financial instability will be maintained or be better in the future. Finally, I would like to express my heartfelt gratitude to my family and my friends for their understanding and warm encouragement at all times.

1 Introduction

1.1 Geophysical implications of gravity studies in earth sciences

Geodesy deals with the shape, size, rotation, and gravity field of the Earth. Since our planet is composed of various materials with non-uniform distribution, its gravitational field shows local variations known as gravity anomaly. These variations can help us explore subsurface mass distribution, and let us look into the interior of the Earth. Temporal variations in the gravity field partly come from tidal forces from the Moon, Sun, and nearby planets. They are also caused by the redistributions of masses on or within the Earth. For example, temporal gravity changes arise by the seasonal changes of terrestrial water storage in hydrological systems. Gravity also changes by the movement of the Earth's rotational axis, mass redistribution in the interior of the Earth, melting of glaciers and ice sheets, and so on. To know the time-variable gravity field enables us to study various aspects of dynamics of the Earth.

As conventional ways of gravity measurement on the ground, there are relative gravimeters, absolute gravimeters (AG), and superconducting gravimeters (SG) [Fig. 1.1]. These measurements have different characteristics and are used for various purposes. Relative gravimeters use precise springs and can measure local gravity fields accurate to $10\mu gal$. They have an advantage of being inexpensive and portable. AG directly measures accelerations of an object during its free fall in vacuum. Its accuracy is better than $1\mu gal$. AG has been used mainly to calibrate relative gravimeters, but its direct geophysical application has been explored. For example, AG could observe the movement of magma by nearly continuous measurements at a fixed point near active volcano [e.g. Kazama and Okubo, 2009]. The most accurate relative gravimeter is SG. It has a sensitivity to gravity changes on the order of $1ngal$. SG is suitable for long-term observations of e.g. the Earth's background free oscillations [Nawa et al., 1998] because of its high stability over

time. Such conventional gravimetry techniques are useful to understand gravity changes at a fixed point occupied by the gravimeter. In contrast, satellite gravity observations make it possible to monitor gravity field in a relatively short time with a uniform accuracy over the whole globe.

Fig. 1.1: Ground-based gravimeters. There are relative gravimeters (left), absolute gravimeters (AG) (middle) and superconducting gravimeters (SG) (right)

1.2 History of satellite gravity observations

If forces acting on a satellite were only the gravitational force from the central body which is a smooth sphere composed of uniform materials, the satellite would remain in a fixed orbit following the Kepler's laws. However, our planet is neither smooth nor homogeneous, and deviate from a sphere. Spatial and temporal variations in the Earth's gravity field let the orbital elements slowly evolve in time [Kaula, 1966]. Since the Sputnik 1 was launched in 1957, the gravity field of the Earth has been observed by monitoring such changes in the orbital elements of satellites. The first result of satellite gravity observation was made by the Vanguard 1 in 1958; they precisely determined the J_2 term, which shows the Earth's dynamic oblateness. In the 1980s, satellite laser ranging (SLR) technique was used to constrain low degree components of the Earth's gravity

field and their temporal variations. For example, SLR detected the secular decrease of the J_2 term [Yoder et al., 1983]. In the 1990's, Nerem et al., [1993] estimated monthly values of the J_2 and J_3 terms with SLR. Also, SLR found that the secular decrease of J_2 slowed down suddenly around 1998 [Cox and Chao, 1998]. However, SLR is not accurate enough to constrain changes of higher degrees in the Earth's gravity. In 2000s, satellites dedicated to the measurement of the Earth's gravity field were launched to study the gravity field with high spatial and time resolutions. GRACE, one of the satellite gravity missions, was launched on 17 March 2002 by American and German space agencies.

1.3 The GRACE mission

The primary objective of the GRACE mission is to obtain accurate estimates of the mean and time-variable components of the Earth's gravity field variations [Bettadpur, 2003]. For this purpose, two identical satellites were put into a polar, near circular orbit at 500km altitude with the inter-satellite separation of $\sim$ 220km [Fig. 1.2].

According to the mechanical energy conservation theory, the sum of the gravity satellite's kinetic energy and the potential energy is conserved,

$$\frac{1}{2}m\Delta v^2 = -\Delta U, \tag{1.1}$$

where m is mass, v is the satellite velocity and U is the gravity potential. Actual quantity observed by GRACE is the range rate between the two satellites, which contains information on the gravity field. Non-gravitational forces, such as air drag, are measured on each satellite using a high accuracy electrostatic, room-temperature accelerometer. The satellite positions are precisely measured using on-board GPS receivers. GRACE can map the global gravity field every 30 days with
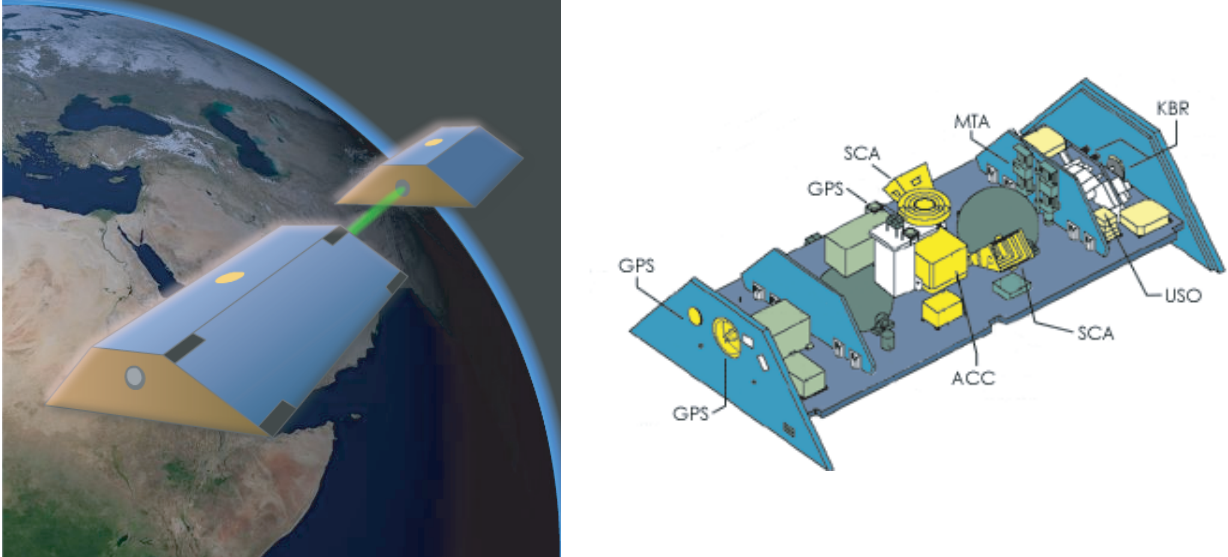
Fig. 1.2: Image of GRACE (left). GRACE consists of two identical satellites coorbiting at polar orbits as high as ~450km, with the separation of ~220km. (right) A GRACE satellite has a senser to measure inter-satellites distances with K-band microwave (KBR), a GPS receiver for orbit determination, and an accelerometer to correct for air drags. (http://www.csr.utexas.edu/GRACE/publications/brochure/page11.html)

a spatial resolution of a few hundreds of kilometers with the *μgal* level accuracy. This satellite mission also made it possible to quantify time-variable gravity field globally, which is important for understanding on-going redistributions of masses in and on the Earth. Until now, GRACE has detected various types of mass redistribution signals relevant to various research fields in Earth sciences.

1.4 Recent studies with GRACE time-variable gravity data

Various studies of time-variable gravity changes have been published by many researchers since GRACE was launched. Such changes cover seasonal to inter-annual timescales, and reflect the mass re-distribution on/in the Earth related to hydrology, glaciology, seismology, oceanography, and so on [Table. 1]. Early scientific results of GRACE data include seasonal hydrological cycles

	Seasonal	Inter-annual	Transient
Place	World wide (e.g. Amazon, Congo) Ocean	Arctic regions (e.g. Alaska) Ice sheets (e.g. Canada) Ocean	Sumatra Equatorial regions
Sources	Hydrology Mass redistribution	Ice melting Glacial isostatic adjustment Mass changes	Earthquake ENSO

Table. 1: Past studies by GRACE gravity data

in the tropical South America which showed good agreement with a hydrological model [Tapley et al., 2004]. Seasonal gravity changes on land are dominated by hydrology [e.g. Strassberg et al., 2007, Chen et al., 2007a]. In addition to seasonal changes, longer-term gravity changes come to be detected in various regions. They include present-day melting of ice sheet in the coastal area of Greenland [e.g. Luthcke et al., 2006], mass losses of the mountain glaciers in Alaska [e.g. Chen et al., 2006] and in Asian high mountains [Matsuo and Heki., 2010]. Morishita and Heki [2008] recently detected transient deviation from average seasonal gravity changes due to precipitation anomalies associated with ENSO (El Nino and Southern Oscillation) episodes.

GRACE detected not only hydrological signals but also those from solid Earth, such as secular gravity increase by glacial isostatic adjustments (GIA) in northern North America [Tamisiea et al, 2007] and in northern Europe [Steffen et al., 2009]. Faulting in an earthquake is associated with mass redistribution, and is expected to modify gravity field. Han et al., [2006] detected coseismic gravity changes due to the 2004 Sumatra-Andaman Earthquake by GRACE for the first time. Gravity changes also occurs as the ocean bottom pressure changes. GRACE has an advantage that it can detect sea water mass changes directly, while other techniques such as satellite altimetry measures the combined effect of steric changes (e.g. thermal expansion) and mass vari-

ations. Chambers [2006] compared GRACE data with seasonal steric sea level variations derived by altimetry. Recently, sea level rise signals were found in GRACE as the increase in the total mass of the oceans [Cazenave et al., 2009].

1.5   The objective of this study

In this study, I discuss several kinds of gravity changes which have not been adequately studied before, and explore new possibilities of satellite gravity observations. The contents of the chapters in this thesis are summarized as follows;

Chapter 2: Data and processing. GRACE gravity data are processed at three analysis centers, and monthly data sets are periodically released on their web sites. Here I will describe how to calculate time-variable gravity changes from such data sets, and how to reduce their noises with various kinds of filters.

Chapter 3: Coseismic/postseismic geoid height changes due to the 2004 Sumatra-Andaman Earthquake. Coseismic gravity changes due to the 2004 Sumatra-Andaman Earthquake were detected with the GRACE data by Han et al. [2006]. Here I will show postseismic changes occurred as well as coseismic changes, and will discuss how postseismic gravity changes occurred. This part of the study has been already published in Ogawa and Heki [2007].

Chapter 4: Acceleration signals in GRACE time-variable gravity. Past GRACE studies have modeled interannual gravity trends as linear changes. Little attention has been paid to the existence of quadratic changes which is responsible for acceleration/deceleration of the gravity changes. Here I will discuss geophysical implications of quadratic signals in the GRACE data.

Chapter 5: Seasonal and inter-annual gravity changes in the Siberian permafrost region. While gravity signals in high latitude regions often show decreases, the Siberian permafrost region show a steady increase in gravity. Here I will discuss mechanisms responsible for the gravity increase

there.

Chapter 6: Here I will summarize the study.

2 Data and Processing

2.1 Data

Processing and archiving of GRACE data are performed in a shared Science Data System (SDS) between the Jet Propulsion Laboratory (JPL), USA, the University of Texas Center for Space Research (UTCSR), USA, and the GeoForschungsZentrum Potsdam (GFZ), Germany. GRACE raw observation data include gravity changes caused by changes in the atmosphere and oceans as well as those on the surface of the Earth. The non-tidal variabilities in the atmosphere and oceans are removed using the ECMWF atmospheric model and a baroclinic or barotoropic ocean model driven by this atmospheric model [Bettadpur, 2007]. After these removals, time-variable gravity signals on land become evident, and these signals have been linked to mass transports on or in the Earth.

GRACE time-variable gravity data are composed of the coefficients of spherical harmonic expansion (Stokes' coefficients) of the global gravitational potential [Fig. 2.1]. I use the Level-2 Release-04 data sets from the UTCSR [Bettadpur, 2007], spanning 2003/01 – 2008/12 given in the form of monthly sets of Stokes' coefficients up to degree and order 60 (http://podaac.jpl.nasa.gov/ grace/data_access.html). Changes in gravity anomaly Δg and geoid height Δh can be expressed as the different kinds of summation of spherical harmonics as shown in eq. (2.1) and (2.2). By assuming that gravity changes are only due to change in the thickness of surface water [Fig. 2.2], $\Delta water$, equivalent water thickness (EWT), can be calculated with eq. (2.3) [Wahr et al., 1998, Chao, 2005].

$$\Delta g(\theta, \phi, t) = \frac{GM}{R^2} \sum_{n=2}^{n_{max}} (n-1) \sum_{m=0}^{n} (\Delta C_{nm}(t) \cos m\phi + \Delta S_{nm}(t) \sin m\phi) P_n^m(\cos \theta) \qquad (2.1)$$

$$\Delta h(\theta, \phi, t) = R \sum_{n=2}^{n_{max}} \sum_{m=0}^{n} (\Delta C_{nm}(t) \cos m\phi + \Delta S_{nm}(t) \sin m\phi) P_n^m(\cos \theta) \qquad (2.2)$$

$$\Delta water(\theta, \phi, t) = \frac{R\rho_e}{3\rho_w} \sum_{n=2}^{n_{max}} \frac{2n+1}{1+k_n} \sum_{m=0}^{n} (\Delta C_{nm}(t) \cos m\phi + \Delta S_{nm}(t) \sin m\phi) P_n^m(\cos \theta) \qquad (2.3)$$

The coordinate systems (θ, ϕ, t) means (colatitude, longitude, time), R is the Earth's equatorial radius. GM is the product of the gravitational constant and the mass of the Earth. The integers n and m denote the degree and order, respectively. $P_n^m(\cos \theta)$ represents the fully normalized associated Legendre functions. $\Delta C_{nm}(t)$ and $\Delta S_{nm}(t)$ are the deviations from the static Stokes' coefficients, and contain integrated signals from all un-modeled gravity effects on/in the Earth. In the eq. (2.3) to calculate EWT, ρ_e and ρ_w are the mean density of the Earth (5517 kg m^{-3}) and that of fresh water (1000 kg m^{-3}), respectively. k_n is the load Love number of degree n, which is to correct for the elastic yielding of the Earth. EWT is often used in discussing geophysical implication of gravity changes by comparing with meteorological quantities.
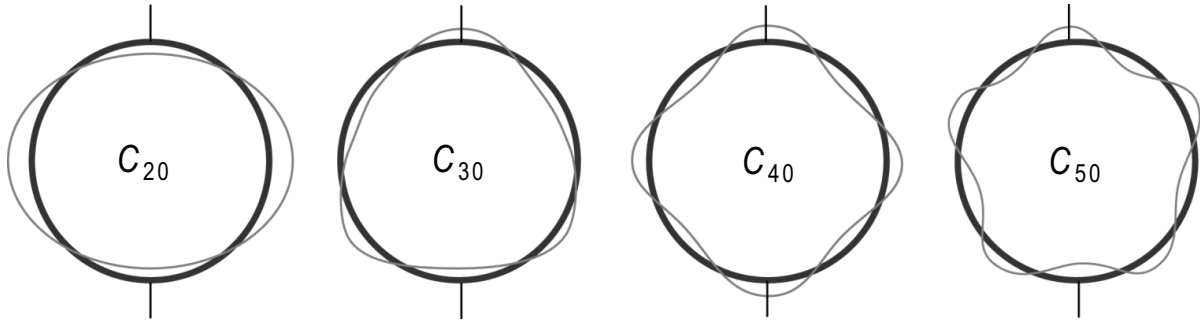
Fig. 2.1: Schematic view of the Stokes's coefficients [Heki, 2007]. Monthly sets of Stokes' coefficients up to degree and order 60 are provided.

C_{20} represents the Earth's oblateness, and this component can be only poorly constrained with the GRACE data [Fig. 2.3]. C_{20} values are replaced by those derived from the SLR observations [Cheng and Ries, 2007].
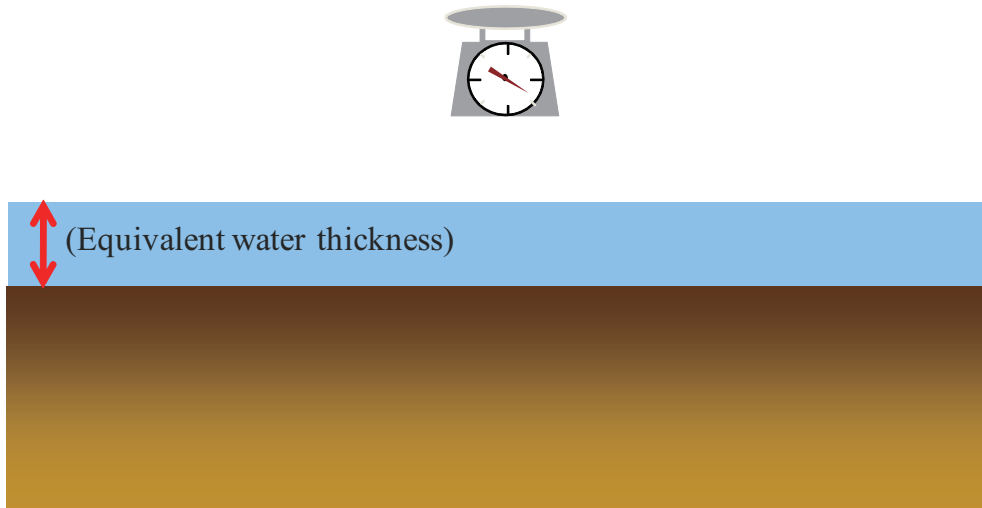
Fig. 2.2: Schematic view of equivalent water thickness. Equivalent water thickness can be converted from the GRACE data taking account of the elastic response of the Earth using the load Love number. Equivalent water thickness is useful in interpreting gravity changes as changes in soil moisture.
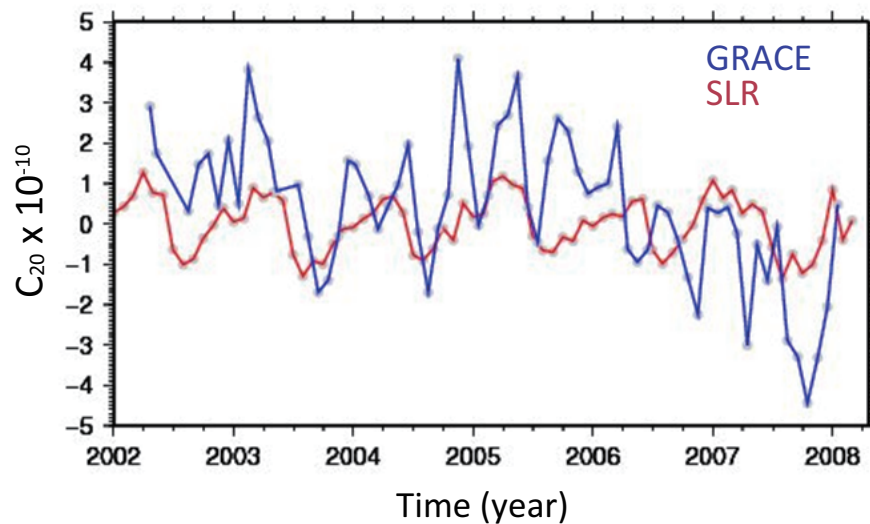
Fig. 2.3: Time-series of C_{20} from GRACE and SLR. C_{20} from GRACE is from UTCSR RL-04 Level-2 data. C_{20} value from SLR is obtained from Cheng and Ries, [2007]. In this study, I adopt C_{20} from SLR because their behaviors are more stable than those from GRACE.

2.2   Spatial filtering

GRACE data are known to suffer from correlated errors and short-wavelength noises, which makes

spatial filtering indispensable. In the maps of gravity changes [Fig. 2.4 (a)] and equivalent water

thickness [Fig. 2.4 (c)], short wavelength components are enhanced due to the factors $(n - 1)$ or

$(2n + 1)$ shown in eq. (2.1) and eq. (2.3). On the other hand, the map of geoid height changes

[Fig. 2.4 (b)] highlights lower degree components. All these maps show correlated errors as

represented by longitudinal stripes. This result suggests a certain kind of correlation among the

Stokes' coefficients in the GRACE data [Swenson and Wahr, 2006].

Here are some examples of Stokes' coefficients as a function of degrees for fixed orders [Fig.

2.5]. Correlations do not appear on the Stokes' coefficients for lower orders. On the other hand,

significant correlations can be found in the coefficients with the order m of 6-7 or higher [Fig.

2.5]. The plot of the Stokes' coefficients shows that groups of coefficients with even degrees or

odd degrees are correlated within the groups, but there are no correlations between the two groups.

In this study, I reduced such noises following the method by Swenson and Wahr [2006]. In this

method, for a given Stokes' coefficient of order 6 and above, I fit the even and odd coefficients with

least-squares method using degree 4 polynomials as shown in Fig. 2.6. I then took the differences

from these polynomials as the true coefficients. This is referred to as the "P4M6" de-striping filter

in Chen et al. [2007b].

When this step is applied to Fig. 2.4 (c), correlated noises (longitudinal stripes) are reduced

efficiently as shown in Fig. 2.7. This step can be used in gravity and geoid height changes as well.

However, relatively strong correlated errors still appear in low latitude regions. Random noises in

the GRACE data become larger for higher degrees. We can mitigate this problem by applying the

anisotropic fan filter which consists of low-pass filters along both the degree n and order m, using
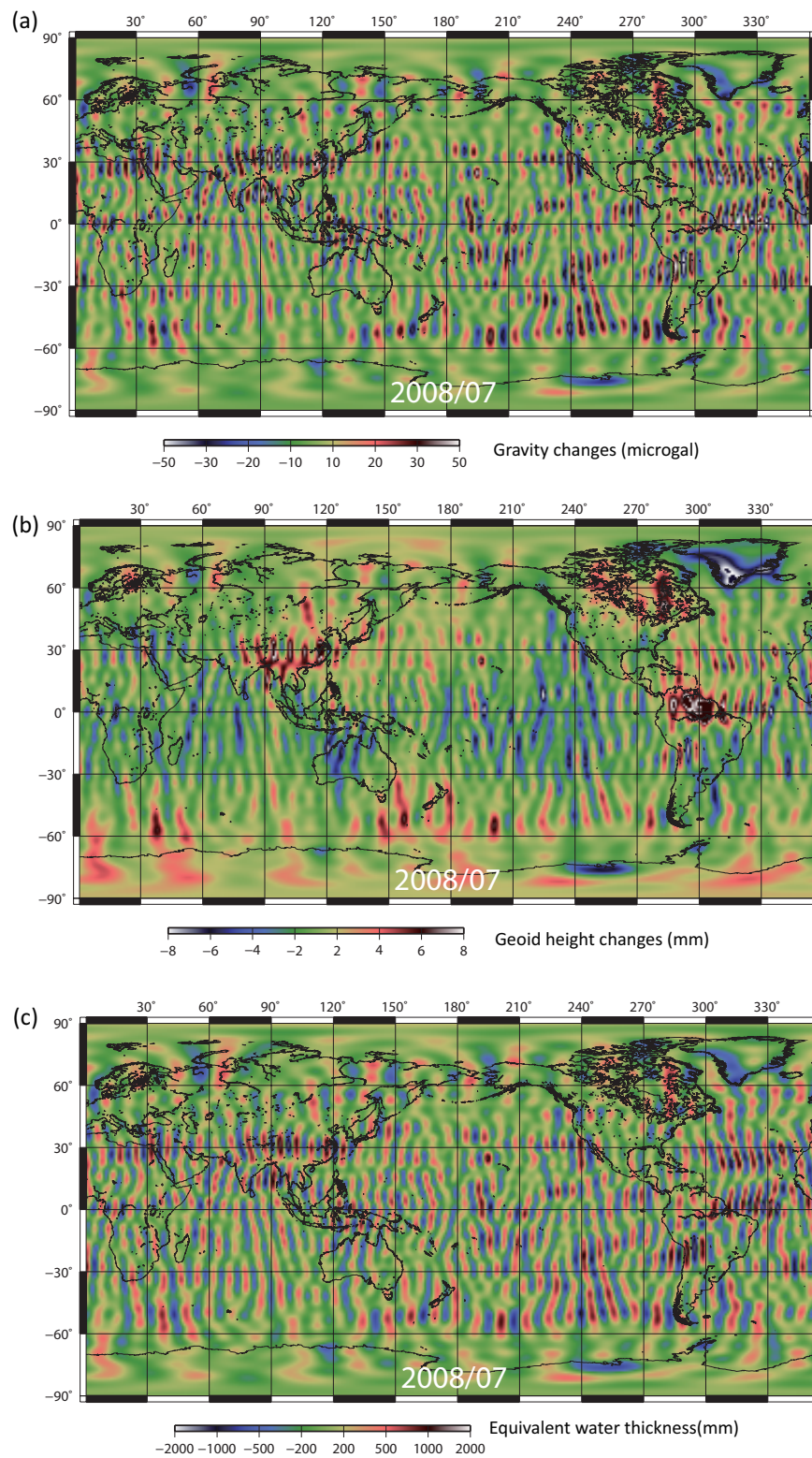
Fig. 2.4: Changes in gravity (a), geoid height (b) and equivalent water thickness (c) in July 2008 drawn without spatial filtering. In all maps the correlated errors appear as longitudinal stripes.

the following equations instead of eq. (2.1), (2.2) and (2.3) [Zhang et al., 2009]:

$$\Delta g(\theta, \phi, t) = \frac{GM}{R^2} \sum_{n=2}^{n_{max}} (n-1)W_n \sum_{m=0}^{n} W_m(\Delta C_{nm}(t) \cos m\phi + \Delta S_{nm}(t) \sin m\phi)P_n^m(\cos \theta) \qquad (2.4)$$

$$\Delta h(\theta, \phi, t) = R \sum_{n=2}^{n_{max}} W_n \sum_{m=0}^{n} W_m(\Delta C_{nm}(t) \cos m\phi + \Delta S_{nm}(t) \sin m\phi)P_n^m(\cos \theta) \qquad (2.5)$$

$$\Delta water(\theta, \phi, t) = \frac{R\rho_e}{3\rho_w} \sum_{n=2}^{n_{max}} W_n \frac{2n+1}{1+k_n} \sum_{m=0}^{n} W_m(\Delta C_{nm}(t) \cos m\phi + \Delta S_{nm}(t) \sin m\phi)P_n^m(\cos \theta). \qquad (2.6)$$

W_n and W_m are the filter weights for coefficients of degree n and order m, respectively. Filter weights is defined as follows [Jekeli, 1981, Wahr et al., 1998]:

$$W_0 = 1 \qquad (2.7)$$

$$W_1 = \frac{1 + e^{-2b}}{1 - e^{-2b}} - \frac{1}{b} \qquad (2.8)$$

$$W_{n+1} = -\frac{2n+1}{b}W_n + W_{n-1} \qquad (2.9)$$

$$b = \frac{\ln(2)}{(1 - \cos(r/a))}, \qquad (2.10)$$

where a is the radius of the Earth, r is the averaging radius. Different averaging radius changes filter weights [Fig. 2.8]. By eq. (2.4), (2.5) and (2.6), clear time-variable gravity fields can be obtained [Fig. 2.9]. All maps show similar patterns, but it is obviously seen that geoid height changes show lower degree components with larger weights [Fig. 2.9 (b)].
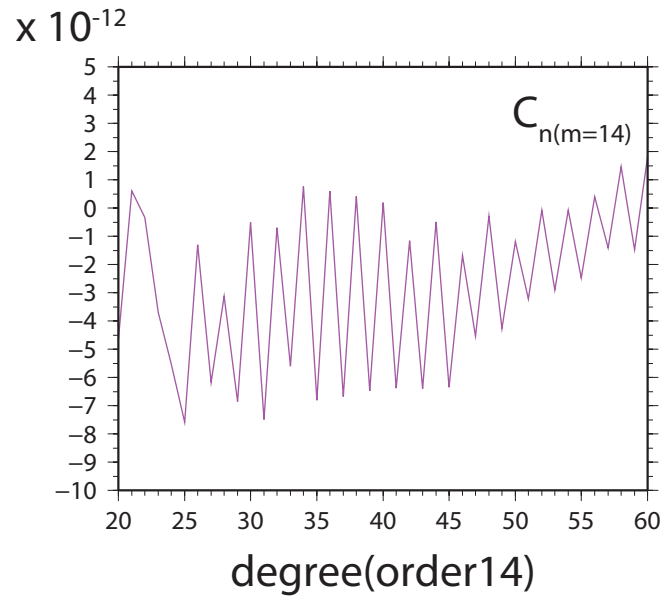
Fig. 2.5: Stokes' coefficients C_{nm}, as a function of degrees n for the order $m = 14$. Correlation of coefficients of every other degree is strong for higher degrees, although it is not seen in lower degrees.
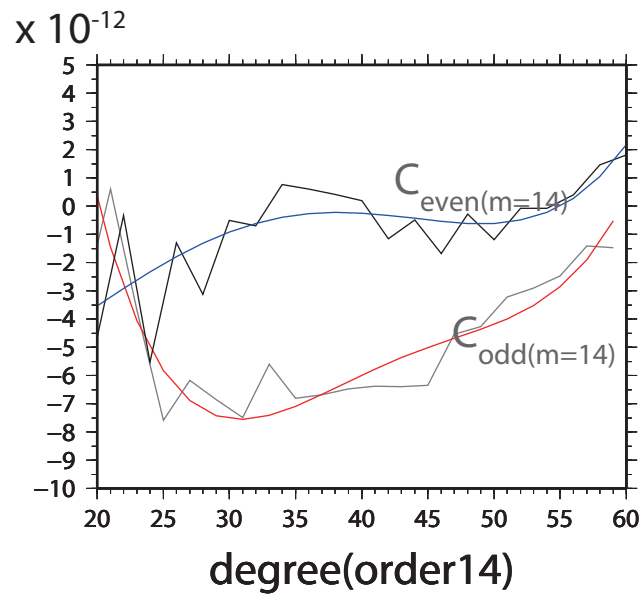
Fig. 2.6: Stokes coefficients C_{nm}, as a function of degrees n for the order $m = 14$. Coefficients are plotted separately for coefficients with even and odd degrees. Blue and Red solid curves are modeled with polynomials of degree 4.
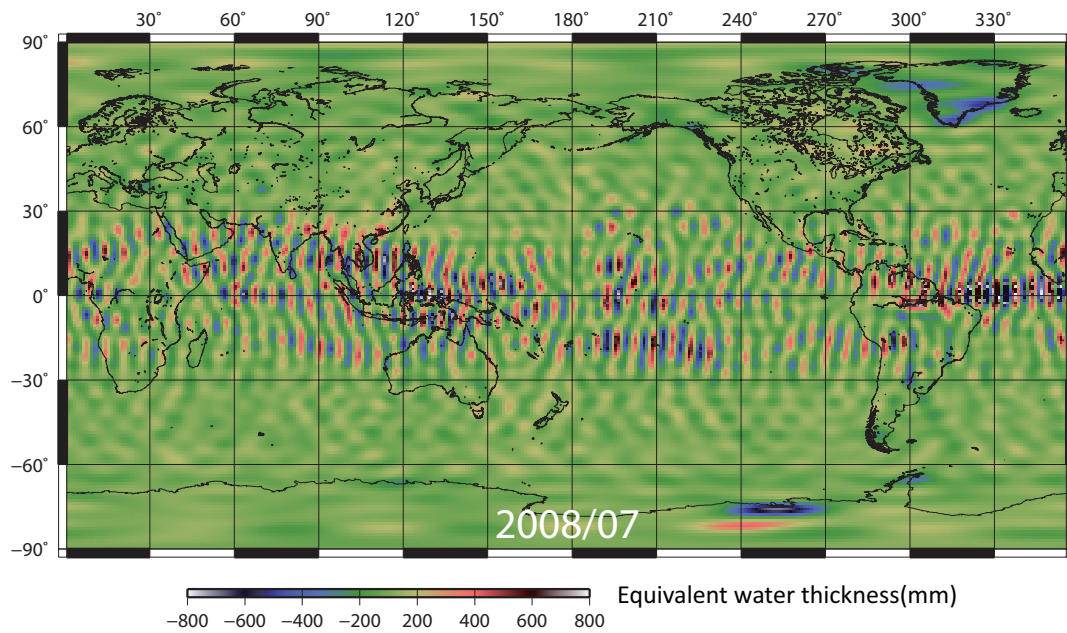
Fig. 2.7: Equivalent water thickness after applying the destriping filter of Swenson and Wahr [2006].
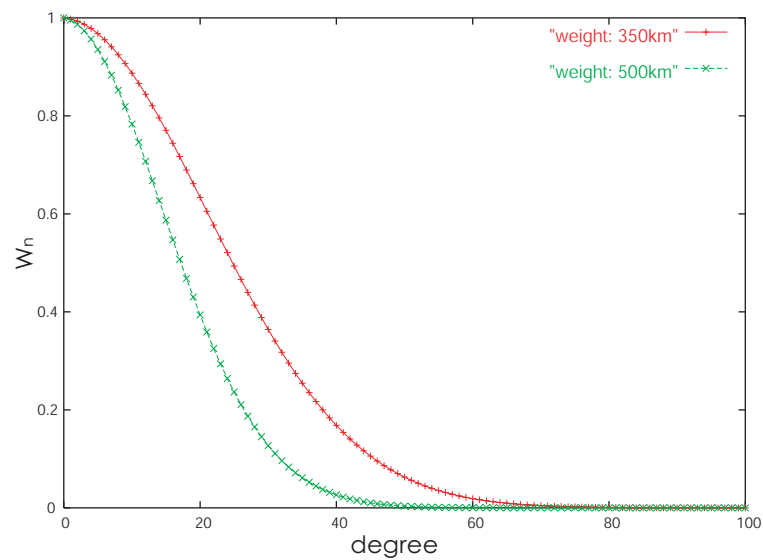
Fig. 2.8: Spherical harmonic coefficients W_n of isotropic Gaussian filters with the averaging radius of 350km (red) and 500km (green), respectively, used for spatial averaging of the GRACE data.
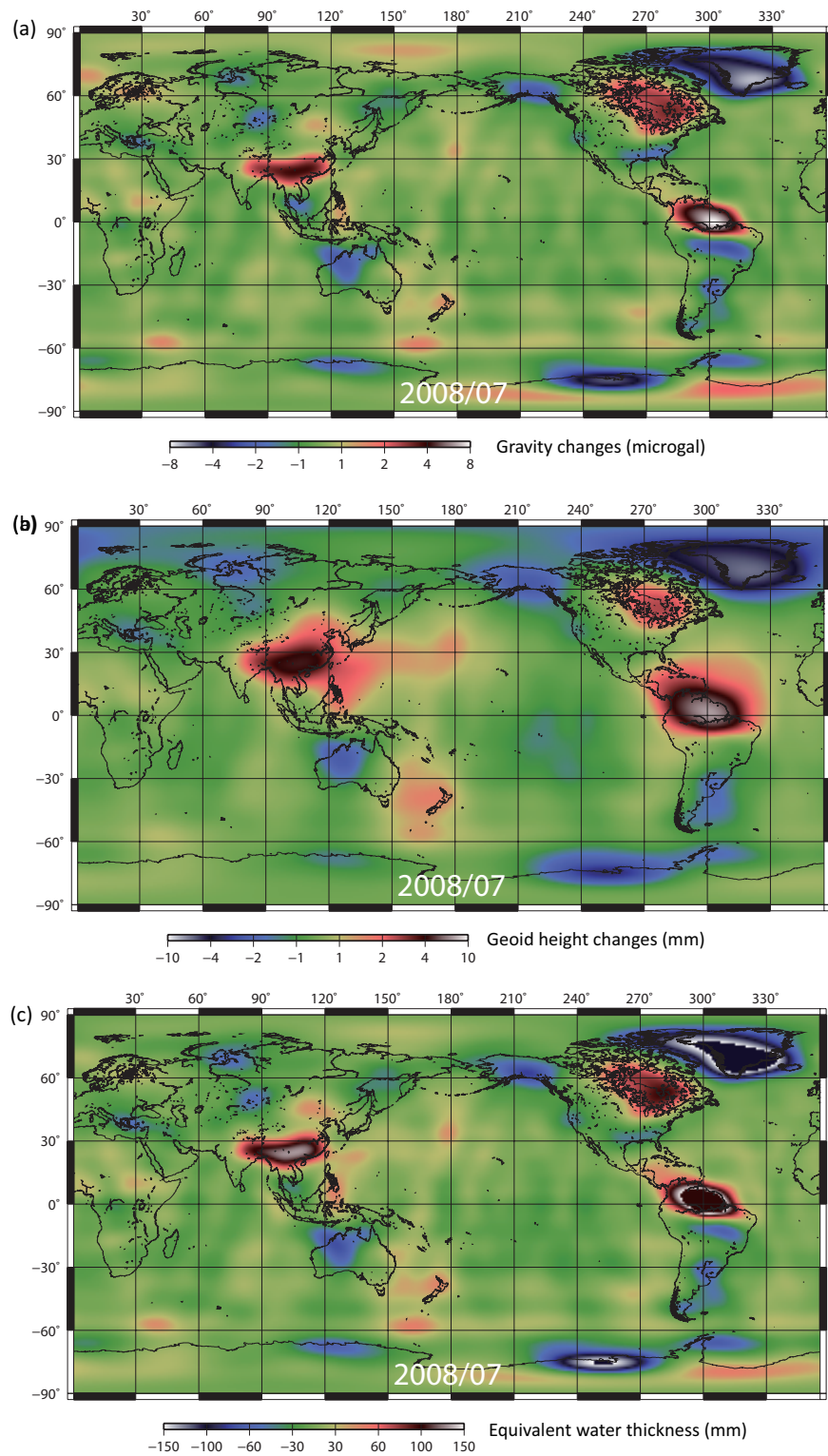
Fig. 2.9: Changes in (a) gravity, (b) geoid height, (c) equivalent water thickness after applying both the destriping filter and the 500km fan filter

2.3 Time series analysis

As mentioned in Chapter 1, the Earth's gravity field reflects the mass re-distribution on and in the Earth on various timescales. There are gravity changes in longer timescales than seasonal. They are called sometimes as "inter-annual" changes and other times as "secular" changes. Secular changes often means changes whose rate does not change during the observation period. In the gravity changes, they are associated with dynamics of the interior of the Earth, e.g. Glacial isostatic adjustments (GIA), true polar wander (TPW). In hydrology and climatology, rate of such changes often varies within the observation period, and we generally call them as "inter-annual" changes. As for processes discussed in this thesis, they are gravity changes coming from hydrological and glaciological processes, and I refer to them as "inter-annual" changes.

To discuss seasonal or inter-annual changes, the time-series of gravity at a given location (or a grid point on the global map) obtained by eq. (2.4), (2.5) or (2.6) is analyzed using the following expression with parameters (a_0, a_1, t_0, b_a, b_s, θ_a, θ_s):

$$Mass(t) = a_0 + a_1(t - t_0) + b_a \sin(\omega t + \theta_a) + b_s \sin(2\omega t + \theta_s), \qquad (2.11)$$

where the last two terms represent the seasonal components (annual and semi-annual, respectively). When we map seasonal changes, we discuss parameters b_a and b_s estimated by the least-squares method at each point. On the other hand, when we discuss inter-annual trends, a_1 should be mainly discussed. By following this standard method, seasonal changes in equivalent water thickness have been obtained [Figs. 2.10, 2.11]. Seasonal gravity and geoid height changes can be calculated by this method as well. In Figs. 2.10, 2.11, it is clear that seasonal hydrological cycles govern gravity changes in low-latitude regions. In addition, Fig. 2.12 shows the distribution of a_1, inter-annual trends in gravity, geoid height, and equivalent water thickness, respectively. These

maps suggest that present-day melting of glaciers and ice sheets predominates gravity decreases in high-latitude regions. Secular gravity changes due to GIA are seen in Canada and Scandinavia. Thus, various kinds of the gravity changes can be made visible with this method. Here I discuss several kinds of gravity changes by this method. Furthermore, I will evaluate the performance of eq. (2.11) with the GRACE data, and propose an alternative model later in the following chapters.
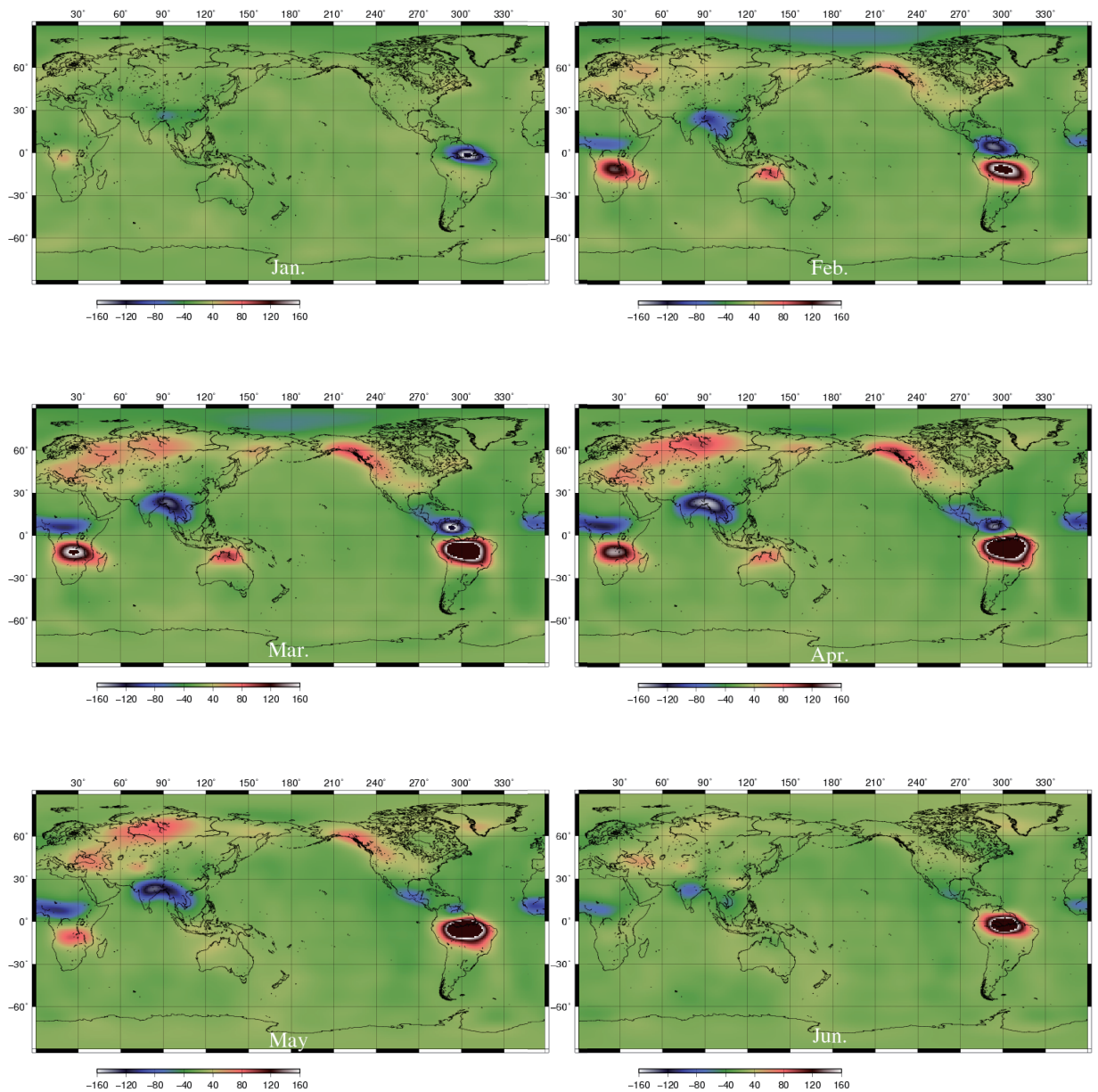
Fig. 2.10: Seasonal changes in equivalent water thickness (mm) from January to June. A 500-km fan filter and de-striping filter applied. In low latitude regions, large amplitude signals are seen due to seasonal hydrological cycles of terrestrial water storage.
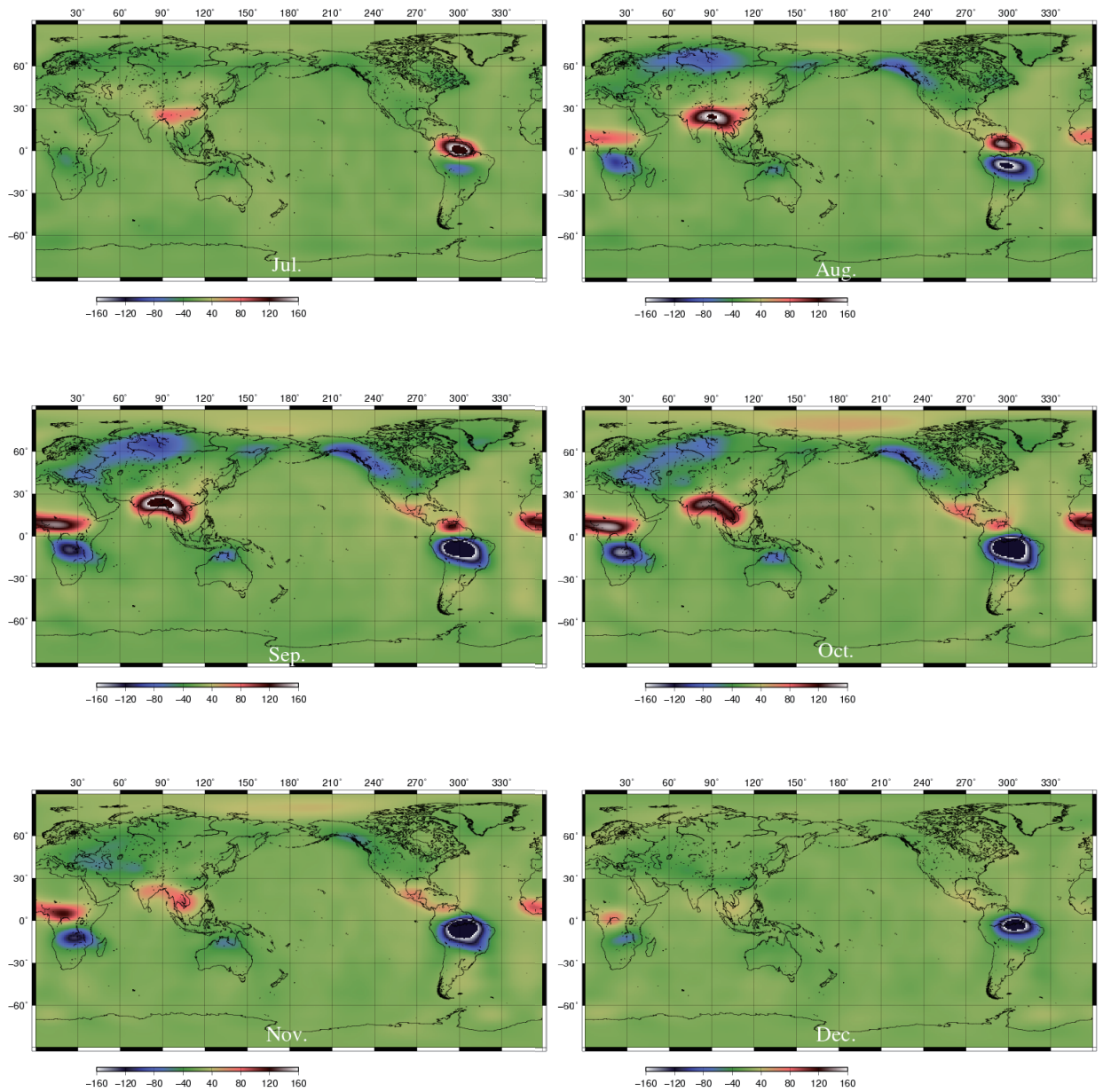
Fig. 2.11: Seasonal changes in equivalent water thickness (mm) from July to December.
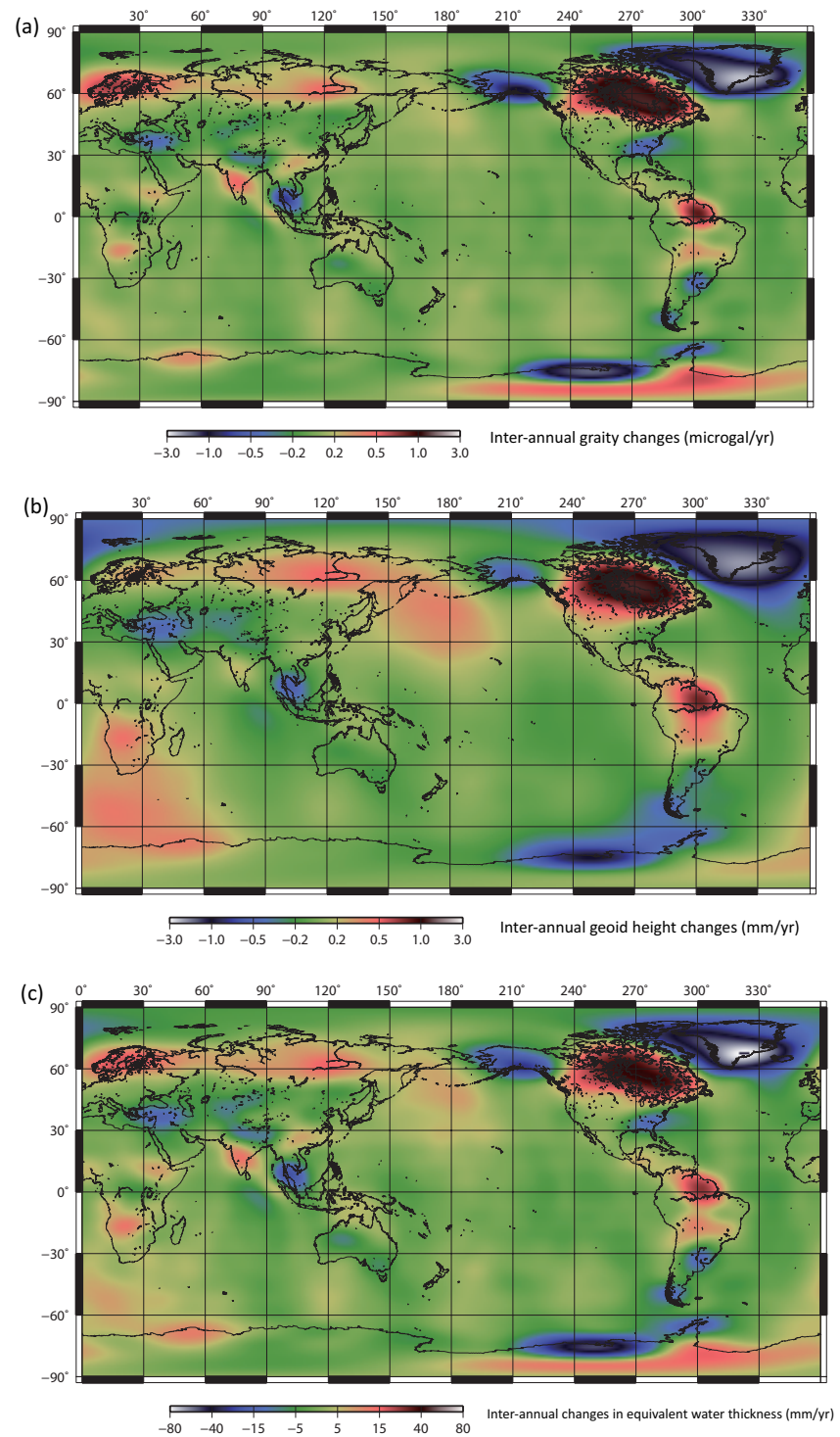
Fig. 2.12: Inter-annual trends in (a) gravity (microgal/yr), (b) geoid height (mm/yr), (c) equivalent water thickness (mm/yr). A 500-km fan filter and de-striping filter have been applied.

3 Coseismic/postseismic geoid height changes due to the 2004 Sumatra-Andaman Earthquake

3.1 Introduction

The great Sumatra-Andaman Earthquake, 26 December 2004, ruptured the eastern boundary of the Indian Plate, extending >1000 km from Sumatra to the Andaman Islands, and caused devastating tsunami in the Indian Ocean. This earthquake has been studied by various approaches such as the Earth's free oscillations amplitudes [Park et al., 2005], array analysis by Hi-net in Japan [Ishii et al., 2005], analysis of seismic body waves and surface waves [Ammon et al., 2005], tsunami observations by tide gauges [Tanioka et al., 2006], tsunami signatures in satellite altimetry [Hirata et al., 2006], crustal movement with Global Positioning System (GPS) [Vigny et al., 2005], ionospheric disturbances [Heki et al., 2006], and resonant coupling between lithosphere and atmosphere [Choosakul et al., 2009].

Earthquakes cause changes in gravity and geoid height by two kinds of mass distribution perturbations; uplift and subsidence of the ocean floor and Moho cause deformation of layer boundaries with density contrasts, and coseismic dilatation and compression of crustal and mantle rocks cause the density changes of constitutive materials [Fig. 3.1]. Gravity measurements would help us understand what goes on at depth as a new sensor in seismology. However, it has been difficult to detect coseismic gravity changes because of low accuracy and discontinuity of conventional ground gravity measurements.

Meanwhile, a network of superconducting gravimeter (SG) stations and satellite gravimetry made it possible to detect coseismic gravity changes. Coseismic gravity change was detected for the first time in the 2003 Tokachi-oki earthquake by an SG array in Japan [Imanishi et al.,
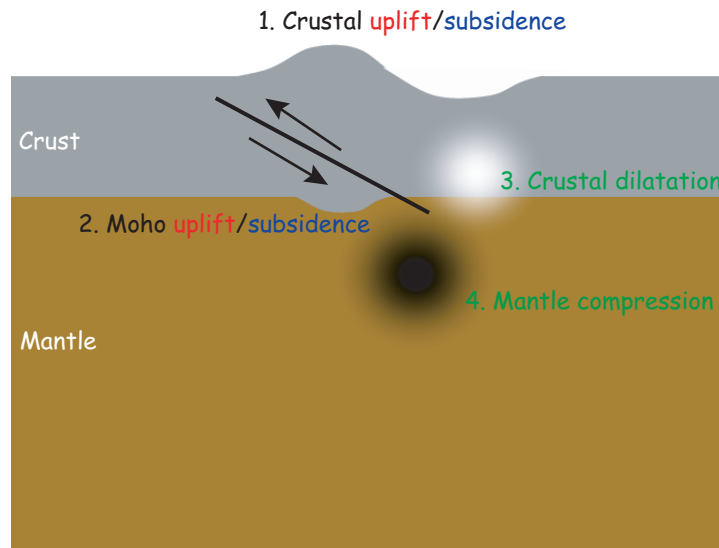
Fig. 3.1: Schematic of coseismic gravity changes. Dislocation at a fault causes the deformation of layer boundaries with density contrasts. Also, coseismic dilatation and compression cause the density changes of rocks.

2004]. With the GRACE data, Han et al., [2006] detected coseismic gravity changes due to the 2004 Sumatra-Andaman earthquake for the first time. Recently, possible detections of coseismic gravity changes were reported by SG [e.g. Nawa et al., 2009; Imanishi et al., 2009]. However, what happens in gravity/geoid height "after" an earthquake has not been known at all. In this chapter, I try to detect postseismic gravity changes associated with the 2004 Sumatra-Andaman earthquake with GRACE, and discuss their mechanisms.

3.2 Observations with GRACE

By the data and method described in Chapter 2, monthly geoid height at an arbitrary point can be calculated by eq. (2.5). Here 350 km averaging radius is applied. In order to discuss coseismic and postseismic gravity changes, I add two earthquake-related parameters to eq. (2.11): (1) coseismic offset of the geoid height a_7, and (2) postseismic slow geoid height change a_6, as follows:

$$h_{before}(t) \equiv a_0 + a_1(t) + b_a \sin(\omega t + \theta_a) + b_s \sin(2\omega t + \theta_s) \tag{3.1}$$

$$h_{after}(t) \equiv a_0 + a_1(t) + b_a \sin(\omega t + \theta_a) + b_s \sin(2\omega t + \theta_s)$$
$$+a_6(1 - \exp(-\frac{t - t_e}{\tau}) + a_7, \tag{3.2}$$

where h_{before}(t) and h_{after}(t) mean the geoid heights before and after the earthquake, respectively. t_e is the occurrence time of the earthquake, and $t - t_e$ shows the time after the earthquake. Fig. 3.2 shows the time series of geoid height at (a) a point in the Andaman Sea and (b) another point around the Andaman Islands. To retrieve signals related to the earthquake, inter-annual and seasonal changes which are expressed as a_0, a_1, b_a, b_s should be estimated using the part of the data set not affected by the earthquake. We then removed these non-seismic parts from Figs. 3.2 (a) and (b), and estimated coseismic offset a_7 and postseismic geoid height changes a_6 [Figs. 3.2 (c) (d)]. A large coseismic subsidence is observed in geoid at the point in the Andaman Sea [Fig. 3.2 (c)]. Fig. 3.2 (d) shows that the coseismic vertical movement at the other point was smaller, but a large postseismic change was found to last for a half year or longer there. The trend of the change is positive (postseismic geoid upheaval), and the time constant τ of ~0.6 year resulted in the best fit.

Then, I applied eq. (3.1) and eq. (3.2) to 1×1 degree gridded map to estimate the distribution of coseismic and postseismic geoid height changes [Fig. 3.3]. In order to stabilize the solution, the time constant of the decay of the postseismic changes τ is fixed to 0.6 year everywhere. As shown in Fig. 3.2, typical post-fit residuals of the geoid height time series were 1-2 mm. Fig. 3.3 clearly show that (1) coseismic and postseismic geoid height changes have opposite polarities, and (2) postseismic geoid height changes have relatively short time constant (0.6 year in this case).
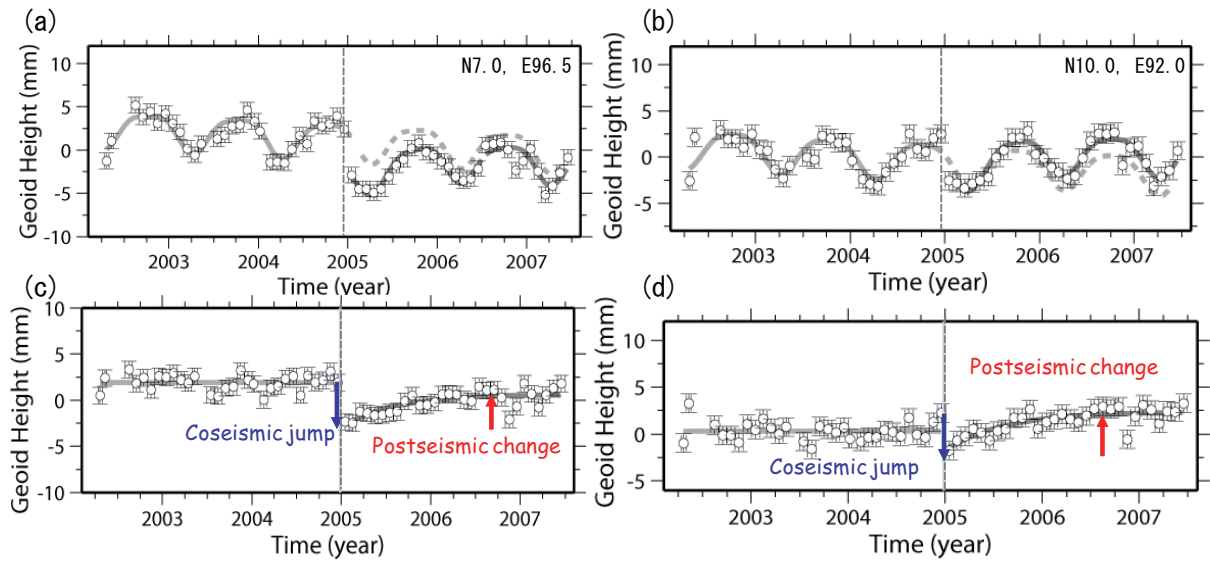
Fig. 3.2: Time series of geoid height changes at point (a) (N7, E96.5) and (b) (N10, E92) by GRACE. Vertical gray lines show the occurrence time of the 2004 Sumatra-Andaman earthquake. Light and dark gray curves are drawn by eq. 3.1 and eq. 3.2. (c) and (d) show same time series as (a) and (b) but inter-annual and seasonal components have been removed.

In order to discuss the mechanism of postseismic geoid height changes, I shall discuss coseismic geoid height changes at first. Then I will discuss how and why such postseismic geoid height changes has occurred.

3.3 Modeling of coseismic geoid height changes

Coseismic gravity/geoid height changes reflect the deformation of boundaries with density contrasts between sea and crust, crust and mantle, and density perturbation of rocks by dilation and compression. These quantities can be calculated using the program to calculate elastic response of a half space to a rectangular fault by Okada [1992], following the method Han et al. [2006] used. Here I calculate such coseismic geoid height changes a little differently from Han et al. [2006].

First I assume fault parameters by Banerjee et al. [2007] and calculate surface and Moho uplift/subsidence [Fig. 3.4] as well as volume strain at a desired point in an elastic homogeneous half
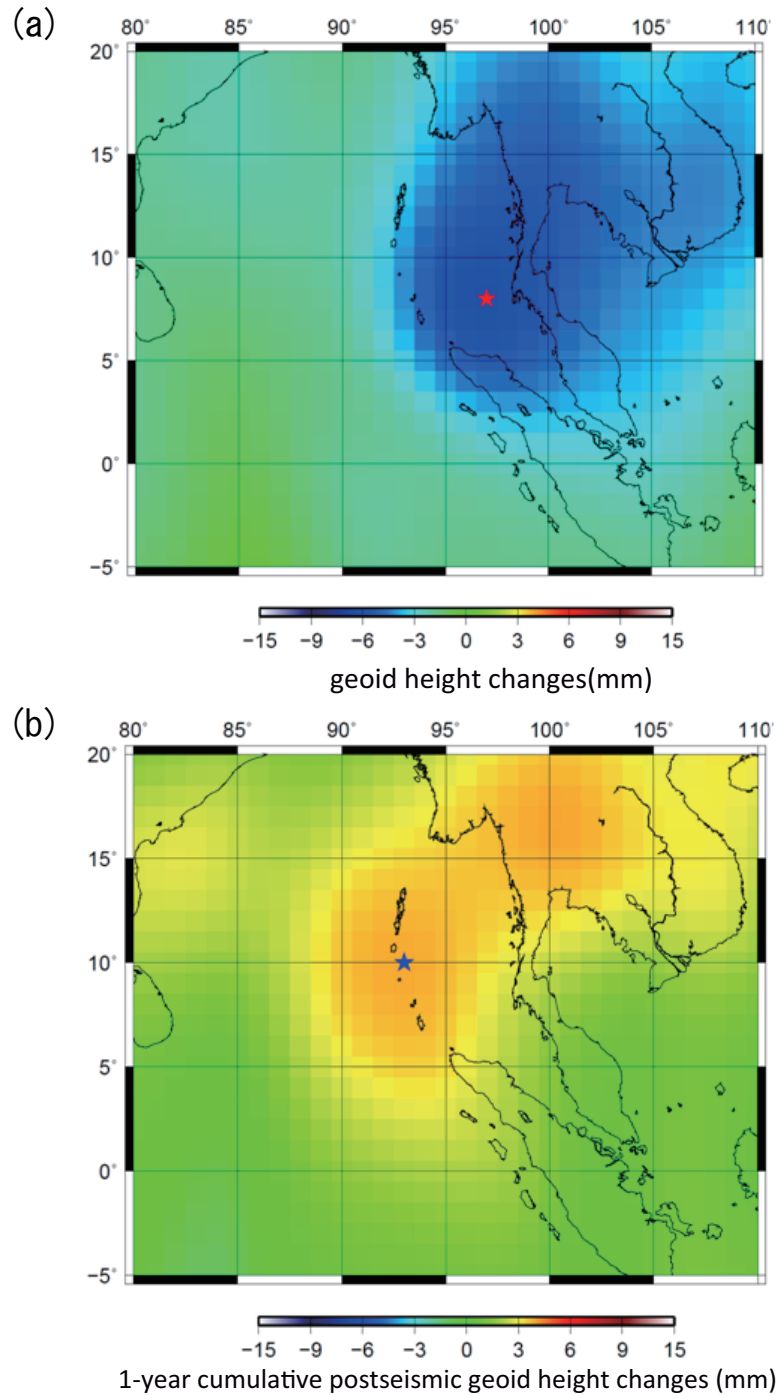
Fig. 3.3: Geographic distribution of (a) coseismic jump of geoid height and (b) 1-year cumulative postseismic geoid height change. Red and blue stars indicate points where geoid height time series are shown in Figs. 3.2.
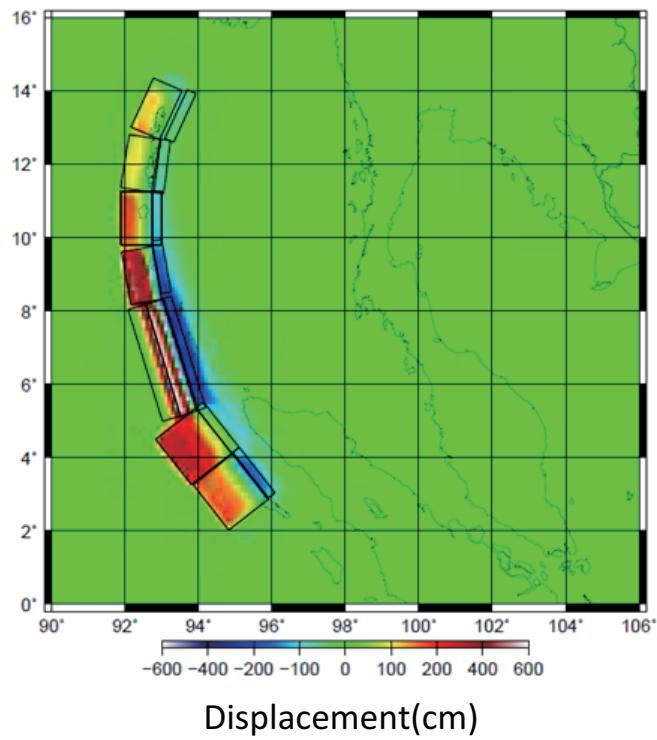
Fig. 3.4: Coseismic uplift/subsidence in the 2004 Sumatra-Andaman earthquake. Fault parameters are adopted from Banerjee et al. (2007).

space [Okada, 1992]. Difference from a more realistic approach assuming spherical and layered

Earth would be < 10% because mass perturbations contributing to geoid deformation mostly occur

within 100 km from the fault [Cummins et al., 1998]. With the resultant displacements at sea floor

$u_{surface}$ and Moho u_{Moho}, small mass perturbations $\delta m_{surface}$, δm_{Moho} can be written as follows:

$$\delta m_{surface} \quad = \quad (\rho_{crust} - \rho_{sea})u_{surface}(x, y) \tag{3.3}$$

$$\delta m_{Moho} \quad = \quad (\rho_{mantle} - \rho_{crust})u_{Moho}(x, y) \tag{3.4}$$

where ρ_{sea} ρ_{crsut} and ρ_{mantle} are densities of seawater, crust and mantle, respectively. Scalar

potential changes due to the displacements, $\delta U_{displacement}$, is calculated by integrating the potential

by such small mass perturbations δm,

$$\delta U_{displacement} = \int \int_s \frac{G\delta m}{r} dS, \tag{3.5}$$

where G is the universal gravity constant. The distance from the point to the geoid, r, is calculated

assuming a spherical Earth. By dividing scalar potentials by the surface gravitational acceleration

g, geoid height changes due to uplift/subsidence $\delta h_{displacement}$ can be calculated [Fig. 3.5].

$$\delta h_{displacement} = \delta U_{displacement}/g \tag{3.6}$$

Secondly, in order to calculate geoid height changes due to dilatation/compression, a volume

strain, $u_{xx} + u_{yy} + u_{zz}$, should be calculated. With the densities of crust ρ_{crust} and mantle ρ_{mantle},

small mass perturbations due to dilatation/compression at a point in the crust δm_{crust} and mantle

δm_{mantle} are calculated as follows.

$$\delta m_{crust} \quad = \quad \rho_{crust}(u_{xx} + u_{yy} + u_{zz}) \tag{3.7}$$

$$\delta m_{mantle} \quad = \quad \rho_{mantle}(u_{xx} + u_{yy} + u_{zz}) \tag{3.8}$$

Geoid height changes due to dilation/compression, $\delta h_{dilatation}$, are calculated by integrating δm (= $\delta U_{dilatation}$) and dividing them by g [Fig. 3.6],

$$\delta U_{dilatation} = \int \int \int_v \frac{G\delta m}{r} dV \tag{3.9}$$

where V indicates volume.

$$\delta h_{dilatation} = \delta U_{dilatation}/g \tag{3.10}$$

The Earth's density structure used in this study was adopted from Han et al., [2006] [Fig. 3.7]. In Fig. 3.5 (c), 3.6 (c) and 3.8 (a), short-wavelength signals due to displacements are seen near the fault, while those due to dilatation/compression extend over a large area. Contribution of the latter to geoid height changes is stronger than the former.

As mentioned in Chapter 2, GRACE data are composed of monthly spherical harmonic Stokes' coefficients up to degree and order 60. It is therefore difficult to see short wavelength signals with the GRACE data. In order to compare predicted coseismic changes with the observed changes from GRACE, the original result [Fig. 3.8 (a)] needs to be blurred by reducing the short wavelength components. In order to do that, I convert gridded result of Fig. 3.8 (a) into the spherical harmonic coefficients by following Swenson and Wahr [2002], and applied 350km Gaussian filter to the obtained the coefficients [Fig. 3.8 (b)]. Please refer to Chapter 5.2.2 for more details. The

patterns of Fig. 3.3 (a) and Fig. 3.8 (b) show good agreement. Profiles along N7° also show good agreement [Fig. 3.8 (c)].

The details of the data and analysis methods in Han et al., [2006], who detected coseismic gravity changes with the GRACE data, are somewhat different from ours as summarized below. First of all, their study is based on their own GRACE data analysis without using the spherical harmonics while we used public domain Level-2 data sets composed of Stokes' coefficients. Secondly, their obtained coseismic gravity changes is calculated by subtracting 4 month mean difference between 2005 and 2004, so their results may to some extent include an early part of the postseismic changes. Their result shows negative gravity anomalies and the peak is located in the Andaman Sea. The predicted gravity changes by the same method described in Chapter 3.3 shows good agreement with the changes observed by GRACE. Our results thus reinforce the results by Han et al., [2006] using a different quantity, i.e. geoid height.
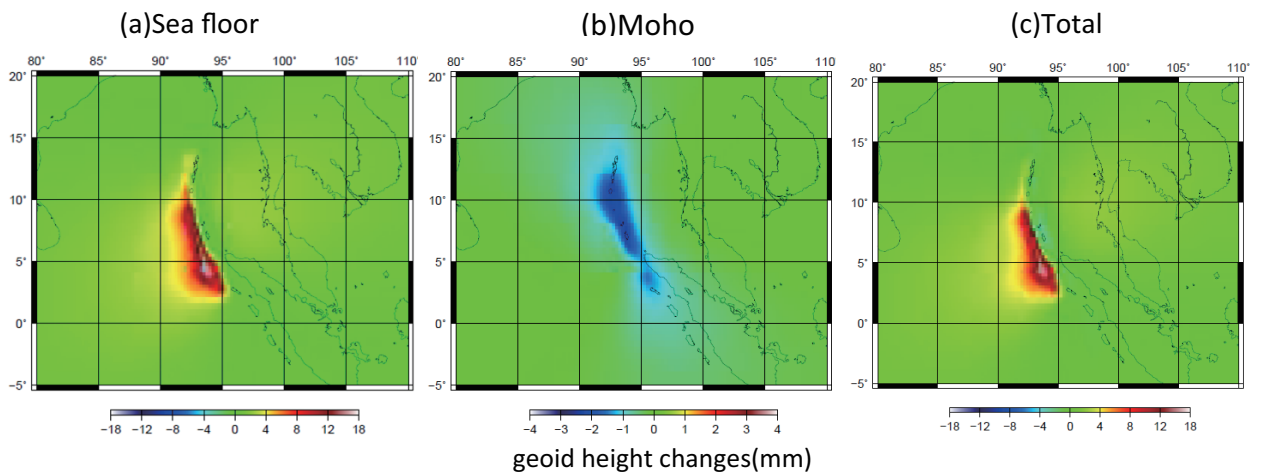
Fig. 3.5: Coseismic geoid height changes due to uplift/subsidence at sea floor (a), Moho (b) and their total changes (c).
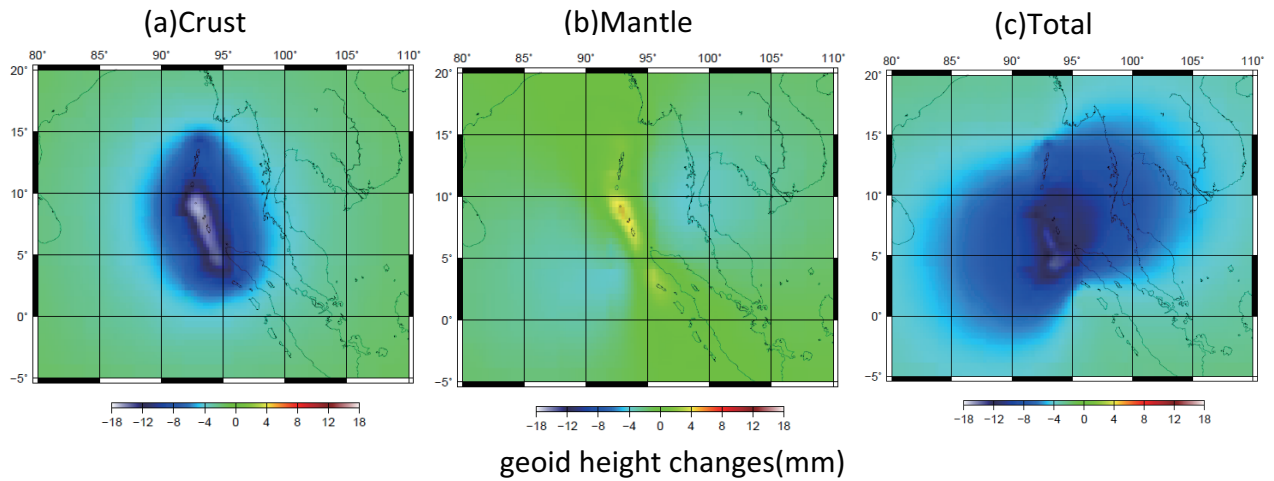
Fig. 3.6: Coseismic geoid height changes] due to dilatation/compression in crust (a), mantle (b) and the total (c).
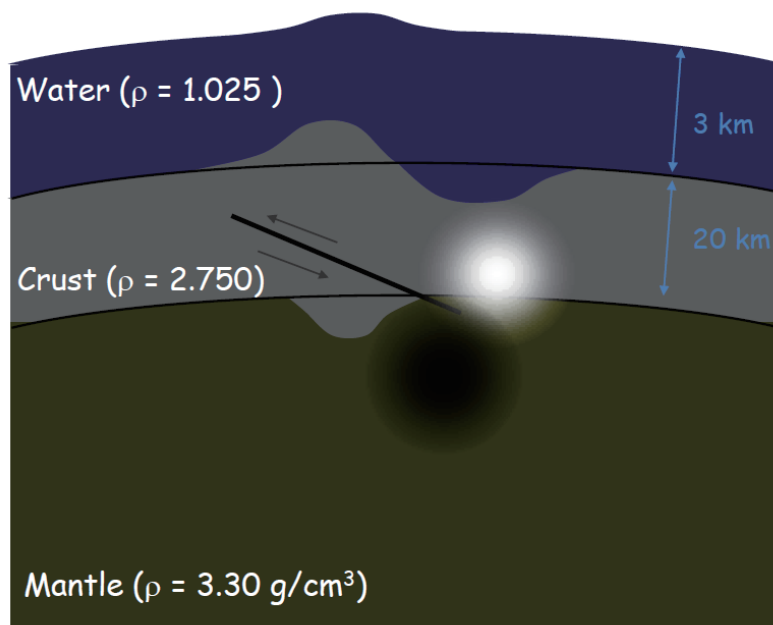
Fig. 3.7: Density structure of the Earth assumed in this study. We adopted these values from Han et al. [2006]
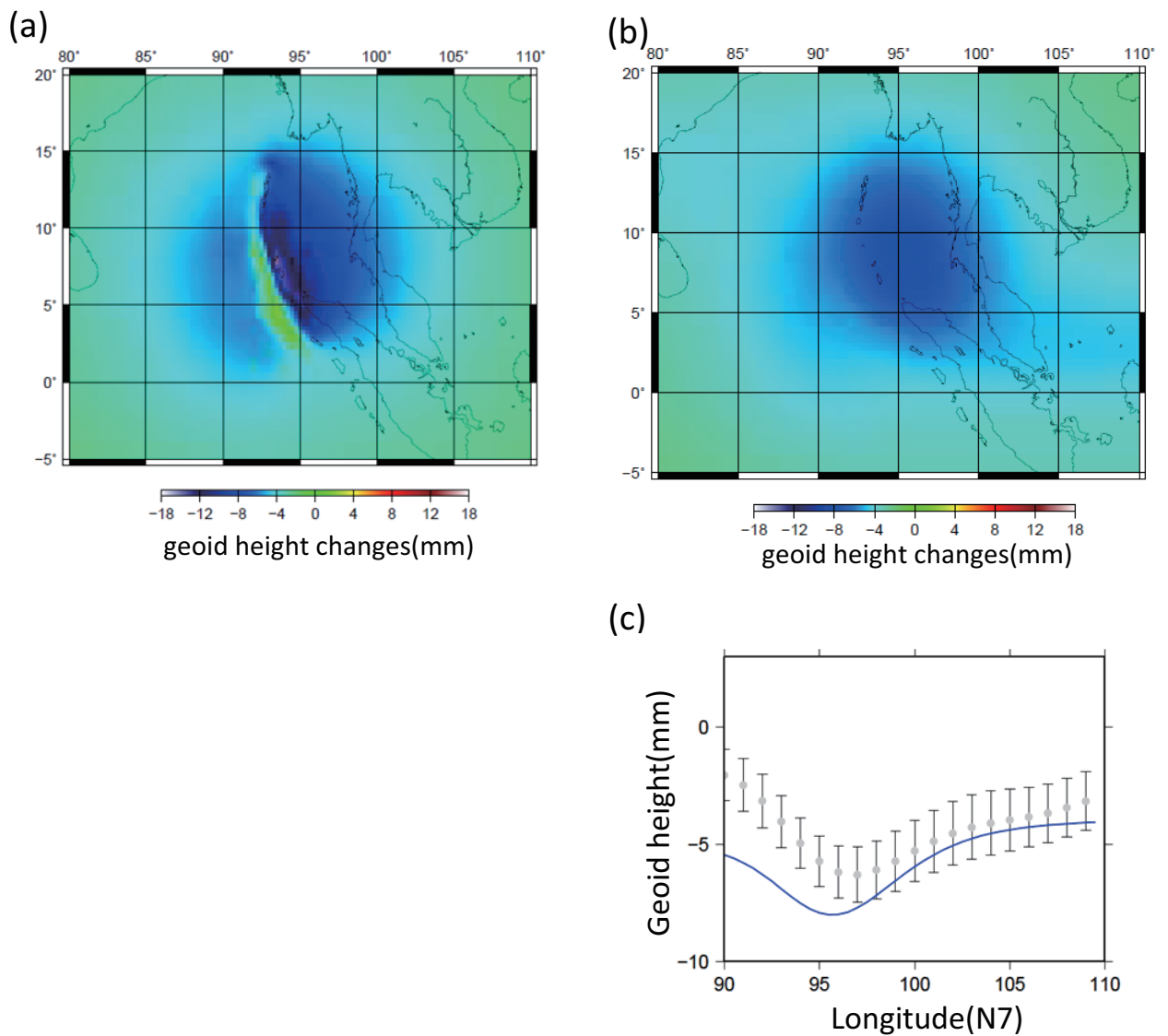
Fig. 3.8: (a) Predicted coseismic change in geoid height (mm) (b) same as (a) but a 350 km isotropic Gaussian filter has been applied (unit: mm). (c) The profile of (b) and Fig. 3.3 along the east-west line along the latitude of N7.0. Gray dots and a blue curve show GRACE observations and predicted changes, respectively.

3.4 Postseismic geoid height changes

Fig. 3.3 (b) has two peaks of signals, one near the Andaman Island and the other in Thailand. The signals in Thailand is considered to be irrelevant to the earthquake as explained below. I applied eq. (3.2) to a hydrological model, the Global Land Data Assimilation System (GLDAS) [Rodell et al., 2004]. GLDAS model provides monthly water storage at 1×1 degree grid points (See Chapter 4 for details). In order to compare the hydrological model with the GRACE data, I applied 350 km Gaussian filter to the model and estimated the a_6 term in eq. (3.2) [Fig. 3.9]. A significant positive signal was found in Thailand from GLDAS model, which means that the geoid uplift observed by GRACE in Thailand was due to land hydrological processes. Thus, I regard the positive signals only around the Andaman Island as postseismic geoid height changes.
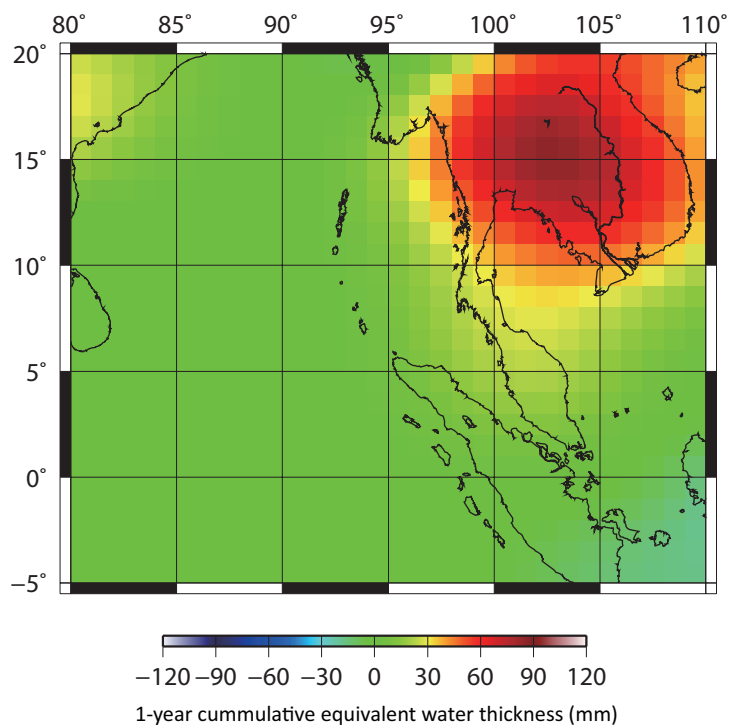
Fig. 3.9: Geographic distribution of a_6 term in GLDAS hydrological model. A 350-km Gaussian filter is applied so that we can compare it with Fig. 3.3 (b)

The profile of the observed postseismic geoid height changes along N7° from the GRACE data [Fig. 3.10] suggests that the postseismic geoid uplifts are statistically significant. The 1-year postseismic geoid height change is comparable in amount to the coseismic subsidence [Fig. 3.3]. This is the first detection of postseismic gravity/geoid height changes with satellite gravimetry, and heir mechanism should be discussed. Postseismic changes in gravity/geoid height are possibly caused by the following three mechanisms; (1) afterslip, (2) viscous mantle relaxation, and (3) pore fluid diffusion. I will examine these three mechanism in the next section.
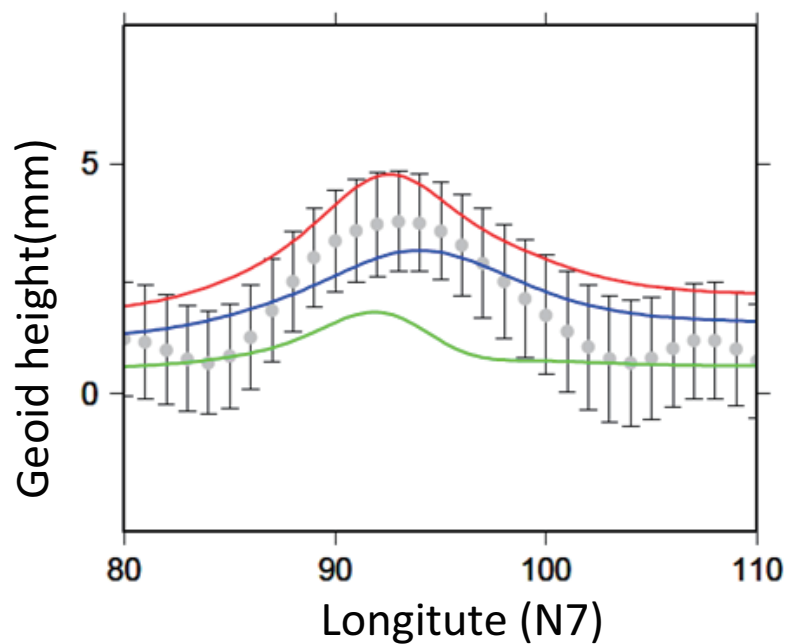
Fig. 3.10: The profile of the predicted postseismic geoid height change along the N7.0. Gray dots show observed postseismic geoid height changes. 1σ error bars are determined a-posteriori based on the post-fit residuals of the geoid height time series. 1σ error bars are less than 2mm. Green and blue curves show geoid height changes due to afterslip (with the 1-year cumulative moment as large as one half the main rupture) and predicted decay of dilatation (we assumed that 30% of coseismic dilatation has been released). Red curves show the postseismic model obtained by combining the contributions from these two.

3.4.1 Afterslip and viscous mantle relaxation

Interplate thrust earthquakes are usually followed by a large amounts of afterslips. Afterslips often release seismic moments comparable to the main rupture [e. g. Heki et al., 1997]. They cause surface displacements similar to coseismic jumps in direction with time constants from days to years.
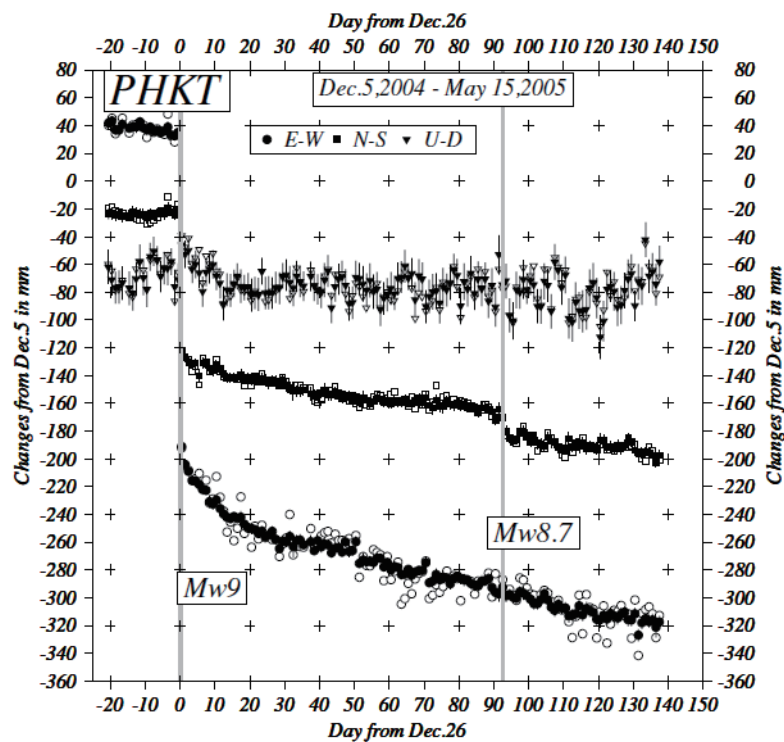
Fig. 3.11: Co- and postseismic movements of the 2004 Sumatra-Andaman Earthquake observed at a GPS point in Phuket [Hashimoto et al., 2006]. The postseismic movements are similar in direction to the coseismic jumps.

Continuous GPS observations around the focal area demonstrated that this earthquake was also followed by a significant afterslip, with the moment not smaller than a few tens of percents of the main rupture [Vigny et al., 2005; Hashimoto et al., 2006]. For example, GPS time series at a station in Phuket, Thailand [Fig. 3.11], shows large coseismic displacement in both north-south and east-

west directions. Postseismic movements are in the same direction as the coseismic displacement. In this station, vertical displacement is relatively small because the faulting occurred on a low-angle thrust fault. After all, co- and postseismic displacements shows the same polarity, and the polarity reversal between coseismic and postseismic geoid height changes found in Fig. 3.3 cannot be explained by a simple afterslip. However, as shown in Fig. 3.11, afterslip actually occurred and has caused gravity changes similar to coseismic changes. Therefore, Fig. 3.3 suggests that another mechanism should be considered to cancel the gravity changes caused by the afterslip.

Viscous relaxation of the mantle also causes slow surface displacements. For example, current oceanward crustal movements in Chile and western Argentine are explained by viscous flow of mantle rocks with Maxwell viscoelasticity [Fig. 3.12 (a)] (with the viscosity η of 2.5×10^{19} Pa· s) induced by the 1960 Chilean Earthquake [Hu et al., 2004]. Assuming the similar viscosity structure beneath Sumatra, together with elastic modulus ϵ of 40 GPa, the Maxwell time η/ϵ of relaxation becomes $\sim$ 20 years, i.e. this mechanism would hardly explain the 0.6 year timescale changes discussed here. On the other hand, a Kelvin element viscosity [Fig. 3.12 (b)], representing the delayed elasticity in a biviscous rheology, of $\sim 5 \times 10^{17}$ Pa· s is suggested to explain postseismic crustal movement [Pollitz et al., 2006]. A Kelvin element viscosity can explain the short time constant observed by GRACE. Moreover, if we consider low viscosity, it may be able to explain the obtained time constant by GRACE. However, it is difficult to explain the observed polarity reversal between coseismic and postseismic geoid height changes even though time constant can be explained. In order to explain the polarity reversal of geoid height changes and short time constant, I make a case for the third mechanism, water diffusion around the down-dip end of the fault.

(a)

(b)

$\eta_1 : \sim 10^{19}$ Pa s

$\eta_2 : \sim 10^{17}$ Pa s
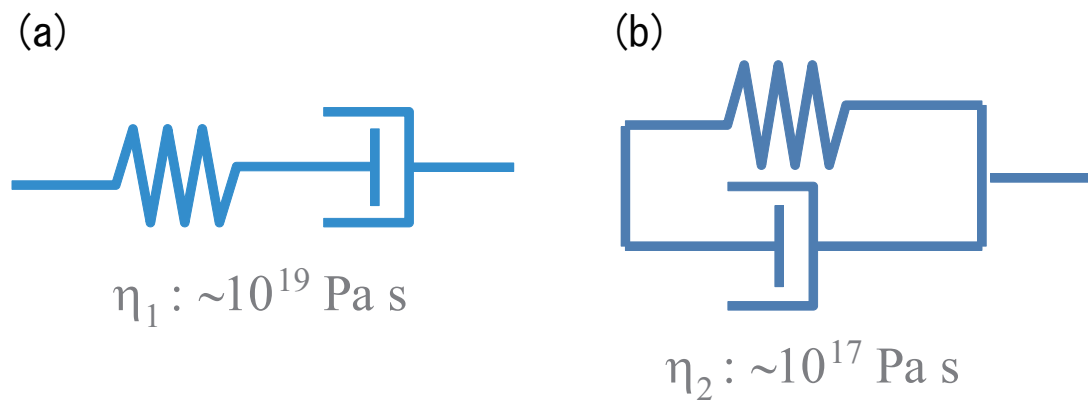
Fig. 3.12: The images of Maxwell substance and Kelvin substance.

3.5 Diffusion of Water

Pore fluid diffusion causes postseismic changes opposite to the coseismic ones with relatively short timescales [J$\acute{o}$nsson et al., 2003]. Dilatation and compression associated with faulting disturb distribution of pore fluid pressure, and the fluid diffuses from the region with the increased pressure (compression part) to the decreased pressure region (dilatation part) [Nur and Booker, 1972]. This phenomenon has been supposed to occur in the uppermost crust, but we here suggest that it may occur deep in the mantle by supercritical water that abundantly exists in subduction zones.

As mentioned in Chapter 3.3, coseismic volume strain can be calculated. For a thrust earthquake, two pairs of increased/decreased pore pressure changes are formed at the up-dip and the down-dip end of the fault The cross section of coseismic volume strain due to the event clearly shows a pair of compression (red) and dilatation (blue) around the down-dip end of the fault [Fig. 3.14]. The other pair at the up-dip end of the fault becomes much smaller in order to satisfy the boundary condition at the ground surface. Around the down-dip end, water flow from the red to blue parts would occur following the pressure perturbation [Fig. 3.13]. Buoyancy would also encourage such upward flow in order to recover hydrostatic equilibrium disturbed by the density
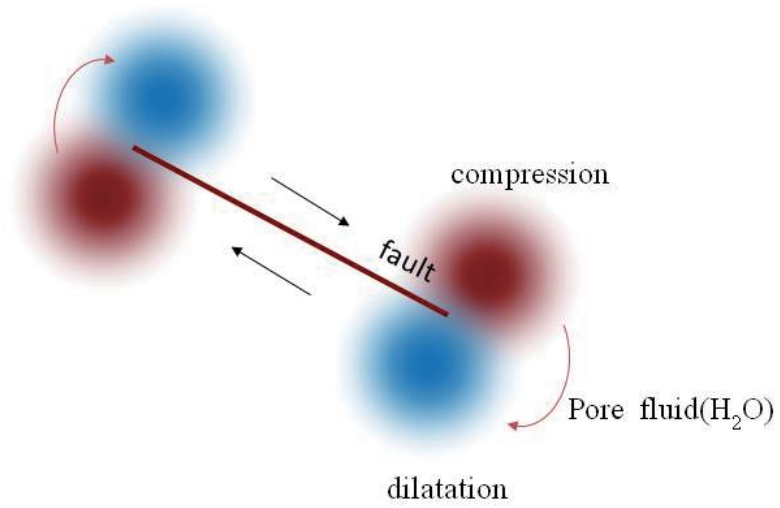
Fig. 3.13: Schematic view of coseismic dilatation (blue parts) and compression (red parts)
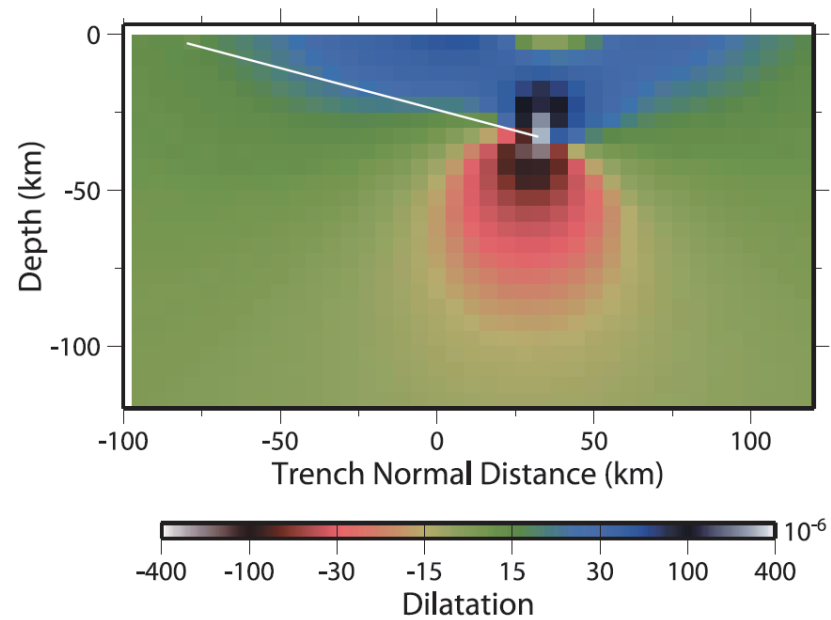
Fig. 3.14: Calculated coseismic dilatation (blue parts) and compression (red parts)

decrease of the shallow layer. Such mantle water flow will continue until the driving forces (pressure gradient and gravity) vanish under the new hydrostatic equilibrium. By then, the dilatation signal in geoid will be relaxed while dilatation/compression of the solid part (crustal and mantle rocks) remains almost intact.

Here two questions arise here to explain the observed geoid height changes.

(1) Dilatation/compression due to the earthquake occurs in 30km-50km in Fig. 3.14. Is the mantle water ample enough to allow such an adjustment in such a depth ?

(2) The observed time constant of postseismic geoid height is 0.6 year. Can mantle water diffuse that fast?

I will discuss these questions.

The coseismic volume strain is mostly within 10^{-5} level around the down-dip end [Fig. 3.14]. Water in oceanic crust of subducting slabs is released at the depth of a few tens of kilometers (depending on thermal structure), which then diffuses into the wedge mantle and serpentinize mantle rocks [Iwamori, 1998]. Recent petrologic studies suggest water content as high as 0.5 weight percent or more in the upper mantle of back arc [Kelley et al., 2006]. That is, the weight percent of H_2O down there is much larger than the coseismic dilatation and compression. So movement of just a small portion of the total water could compensate density perturbation caused by such small dilatation/compression.

As for (2), the pressure difference lets the pore pressure obey diffusion equation:

$$\frac{\partial P(r,t)}{\partial t} = c\nabla^2 P(r,t) \tag{3.11}$$
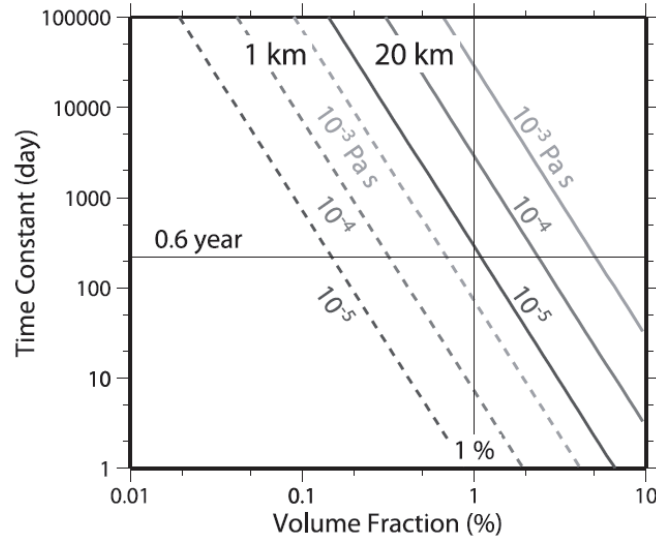
Fig. 3.15: Time constant of the pore pressure diffusion for distances 1 km and 20 km as functions of the volume fraction of pore fluid. Three kinds of viscosity of the pore fluid, 10^{-3}, 10^{-4}, 10^{-5} Pa·s, are assumed.

Eq. 3.11 is most easily solved as follows [Nur and Booker, 1972],

$$P(r,t) = A\frac{1 - exp(-r^2/4ct)}{r} \sin\theta, \qquad (3.12)$$

where r, θ, c are the distance from the fault end, angle from the fault, the pore pressure diffusivity, respectively. c is calculated by $k/\eta\beta$. There k is permeability, η is the viscosity of pore fluid, and β is bulk compressibility. With the pore pressure diffusivity c and a travel distance L, the time constant τ is expressed by $L^2/4c$ [Nur and Booker, 1972]. That is, time constant for pore fluid diffusion depends on permeability and viscosity of pore fluid. Fig. (3.15) shows τ as a function of φ, and for different values of L (1km and 20km) and η. The quantity β is fixed to 2.5×10^{-11} Pa^{-1}. Due to ambient high pressure and temperature, water (or H_2O) behaves as supercritical fluid whose viscosity is closer to gas (10^{-5} Pa·s level) than to liquid (10^{-3} Pa· s level). The time constant

τ of 0.6 year is realized with the volume percent of H_2O of $\sim 1\%$ and with the viscosity 10^{-5} Pa·s. Mantle water diffusion can therefore take place on a < 1 year timescale required to fit postseismic geoid changes with reasonable hydraulic parameters. With equation 3.12, it is possible to calculate water diffusion around the down-dip end of the fault. Assuming the pore diffusivity, c, is 3.2 m^2/s, I simulated water diffusion in 10 days, 100 days (= 0.6 year) and 1 year using an arbitrary fault geometry [Fig. 3.16]. Fig. 3.16 suggests that 0.6 year can diffuse pore pressures around the down-dip end of an arbitrary fault by the upward movement of the fluid from the increased (red) part to the decreased (blue) part.

3.6 Discussion

Afterslip causes uplift/subsidence and dilatation/compression similar to the main rupture, and may leave geoid depression signature similar to Fig. 3.8 (b). However, such geoid depression might recover to some extent by simultaneous diffusion of mantle water as the afterslip slowly goes on. Therefore geoid signal of afterslip may look different, i.e. composed more of uplift/subsidence signature and less of dilatation/compression signature. Fig. 3.10 shows the "model" postseismic geoid uplift profile, calculated as the mixture of the decay of the coseismic dilatation signature and afterslip. The model assumes that an afterslip with the one-year cumulative moment release equal to one half of the main rupture has occurred, and that 30% of the coseismic dilatation signature has disappeared. In this result, observed postseismic geoid height changes may be explained by pore fluid diffusion to a certain extent. This model is not unique, e.g. we could consider less afterslip and more decay of the coseismic dilatation, and vice versa. We did not consider viscous mantle relaxation here, but its contribution to geoid changes should grow in time and merits long-term attention.

Since Ogawa and Heki[2007] was published [Table 2], many studies related to postseismic
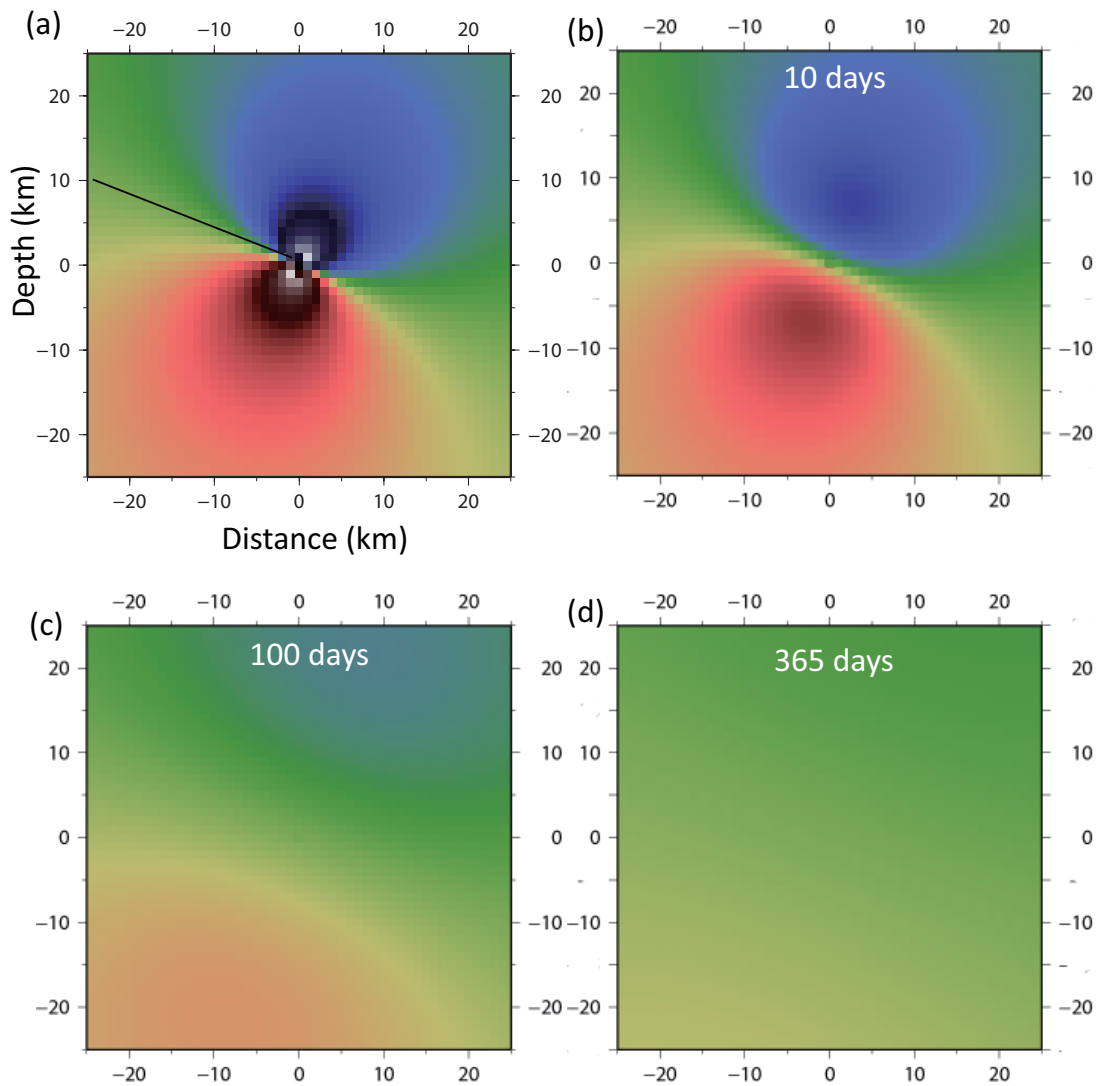
Fig. 3.16: Simulated water diffusion calculated using the equation (3.12) (arbitrary unit and fault geometry). I assumed the pore diffusivity c of 3.2 m^2/s. The obtained increased/decreased pore pressure (a) has been relaxed in 10 days (b), 100 days (= 0.6 year) (c) and 1 year (d).

gravity/geoid height changes due to the Sumatra-Andaman earthquake have been published. Some papers discuss only geodetic aspect of the issue, e.g. how to detect postseismic gravity/geoid height changes. While we applied least square methods to the obtained time series [e. g. Ogawa and Heki, 2007; de Linage et al., 2009], some people estimated postseismic parameters by stacking of 1 or 2 years data and retrieving the differences [e. g. Chen et al., 2007, Panet et al., 2007]. On the other hand, de Viron et al. (2006) proposed a method based of the Empirical Orthogonal Function (EOF) analysis. These papers suggest that positive gravity/geoid height could change with a relatively short time constant as shown in the table. 2. Some papers also discuss geophysical aspect of the issue. While Ogawa and Heki [2007] explained the obtained postseismic with pore fluid diffusion, Panet et al. [2007] tried to explain the observed postseismic gravity signals by low viscosity materials beneath the active Central Andaman Basin. Hasegawa et al. [submitted] interpreted that postseismic gravity changes can be interpreted by two different types of afterslips, fast slip in the shallow zone and slower slips in the deeper zone. Recently, modeling of pore pressure recovery after the earthquake has been discussed in terms of stress perturbation [Hughes and Masterlark, 2009]. The true mechanism of postseismic gravity/geoid height changes are yet to be clarified by longer term observations of gravity field and crustal deformation.

Reference	Mechanism	Characteristics
Ogawa and Heki [2007]	Pore fluid diffusion (Partly afterslip)	First detection Time constant: 0.6year
Panet et al. [2007]	Viscous mantle relaxation	Time constant: 3 and 9 months
Chen et al. [2007]		
de Viron et al. [2008]		Detection by EOF analysis
de Linage et al. [2009]		Time constant: 0.7year
Hasegawa et al. [under revision]	Afterslip	Time constant: 1 ~ 2 months and 1year

Table. 2: Recent studies about postseismic gravity/geoid height changes by GRACE

4 Acceleration signals in GRACE time-variable gravity in relation to inter-annual hydrological changes

4.1 Introduction

Many geophysical and climatic changes have been studied using time-variable gravity (TVG) data from the twin-satellite mission of GRACE which was launched in 2002. As described in Chapter 1, in addition to a seasonal TVG, a long-term TVG trends began to be detected in various regions. They include gravity signals of the present-day melting of ice sheet in the coastal Greenland [e.g. Luthcke et al., 2006] and mountain glaciers in Alaska [e.g. Chen et al., 2006], and secular TVG increase by glacial isostatic adjustment (GIA) in northern North America [Tamisiea et al., 2007] and northern Europe [Steffen et al., 2009]. Inter-annual TVG in Greenland indicated that the ice loss has been accelerating there [Velicogna and Wahr, 2006].

With the accumulation of available TVG data exceeding 7 years in time span at present, it is now imperative and feasible to examine temporal variation of the trend. Such a variation, for any given geographical location, constitutes by definition an acceleration signal in TVG, which I shall simply model with a quadratic polynomial, or a parabolic function, in time within the studied time span. The acceleration in TVG naturally reflects the acceleration in the cause of TVG, that is, the mass transport in the Earth system. In particular, I shall focus on continental hydrological mass variations: any temporal acceleration thereof is obviously of grave importance in monitoring and understanding of present-day global climate change, as well as in predicting the future. Such is already the case in the observed sea level rise, as emphasized in the Intergovernmental Panel on Climate Change (IPCC) 2007 report [Bindoff et al., 2007].

4.2 Data and Processing

For the TVG signals whose sources are mass transports occurring on the Earth's surface, one can directly and uniquely convert the observed TVG into surface mass density changes [Chao, 2005]. By the data and method described in Chapter 2, monthly $1° \times 1°$ gridded changes is calculated in terms of equivalent water thickness (EWT). Here 500 km averaging radius is applied to eq. (2.6) to reduce higher degree noises. At this stage, I disregard any non-surface processes, which are not among the main interest of this chapter, such as the GIA that would have hardly any quadratic acceleration signals.

The EWT time series of any given location is then analyzed to look for hydrological accelerations as follows. If the goal is to study a linear temporal trend in TVG, the common practice is to model by eq. (2.11). The coefficient a_1 is to account for any linear trend in mass variation over the observed period. Although the time derivative of the non-seasonal part of eq. (2.11) does not mathematically depend on t or epoch t_0, different studied periods often yield different trends. For example, with time-series of EWT at arbitrary points in Eastern Europe [Fig. 4.1 (top)], such trend looks quite different between the first and the second halves of the time span. That is, the increasing trend in the first half reverses itself in the second. The opposite is seen in the equatorial region of Africa [Fig. 4.1 (bottom)]. In such cases, apparent trend changes can be a part of the inter-annual variability or just a result of a couple of anomalous years, so a discussion on trend without specifying a specific epoch is often inadequate, especially as the data time span increases. To better account for possible temporal acceleration/deceleration, therefore, I add an additional quadratic term with coefficient a_2 to eq. (2.11) as follow:

$$Mass(t) = a_0 + a_1(t - t_0) + a_2(t - t_0)^2 + b_a \sin(\omega t + \theta_a) + b_s \sin(2\omega t + \theta_s) \quad (4.1)$$
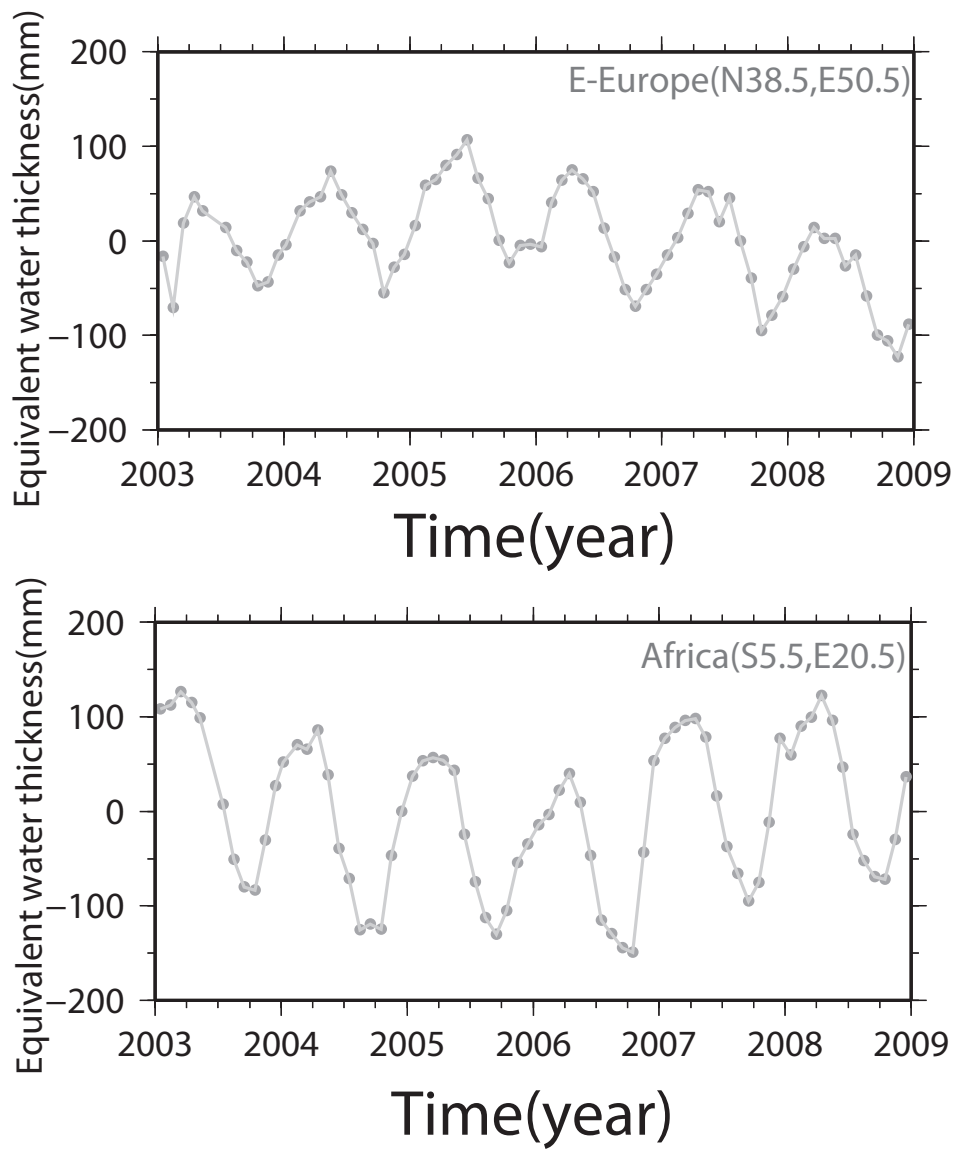
Fig. 4.1: Time-series of EWT from GRACE data at arbitrary points in Eastern Europe (top) and Africa (bottom). The dots show observed data by GRACE. The curves is just connected with each gray dot.

Now the time derivative of eq. (4.1) depends on t, and we need to specify epochs in addressing the trend. Note that the coefficient a_1 represents the "instantaneous" trend at the epoch t_0. In fact, linear trends of EWT with a different epoch show different pattern [Fig. 4.2]. Here I let the epoch $t_0 = 2006.0$, the mid-point of our time span. In that case, a_1 coincides with the average trend as recovered using eq. (2.11). The parameters in eq. (4.1) are estimated with the least-squares procedure. I plot the geographical distribution of the resultant values of the linear (a_1 with epoch t_0) and quadratic (a_2) coefficients for EWT in Figs. 4.3 (a) and 4.3 (b), respectively.
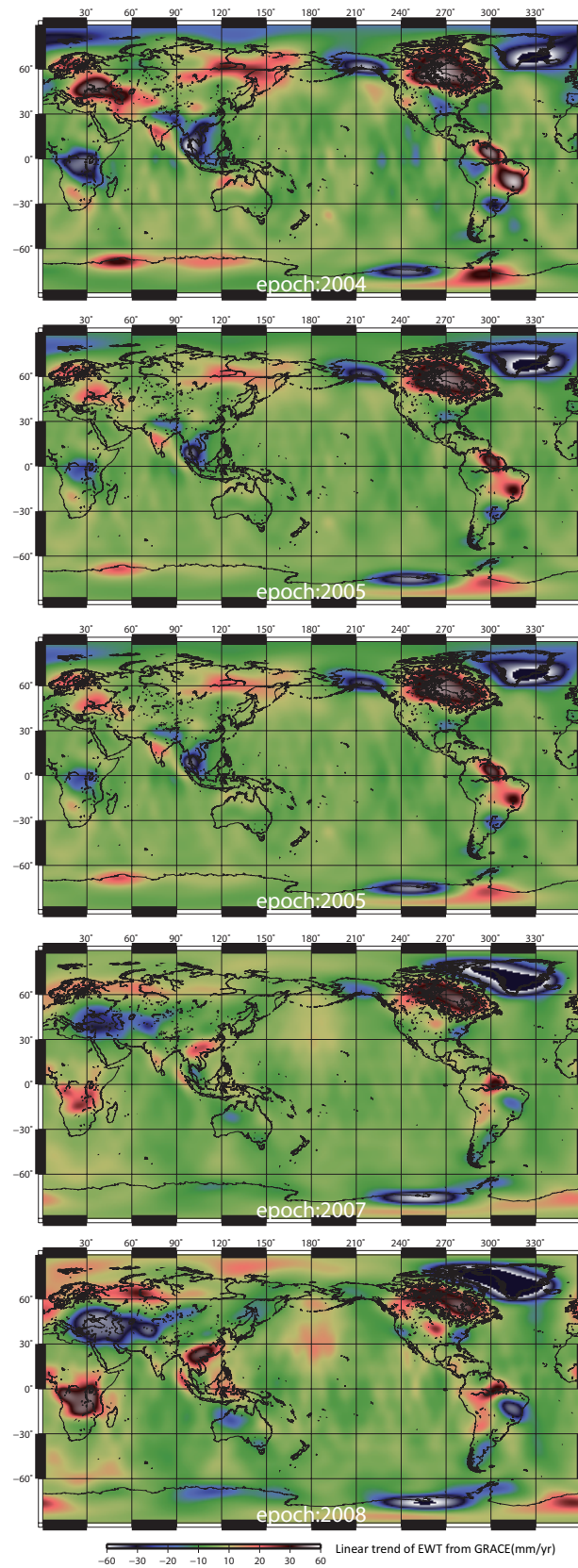
Fig. 4.2: Linear trend of EWT using different epochs from the GRACE data. Each linear trend is estimated at epochs 2004.0, 2005.0, 2006.0, 2007.0 and 2008.0 from the top.
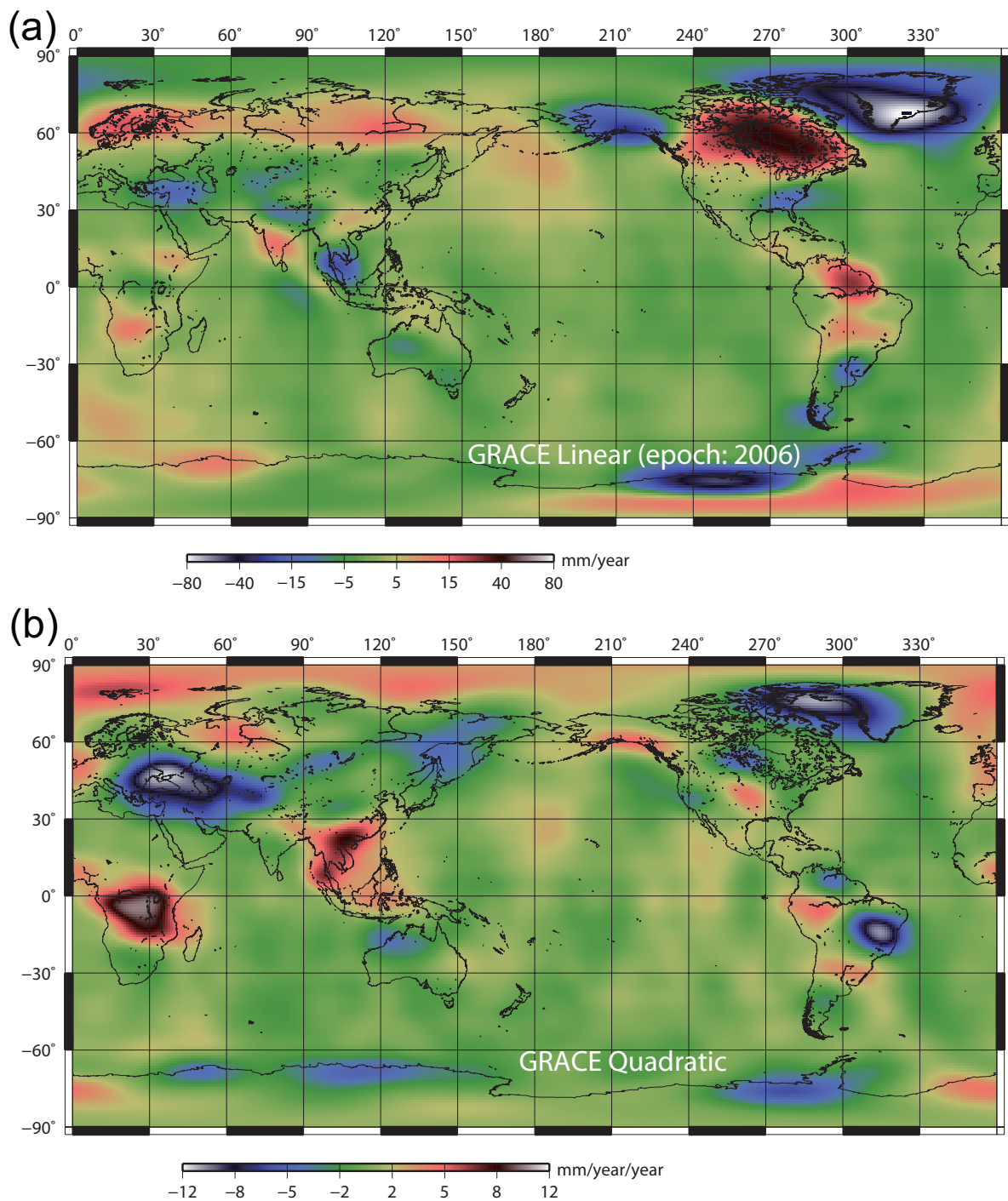
Fig. 4.3: (a) Mean linear trend (epoch 2006.0); and (b) quadratic acceleration/deceleration of EWT from GRACE data, 2003-2008 (a 500-km fan filter and de-striping filter applied).

4.3 The statistical significance

In a wave number domain, it is well known that degree variance of static gravity field is inversely proportional to the square of degree. This is what we call Kaula's rule-of-thumb. In addition to static gravity field, degree variances of seasonal component and linear trend obey Kaura's rule [Ogawa and Heki, 2006]. They also found that seasonal component up to degree 25 and linear trend up to degree 20 showed significant signals with the GRACE data in an early version. With the GRACE data in the latest version, the estimated linear and quadratic terms up to degree 50 remain well above formal uncertainties, scaled so that the χ^2 of the post-fit residuals becomes unity, and obey the Kaura's rule [Fig. 4.4 (a)]. The coefficients with degrees > 50 have large uncertainties but they little affect the recovered gravity changes as shown in Fig. 2.8 drawn with the 500 km Gaussian filter.

In order to test whether the models with higher degree terms are statistically significant, we calculated the Akaike's Information Criterion (AIC) [Akaike, 1973]. A smaller AIC means a better model. AIC certainly decreases when we add the quadratic term. However, AIC still decreases as we further add higher order terms. These results may mean that the GRACE time series do carry some significant information in their higher order terms. It general, root-mean-square (RMS) residual decreases as the degree of polynomials increases. Fig. 4.4 (b) shows that this is the case, and the RMS residual notably decreases from the model with linear function to the model with quadratic function for each Stokes' coefficient, while RMS residual does not change much by adding any of the higher degree terms.

After all, although GRACE data may have useful information in terms higher than quadratic polynomial functions, I here discuss only the implication of adding the quadratic terms in modeling the TVG over a 7 years time span. We would be able to discuss higher terms sufficiently as the
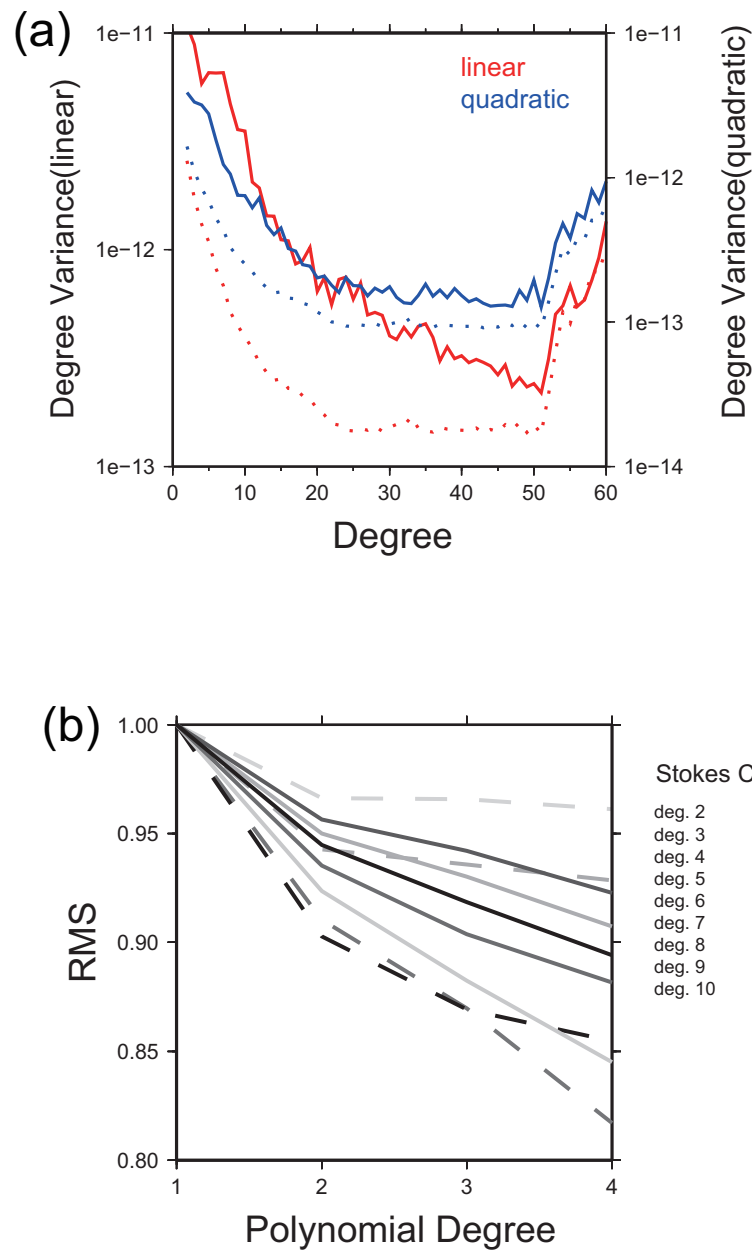
Fig. 4.4: (a) Degree variance of linear and quadratic changes of GRACE TVG. Red and blue curves show linear and quadratic terms, respectively. They all exceed one-sigma errors shown with dotted curves. (b) Relationship between post-fit RMS residuals of the Stokes coefficients of various spatial degrees and the polynomial degree for the assumed interannual fit (plus the seasonal terms). Residual decreases notably by adding the quadratic term (i.e. by changing polynomial degree from 1 to 2).

total time span of the data increases.

4.4 Results and Discussion

4.4.1 Origin of quadratic signals

Changes in the continental hydrological water storage in both forms of surface soil moisture and underground water are the main cause for (surface) TVG on land, as observed by the GRACE data. Here I discuss possible origins of quadratic changes in water storage (W), governed by the land-water budget equation:

$$\frac{dW}{dt} = P - E - R, \tag{4.2}$$

where P, E and R are the precipitation, evapotranspiration and runoff, respectively. If any of these fluxes contains a linear signal of the form, $\alpha t + \beta$, it would translate into a quadratic signal in water storage:

$$W = \frac{1}{2}\alpha t^2 + \beta t + const. \tag{4.3}$$

Conversely, acceleration in the water storage implies a linear trend in the combination of the three hydrological fluxes.

4.4.2 Comparison between quadratic signals by GRACE and liner trend by precipitation data

Thus, let us first compare GRACE data with the linear trends in P estimated from meteorological data. Crowley et al. [2006] showed good agreement between groundwater changes from GRACE data and the integrated monthly precipitation anomalies within the Congo Basin of Africa. Mor-

ishita and Heki [2008] compared the value of $P - E$ from meteorological data with anomalous changes in soil moisture related to El Nino/Southern Oscillation episodes from GRACE data. Both studies integrate P or $P - E$ to compare with W, and assume constant R without better information. Here I, instead, directly compare linear trends in the both sides of eq. (4.2). The quantity dW/dt in eq. (4.2) can be obtained from GRACE data by calculating (i) monthly EWT at grid points as shown in eq. (2.6), and (ii) their month-to-month differences at these points. Then I could calculate its trend by estimating the linear term in the time series of dW/dt using eq. (2.11) [Fig. 4.5]. This is equivalent to directly estimating the quadratic terms in GRACE with eq. (4.1) [Fig. 4.3 (b)].
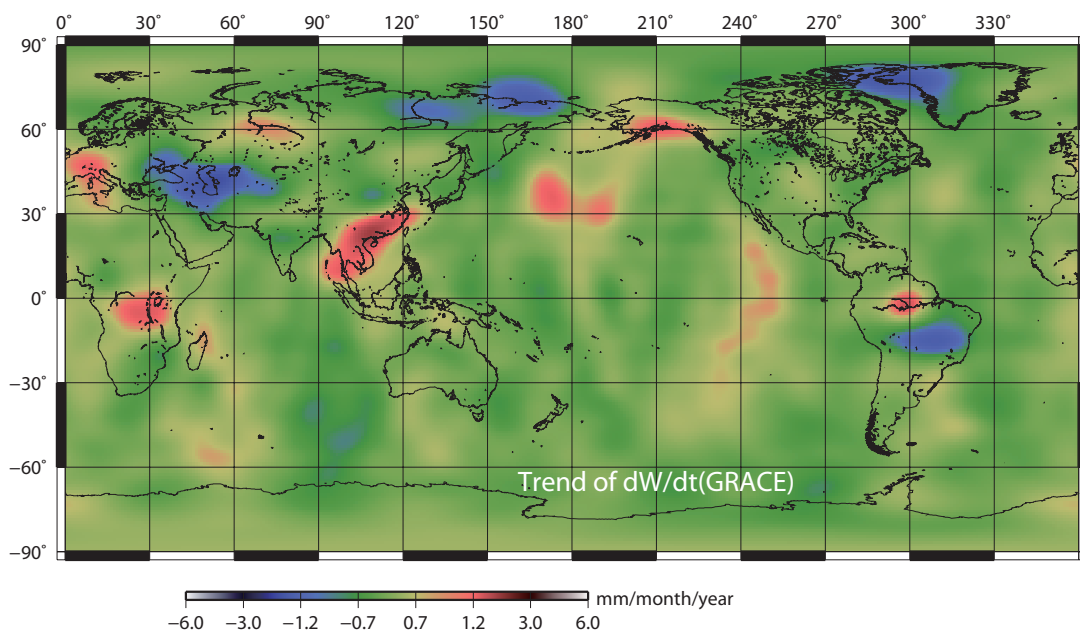
Fig. 4.5: Linear trend of dW/dt from GRACE. The same spatial filters as the GRACE data have been applied.

In parallel, monthly worldwide precipitation data are available from CMAP (Climate Prediction Center Merged Analysis of Precipitation) at 2.5×2.5 degree grids. CMAP provides merged precipitation data using rain gauge, satellite observation and NCEP (National Centers for Environ-

mental Prediction) model output. I apply the same 500 km fan filter to allow direct comparison

with the GRACE data. I then model P with eq. (2.11) to determine its linear trends, and show

them in Fig. 4.6 (the original values in mm/month/year is converted to those in mm/year/year to

allow direct comparison with Fig. 4.3 (b)). These trends constitute the contribution of P to α in

eq. (4.3). Since precipitation data on Antarctica has poorer quality, I plot Fig. 4.6 from 90°N to

60°S.
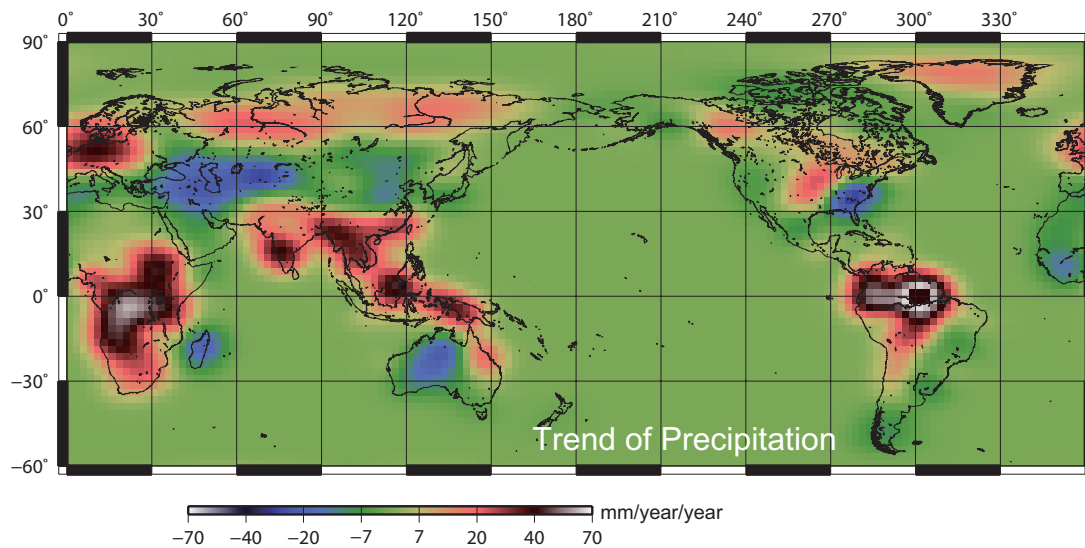
Fig. 4.6: Linear trends in P from the CMAP meteorological data. The same spatial filters as the GRACE data have been applied.

As noticed by comparing Figs. 4.3 (b) and 4.6, both show clear systematic patterns in wide

areas of Africa, Eastern Europe, Siberia, Southeast Asia, and central North America. It is natural

that they do not match in places where ice sheets or glaciers exist, such as in Greenland or Alaska

because GRACE reflects not only soil moistures but also ice meting. The signals of ice melting

are often much stronger than precipitation.

The quantities shown in Fig. 4.6 should be twice as large as those in Fig. 4.3 (b) as indicated

by the factor 1/2 in eq. (4.3). However, the former is obviously much larger than that. This

is consistent with the fact that P is only the input of the hydrological budget that determines dW/dt or W, and one has to take into account the water loss by E and R for a full comparison. Unfortunately I find the latter not feasible at present. I have tried various ways to evaluate $P - E$ or E alone from atmospheric general circulation model (GCM) data, for example using water balance in the atmosphere [Oki et al., 1995] or using temperature, hours of sunlight and precipitation data [Hamon, 1963]. They do agree well on the seasonal behavior, but not on the linear trends over the studied period of time. Even when I use the same method on different atmospheric GCM outputs to evaluate $P - E$, the results for trends often disagree [Fig. 4.7]. The same applies for the model output for R; at present their inter-annual behavior does not close the water budget as dictated by eq. (4.2). Nevertheless, the point of comparing the spatial distribution of the trend of P with the quadratic changes in the GRACE data is to confirm readily that a direct relationship exists between them, the former as the source and the latter the consequence of the water budget.
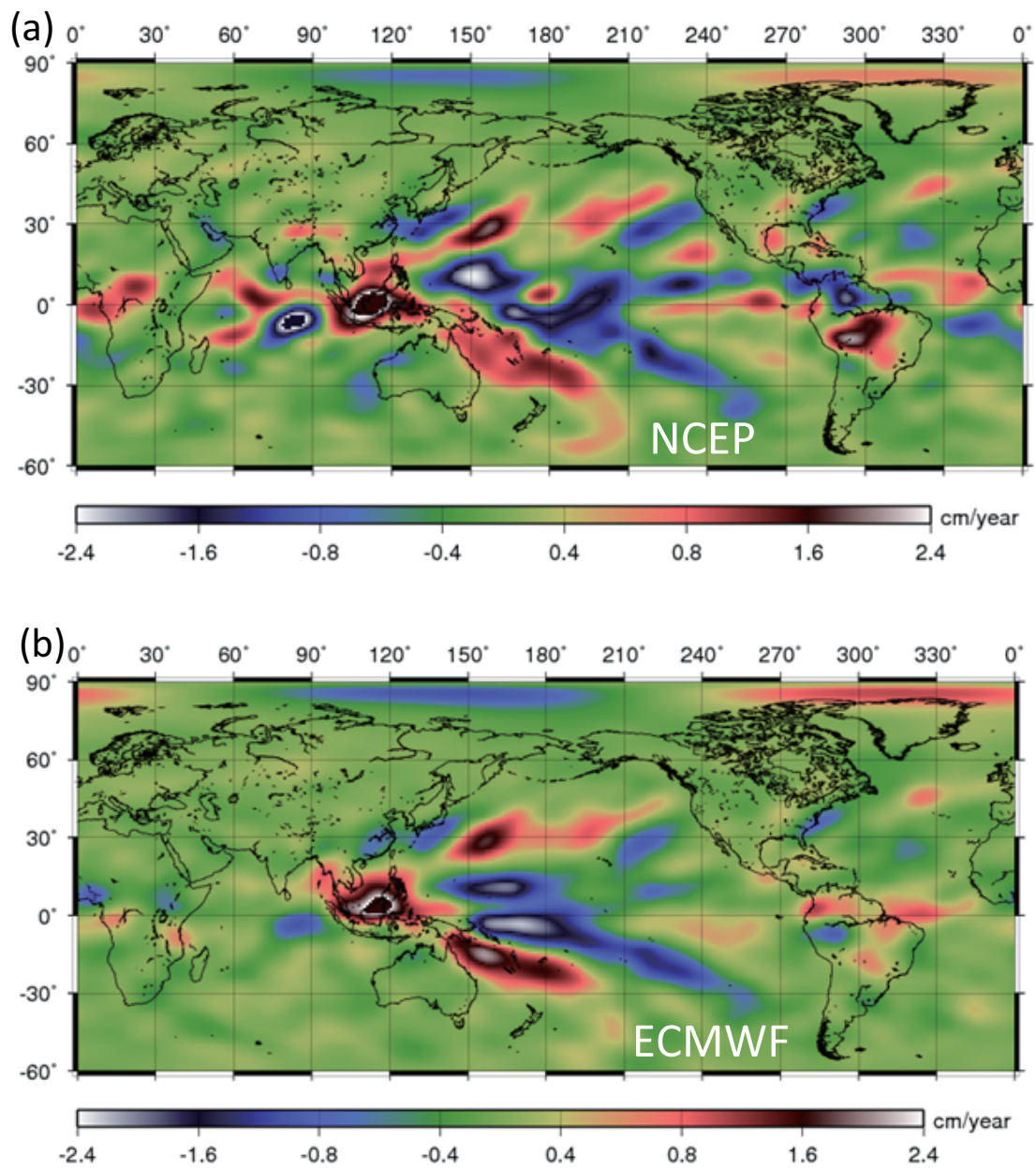
Fig. 4.7: Linear trend of $P - E$ from NCEP model output and ECMWF model outputs

4.5 Comparison between GRACE and hydrological model outputs

To further validate the GRACE results with those from independent sources, I estimate the same parameters from the Global Land Data Assimilation System (GLDAS) [Rodell et al., 2004]. GLDAS/Noah model provides snow, canopy and soil moisture data at 1×1 degree grid points, except for Antarctica and Greenland where meteorological data are inadequate or unavailable. Although GLDAS terrestrial water changes in some regions show fairly good agreement with TVG from GRACE for their seasonal variations [Tapley et al., 2004, Syed et al., 2008], reliability of inter-annual changes in GLDAS hitherto have not been discussed sufficiently yet. Here I estimate linear and quadratic terms from GLDAS/Noah data at grid points, and apply the same 500 km fan filter as I did for GRACE data.

While linear trend of precipitation corresponds to quadratic changes of the GRACE data, now it is able to compare directly linear signals of continental water storage in GLDAS [Fig. 4.8 (a)] and GRACE [Fig. 4.3 (a)] over the globe except Antarctica and Greenland. The spatial pattern of the amplitude of GRACE and GLDAS trends agree fairly well in Africa, eastern North America, northern Australia, and, to a lesser degree, near Amazon River and Siberia. On the other hand, GRACE shows a larger negative trend in Alaska than GLDAS because the latter does not include the melting of mountain glaciers. GRACE data, however, also include non-hydrological gravity changes, for example, GIA signals in Northern Canada and Scandinavia, and co-seismic [e.g. Han et al., 2006] and post-seismic [e.g. Ogawa and Heki, 2007] gravity changes associated with the great 2004 Sumatra-Andaman earthquake (see Chapter 3).

Next, I compare Figs. 4.3 (b) and 4.8 (b) for the quadratic signal. There are good agreements in the patterns of GRACE and GLDAS in many major areas. Acceleration signals (in red) are seen in both cases in equatorial Africa, Southeast Asia, western Siberia and to a lesser extent in
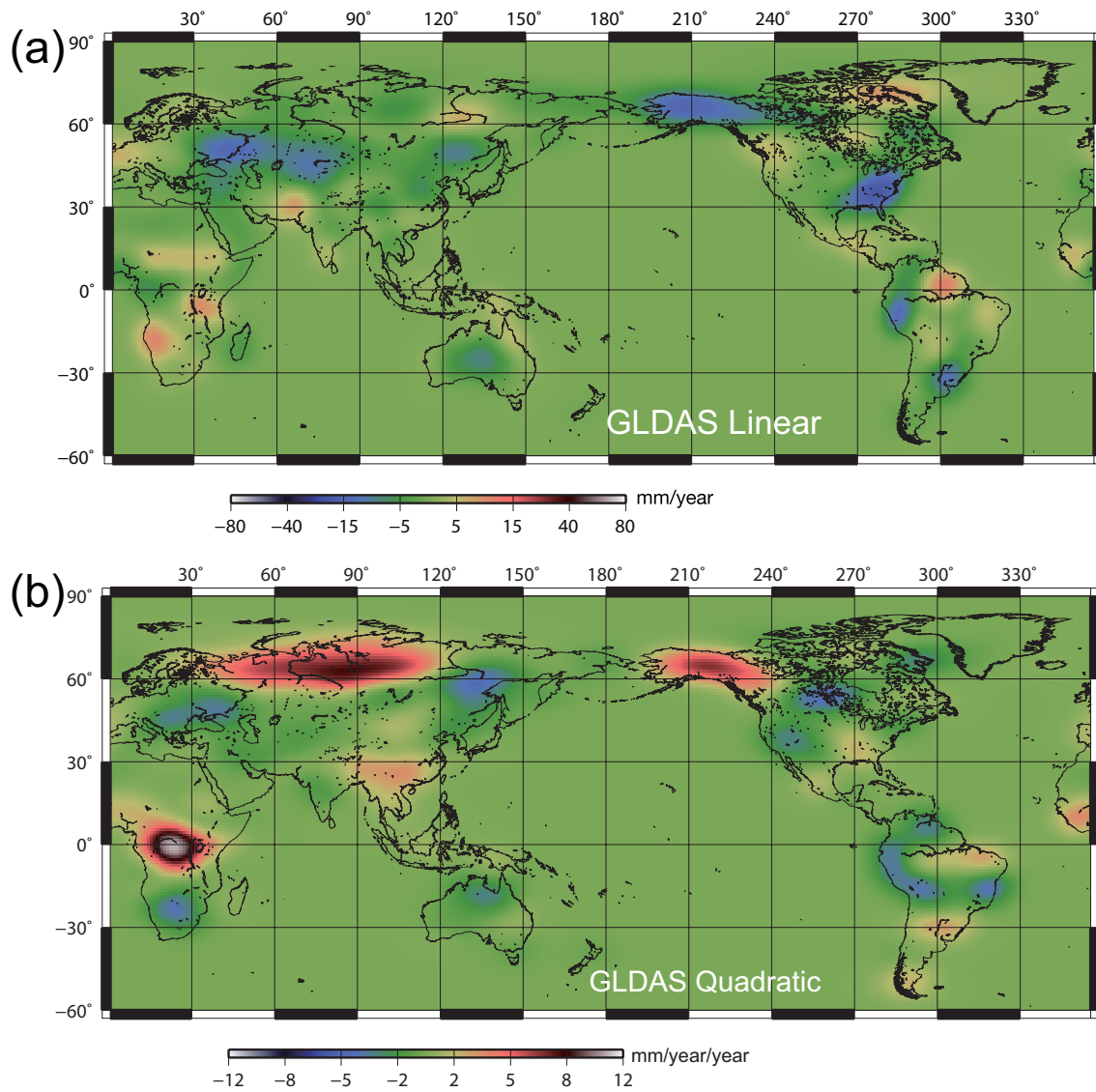
Fig. 4.8: Same as Fig. 4.3, except for the GLDAS hydrological model output. Greenland and Antarctica are excluded.

central North America and Alaska. Similarly, deceleration signals (in blue) are seen in both cases
in Eastern Europe and Southern South America. On the other hand, their amplitudes are somewhat
different, and the differences tend to be larger in regions near large rivers. In general, the GLDAS
values are on a smaller side, suggesting an underestimation of the hydrological model on the inter-
annual and longer timescale. One common reason for such a model underestimation is the fact
that the adopted models tend to be conservative and revert to the climatology when and where
actual data are weak or inadequate. Moreover, in the present case, the anomalies in P lead to, and
hence are largely offset by, opposite changes in R mainly due to the effects of rivers and partly
due to groundwater storage; the time constant of the latter is much longer than the former. As the
nominal depth of soil layers treated in GLDAS is 2 meters, groundwater is not considered in its
output. The present result may suggest that groundwater plays a non-negligible role in regulating
W on inter-annual timescales. As for signals in Antarctica, GRACE can only estimate linear and
quadratic changes. In Fig. 4.3, gravity of Pine Island Glacier in West Antarctica decreases rapidly.

For a case study in more detail, I focus on Eastern Europe in the comparison between Figs.
4.3 (b) and 4.8 (b), where the GRACE quadratic signal much exceeds that of GLDAS. This might
be partly because GLDAS, being a continental model, does not model Caspian and Black Seas.
Generally speaking, long-term gravity changes in oceanic areas are much smaller than those on
land. Relatively small oceans surrounded by continents, however, might show signals comparable
to land regions. For example both GRACE and altimetry detected relatively large seasonal signals
in the Mediterranean Sea [Garcia et al., 2006]. In fact, Swenson and Wahr [2007] showed a
positive trend in GRACE gravity in Caspian Sea up to 2006. Thus, I also analyze average mass
changes in Caspian and Black Seas with the GRACE data as shown in Swenson and Wahr [2006].
At first, I calculate spherical harmonics coefficients of land mask which shows the shape of an

object area.

$$\vartheta_{nm}^c = \frac{1}{4\pi} \int_0^{2\pi} \int_0^{\pi} \vartheta(\theta,\phi) P_n^m(\cos\theta) \cos m\phi \sin\theta d\theta d\phi$$

$$\vartheta_{nm}^s = \frac{1}{4\pi} \int_0^{2\pi} \int_0^{\pi} \vartheta(\theta,\phi) P_n^m(\cos\theta) \sin m\phi \sin\theta d\theta d\phi, \tag{4.4}$$

where,

$$\vartheta(\theta,\phi) = 1 \ (\text{ for inside }) \tag{4.5}$$

$$\vartheta(\theta,\phi) = 0 \ (\text{ for outside }) \tag{4.6}$$

There (θ, ϕ) means (colatitude,longitude). The integers n and m denote the degree and order, respectively. The P_n^m is the fully normalized associated Legendre-polynomials. This can be made using the source codes by Masanori Saito, available on line from the web page of the Geodetic Society of Japan (http://wwwsoc.nii.ac.jp/geod-soc/contents/book/program.html). Secondly, with $\Delta C_{nm}(t)$ and $\Delta S_{nm}(t)$ which express the deviations from the static Stokes coefficients of the GRACE data, time series of equivalent water thickness can be calculated:

$$\Delta water(t) = \frac{R\rho_e}{3\rho_w} \sum_{n=2}^{n_{max}} \frac{2n+1}{1+k_n} (\vartheta(\theta,\phi)\Delta C_{nm}(t) + \vartheta(\theta,\phi)\Delta S_{nm}(t)) \tag{4.7}$$

Adopted parameters ρ_e, ρ_w, k_n are the same parameters as described in Chapter 2.1. In this result shown in Fig. 4.9 (blue curves), clear deceleration signals (an increase up to ∼2005 followed by a decrease after ∼2006) are seen in both seas. Indeed, looking at the linear trend of precipitation [Fig. 4.6], precipitation decreases linearly in the whole regions. The changes of precipitation

should also be seen in the sea surface height (SSH). Therefore, I make use of the satellite ocean altimetry data from AVISO (http://www.aviso.oceanobs.com/en/data/products/sea-surface-height-products/global/index.html) to compare directly with GRACE quadratic changes. I multiply an empirical factor to the SSH in accordance with Swenson and Wahr [2007]. Their agreement shall not be expected because GRACE data only reflect the mass variation while the altimetry gives the total SSH which also includes the steric contribution. Nevertheless, a similar deceleration (actually "acceleration" of decrease) is also present in the altimetry data for Caspian Sea [Figs. 4.9, 4.10]. SSH in Black Sea shows similar but weaker deceleration. Its seasonal amplitude is also significantly smaller than that in GRACE. This may be because Caspian Sea, being a closed water basin, would have accumulated, or integrated, such trend more effectively than did Black Sea, which is connected (although indirectly) to the global ocean system. The phases are seen to differ between mass changes from the GRACE data and sea surface height from the altimetry data. This difference suggests that it takes some time for the thermal expansion to occur.
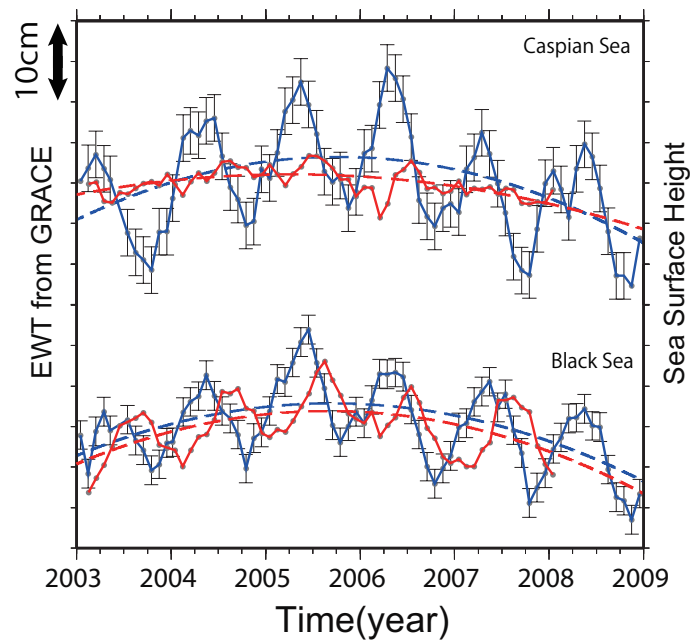
Fig. 4.9: Time series of EWT in Caspian Sea (top) and Black Sea (bottom). Blue curves show the mass changes from GRACE gravity data in the two regions. Red curves show the corrected sea surface heights from AVISO at arbitrary points in these regions. Dashed curves show best-fit quadratic functions.
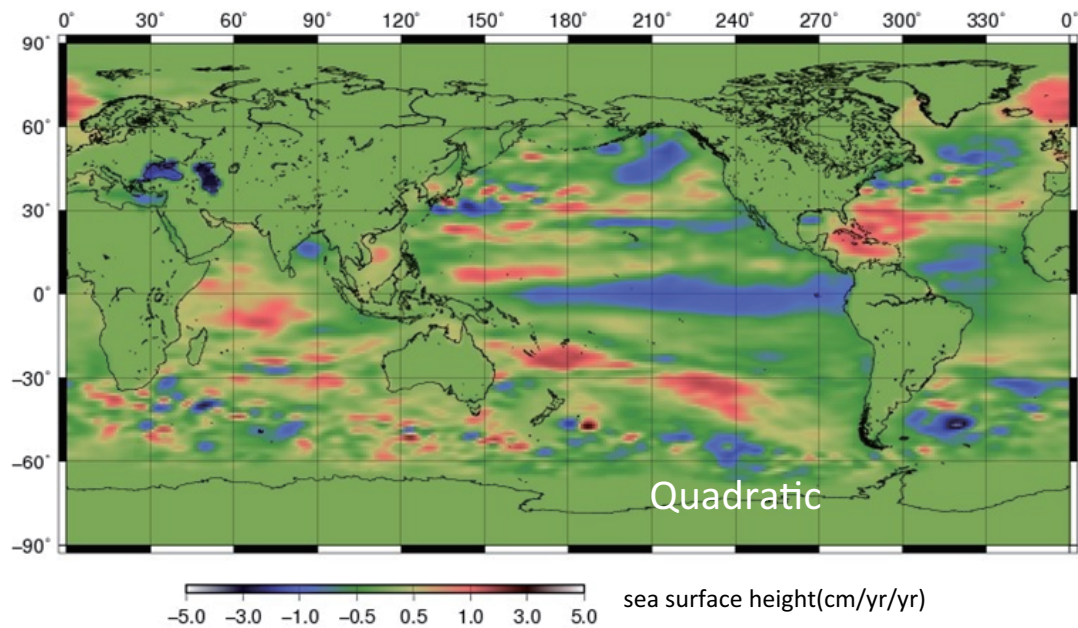
Fig. 4.10: Distribution of Quadratic terms in sea surface height changes from altimetry data. Deceleration signals are seen in both of Caspian Sea and Black Sea.

4.6 Conclusions

With the GRACE data over 7 years, I find that a quadratic variation of TVG is significant both in wavenumber and space domains. Quadratic terms are significant in many regions, including equatorial Africa, Eastern Europe, central North America, Southeast Asia and Amazon basin, whereof I need to specify epochs in discussing TVG trends. Comparison with meteorological data suggests that the trends of P have a similar distribution to W, according to GRACE although I still lack accurate knowledge of inter-annual changes in E and R to study fully the continental water storage. Nevertheless, I confirm that the quadratic term in TVG would be a manifestation of the linear trend of P. Hydrological model GLDAS, which includes E and R, also shows geographical patterns of linear and quadratic changes in intriguing agreement with those of GRACE in major

areas. GLDAS tends to underestimate the inter-annual changes of W, which may suggest the inadequacy of GLDAS in modeling the contribution of groundwater transport. The comparison indicates for the first time that both the GRACE observation and the GLDAS hydrological model are monitoring the inter-annual variability by yielding qualitatively "correct" estimates for inter-annual mass variations. Further quantitative comparisons of the acceleration/deceleration terms will provide independent assessment as to the quality and validity of the hydrological models for inter-annual applications.

5 Seasonal and inter-annual gravity changes in the Siberian permafrost region from GRACE

5.1 Introduction

The inter-annual gravity trends [Fig. 2.12] in Chapter 2 show clear increases in Canada and Scandinavia due to glacial isostatic adjustment (GIA), a delayed viscous response to melting of past ice sheets. In addition, global warming seems to cause gravity decrease in many places due to present-day melting of glaciers and ice sheets, for example, Greenland [Velicogna and Wahr, 2006], Alaska [e.g. Chen et al., 2006], Patagonia [Chen et al., 2007b] and Asian high mountains [Matsuo and Heki., 2010]. Their rates of ice loss observed by GRACE are, 248 ± 36 gigaton (Gt)/yr in Greenland, 101 ± 22 Gt/yr in Alaska, 27.9 ± 11 Gt/yr in Patagonia, and 47 ± 13 Gt/yr in Asian high mountains, respectively. Such changes in the ice mass on land cause global sea level rise. According to the IPCC 4th Assessment Report [Bindoff et al., 2007], about a half of the observed sea level rise during 1993–2003 can be explained by thermal expansion, while the other half is due to melting land ice. Lemke et al. [2007] suggested that surface air temperature will increase by ~5 degrees in 100 years in the Arctic region due to global warming. Such a climate change may affect not only ice sheets and mountain glaciers but also the permafrost distributed over the extensive Arctic area.

Lena, Yenisei and Ob are the three largest Eurasian Arctic rivers running through the Siberian permafrost region [Fig. 5.1, Fig. 5.2]. There, increasing discharge to the Arctic ocean is observed (~ 2.0 gigaton/yr) [Peterson et al., 2002]. On the other hand, inter-annual gravity trends [Fig. 2.12] show significant mass increases in these river basins. GIA activity is considered to be absent in central-eastern Siberia, even though it lies in the same latitude band as Canada or Scandinavia
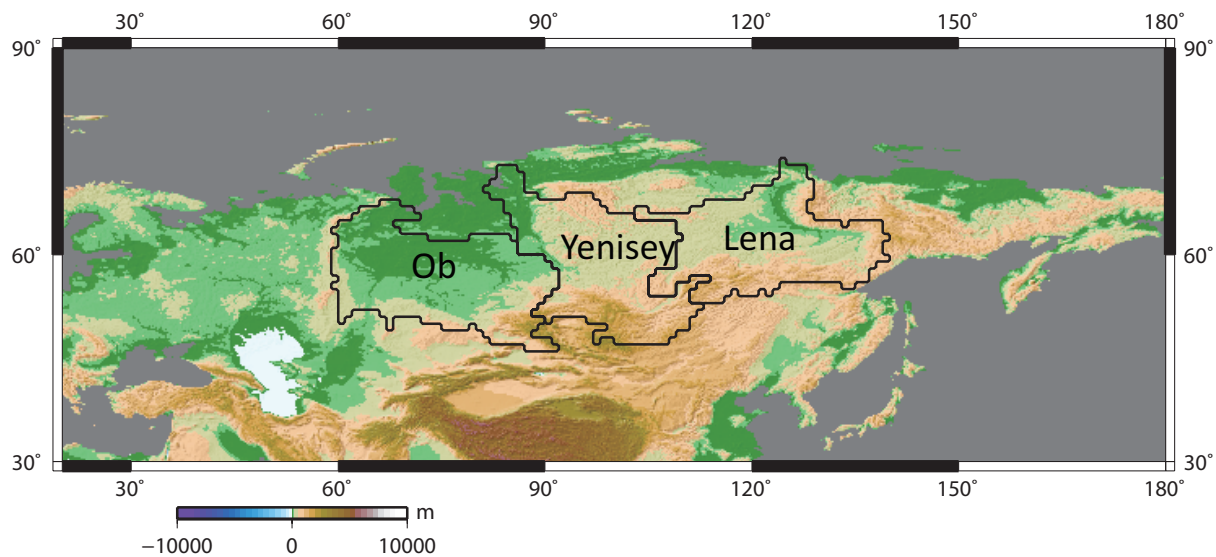
Fig. 5.1: Topography of Siberia and the three major river basins.
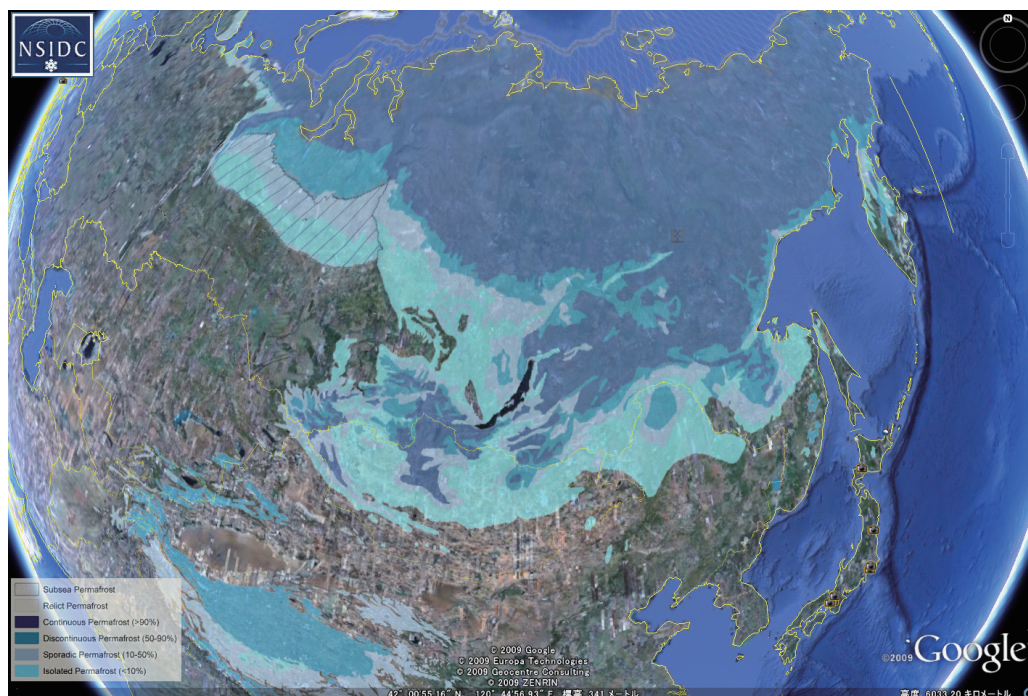
Fig. 5.2: Distribution of permafrost. Darkest blue shows continuous permafrost. Darker Blue and white show discontinuous, sporadic permafrost. Blue shows isolated permafrost

because this region has very thick permafrost. The permafrost thickness reaches a few hundreds of meters here, which reflects the absence of an ice sheet in the last glacial maximum (LGM), i.e. lack of ice cover enabled deep penetration of the cold temperature. The reason why this region was not covered by an ice sheet is the small precipitation. Actually, the central-eastern Siberia is the driest region in the world covered with forest [Sugimoto et al.,2003]. The annual precipitation there is only ~ 200mm. Indeed, the currently accepted past ice model, ICE-5G (VM2) [Peltier, 2004], does not consider GIA signals in Siberia [Fig. 5.3].
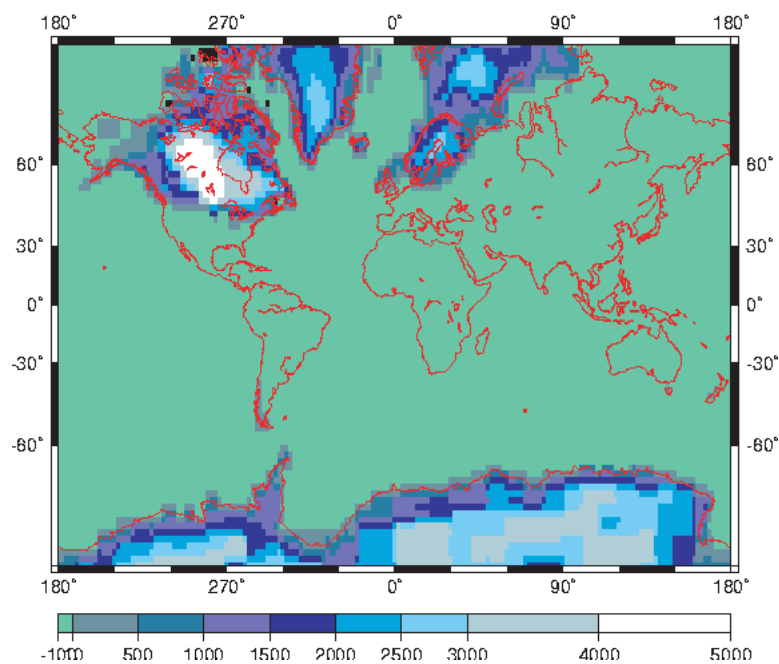
Fig. 5.3: Thickness of ice cover in the ICE-5G Model at the last glacial maximum. [Peltier, 2004]

Consequently, the observed increase of gravity in Siberian permafrost regions may be of hydrological origins. Hydrological dynamics in permafrost regions is peculiar because the impermeability of frozen soil prohibits melt water from migrating into depth. Moreover, excess water from summer rains does not always run off, but can be stored as ice lens during winter. Such

water could be used in the next dry summer, and stabilize the Taiga forest in such a dry region

[Sugimoto et al., 2003]. The response of permafrost to global warming is an important issue, but

has not been addressed sufficiently. Now that GRACE can observe water storage directly, we try

to discuss hydrological dynamics in the permafrost region in the recent warming environment.

5.2 Data and Processing

5.2.1 water budget

We will compare water storage obtained by two independent data sets in the three river basins

(Lena, Yenisei, Ob). Change in water storage (ΔW) is expressed by the following equation, similar

to eq. (4.2).

$$\Delta W = \int_{t_0}^{t_1} (P - E - R)dt, \tag{5.1}$$

where ΔW is the increase terrestrial water storage in a month, P, E and R are the precipitation,

evapotranspiration, and runoff, respectively. GRACE can observe, W, the water storage. On the

other hand, water storage can be estimated from eq. (5.1) by integrating the $(P - E - R)$, ground-

based observation data. Here t_0 and t_1 are the first and the last days of the month. Monthly

worldwide precipitation (P) data are available from CMAP (Climate Prediction Center Merged

Analysis of Precipitation) at 2.5×2.5 degree grids, as explained in Chapter 4. Runoff (R) obser-

vation data in the Arctic regions are available from http://rims.unh.edu/. We assume that discharge

at river mouth represents the total discharge in the river basin. This data set provides runoff in

volume per unit time (m^3/s). We convert it into monthly runoff height (mm/month) by dividing

it with the drainage area. As we mentioned in Chapter 4, evapotranspiration (E) is difficult to

measure. According to Hamon [1963], potential evapotranspiration (PET) can be calculated by

putting data such as temperature, hours of sunlight and precipitation into the following equation:

$$PET = 29.8 \cdot D \cdot \frac{e^*}{T + 273.2}, \tag{5.2}$$

where D is the hours of sunlight (hour), T is temperature(°C) and e^* is saturation vapor pressure (kPa). The hours of sunlight, D, can be calculated as follows [Dingman, 2002]:

$$D = \frac{2 \cos^{-1}[-\tan(\delta) \cdot \tan(\Lambda)]}{\omega} \tag{5.3}$$

where δ and Λ are declination and latitude, respectively. ω is the angular velocity of the Earth's rotation (= 0.2618 rad/hr). δ is given by this equation:

$$\delta = \frac{180}{\pi} \cdot [0.006918 - 0.39912 \cdot \cos(\Gamma) + 0.070257 \cdot \sin(\Gamma)$$

$$-0.006758 \cos(2\Gamma) + 0.000907 \sin(2\Gamma)$$

$$-0.002697 \cos(3\Gamma) + 0.00148 \sin(3\Gamma)] \tag{5.4}$$

where Γ, the day angle, can be calculated with the day number of the year, J,

$$\Gamma = \frac{2 \cdot \pi \cdot (J - 1)}{365} \tag{5.5}$$

At latitudes greater than 66.5°, the absolute value of $[-\tan(\delta) \cdot \tan(\Lambda)]$ can exceed unity. In this case, D should be zero or 24 because there is neither sunrise in winter nor sunset in summer. In order to calculate PET, e^* also should be known. We used temperature data from NCEP (National

Centers for Environment Prediction). e^* can be calculated by the following equation;

$$e^* = 0.611 \cdot exp(\frac{17.3 \cdot T}{T + 237.3}).$$ (5.6)

According to Thornthwaite and Mather [1955], evapotranspiration (E) is proportional to potential evapotranspiration (PET), that is,

$$E = f \times PET,$$ (5.7)

where f is the reduction factor determined a-posteriori. This reduction factor can be calculated using the water budget method [Thornthwaite and Mather, 1955]. The appropriate value of f is obtained to achieve the seasonal balance between dW/dT and $P - E - R$, i.e.

$$\frac{dW}{dt} = P - E - R.$$ (5.8)

Evapotranspiration can be estimated by modifying the above equations as follows,

$$f \times PET = P - R - \frac{dW}{dt}$$ (5.9)

$$f = \frac{P - R - dW/dt}{PET}.$$ (5.10)

The reduction factor, f, depends on vegetation. Penman [1948] showed the annual average reduction factor was determined as 0.75 for southern England. According to Arai [2004], a value from 0.6 to 0.7 is used for Japan as the annual average reduction factor. Here we determine the factors f for the Lena, Yenisei and Ob river basins, respectively.

5.2.2 Signals in an interest area

Water storage, precipitation and evapotranspiration provides information on quantities at grid points while runoff data are averaged over river basins. In order to compare water storages observed by GRACE with those by ground-based data, averaged changes in the studied area have to be compared with changes at gridded points. As described in Chapter 1, the Gaussian filter is applied to GRACE data to reduce short wavelength noises. Such filtering leads to signal leakage across the border of the region of interest. For example, Fig. 5.4 shows how signals changes with different averaging radius. There, I apply the eq. (4.4) to the shape assigning 1 for ocean and 0 for land, and recover gridded map. In order to compare the water storage observed by GRACE with that by ground-based data directly, the same Gaussian filter should be applied to ground-based data. In order to solve these problems, we need to (1) make a land mask which shows the shape of each river basin and (2) calculate averaged time-series of water storage from the GRACE data and the ground-based data with the same land mask and Gaussian filter.

As for (1), I make $1° \times 1°$ land mask, which has values 1 within the studied region and 0 outside it, using free Geographic Information System (GIS) software, Geographic Resources Analysis Support System (GRASS). GRASS can choose an arbitrary watershed area and make a set of gridded data, $\vartheta(\theta, \phi)$. In order to do (2), I convert $\vartheta(\theta, \phi)$ into the spherical harmonic coefficients, ϑ_{nm}^c, ϑ_{nm}^s, with eq. (4.4). With ϑ_{nm}^c and ϑ_{nm}^s, I obtain averaged time series of EWT from the GRACE data in each river basin by applying eq. (4.4). As for the ground-based data, I recover gridded map $mask(\theta, \phi)$ with Gaussian filter:

$$mask(\theta, \phi) = \sum_{n=2}^{n_{max}} \sum_{m=0}^{n} W_n W_m (\vartheta_{nm}^c + \vartheta_{nm}^s), \tag{5.11}$$

where W_n and W_m are the same filter weights for coefficients of degree n and order m. Here we
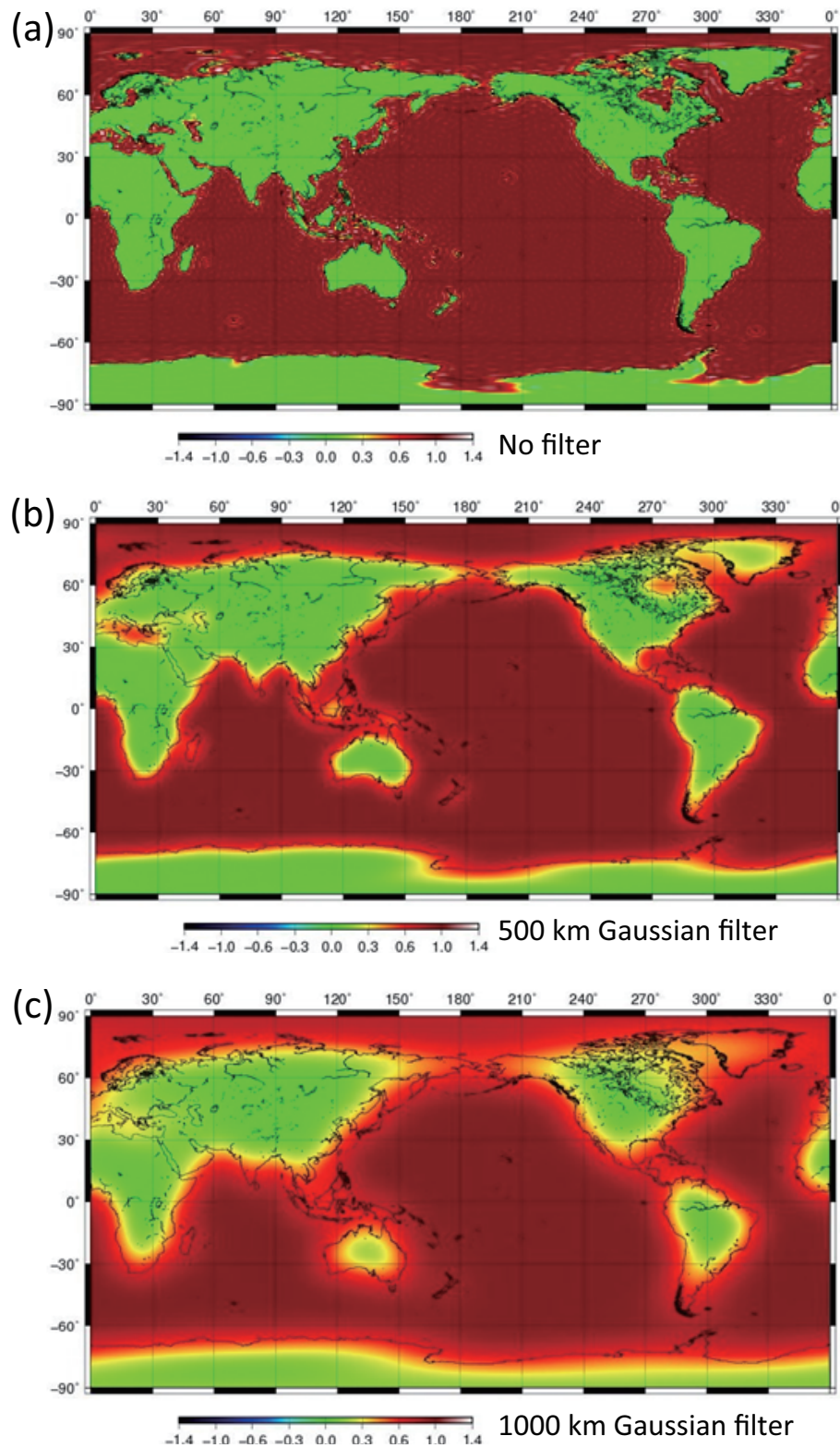
Fig. 5.4: Comparison of the signal leakages with different averaging radii. Here I assign 1 within the region of interest, and zero outside [Top].

use 300 km averaging radius for W_n and W_m to both GRACE and ground-based data.

By multiplying $mask(\theta, \phi)$ by precipitation or evapotranspiration gridded data $f(\theta, \phi, t)$, averaged time series of EWT from ground-based data can be obtained in each river basin

$$\Delta E\bar{W}T(t) = \frac{1}{S} \int \int_s f(\theta, \phi, t) \cdot mask(\theta, \phi) \sin \theta d\theta d\phi, \tag{5.12}$$

where S is the drainage area. After getting the average time-variable water storage, precipitation, evapotranspiration and runoff, I compare water storage from gravity data and from ground-based observations in seasonal and inter-annual timescales.

5.3 Average seasonal changes in the Siberian permafrost region

Before discussing seasonal water budget in the Siberian permafrost region, I define winter as the period from November to April and summer from May to October. Due to impermeability of frozen soil, permafrost and non-permafrost rivers have different hydrological dynamics. In the permafrost, high discharge is seen in summer due to snow melt, and discharge is very low during winter [Ye et al., 2009]. Therefore, the model shown by the eq. (2.11) in Chapter 2 is not enough. Here I obtain its average seasonal changes using the 2003 – 2008 data of GRACE gravity and ground-based observations in each basin [Figs. 5.5, 5.6, 5.7].

We discuss water budget in a river basin using four parameters as mentioned in eq. (5.1) in general. So far, it was very difficult to observe water storage and evapotranspiration while precipitation and runoff can be observed with ground-based observations. Now GRACE can measure water storage directly, and this makes it possible to constrain evapotranspiration by eq. (5.10). When we adopt 0.400 and 0.565 as the *E/PET* factor (f) for the Lena and Ob river basins, respectively, water storage curves from the GRACE data (gray curve) and ground-based data (black
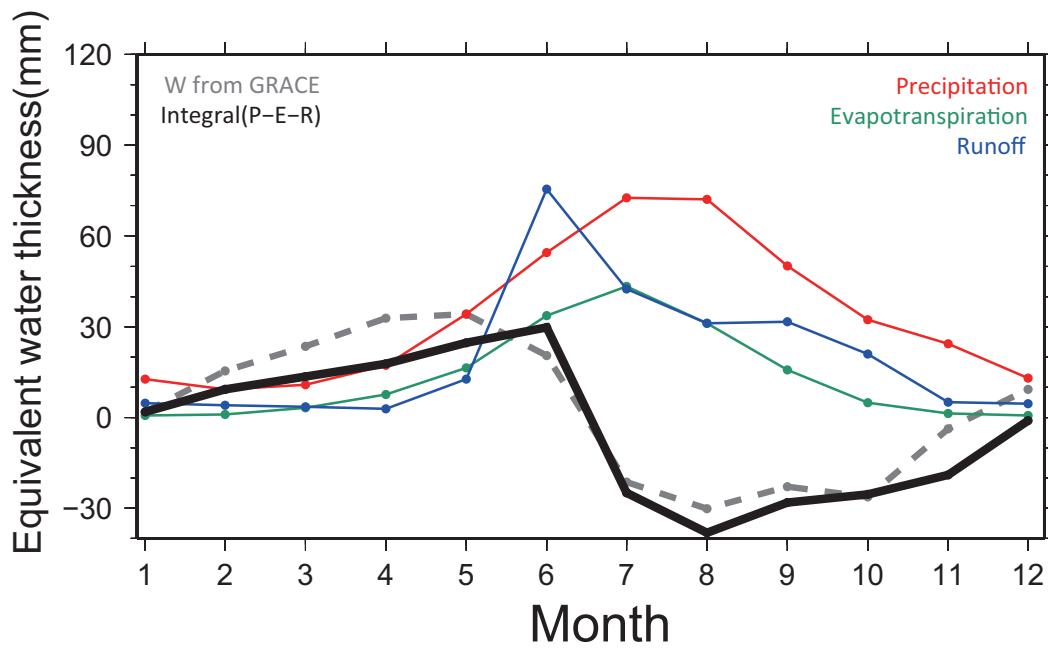
Fig. 5.5: Average seasonal changes in the Lena river basin. It shows good agreement when the reduction factor ($f = E/PET$) for evapotranspiration is 0.400.
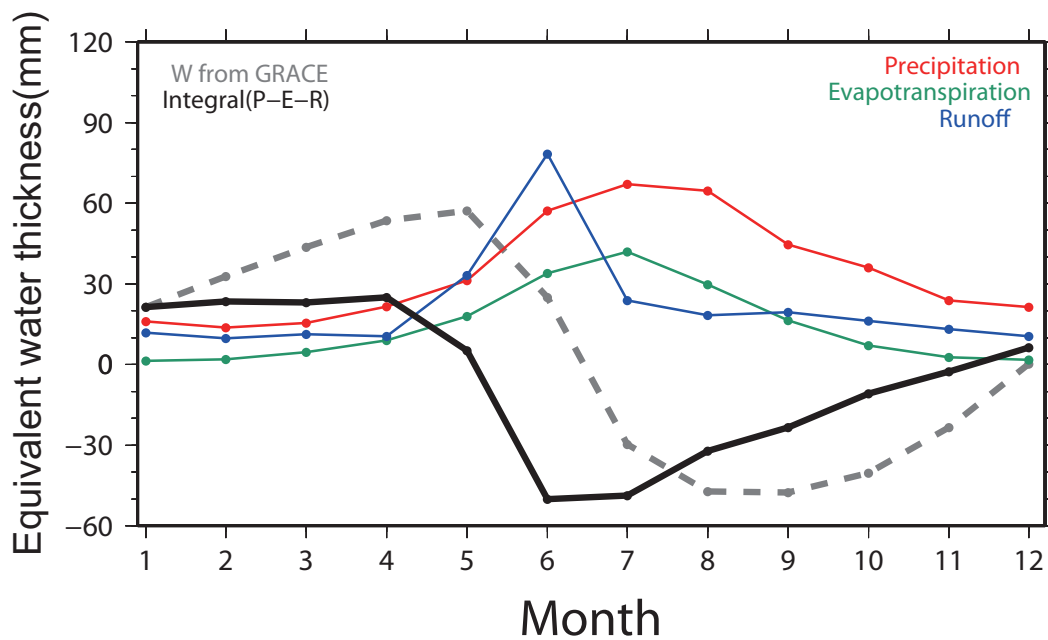
Fig. 5.6: Average seasonal changes in the Yenisei river basin. It shows poorer agreement even with the most suitable reduction factor (f) of 0.330.

curve) show good agreements for these river basins [Figs. 5.5, 5.7]. The value of 0.400 and 0.565 are smaller than those shown in Penman [1948] and Arai [2004]. This may come from the difference of climate and vegetation.

Looking at the relation between water storage and water fluxes in the Lena river basin [Fig. 5.5], for example, we can see that accumulation of snow is directly reflected in water storage because discharge is very small due to frozen soil. In the spring thaw, high peak of discharge and sudden increase of evapotranspiration let the water storage drop rapidly. In early summer, a large amount of evapotranspiration and runoff let water storage slowly decrease. However, water storage starts to increase in late summer when summer precipitation exceeds the evapotranspiration and runoff, and starts to fill the dry soil. It is notable that the characteristic hydrological dynamics in the permafrost can be seen in the gravity data.
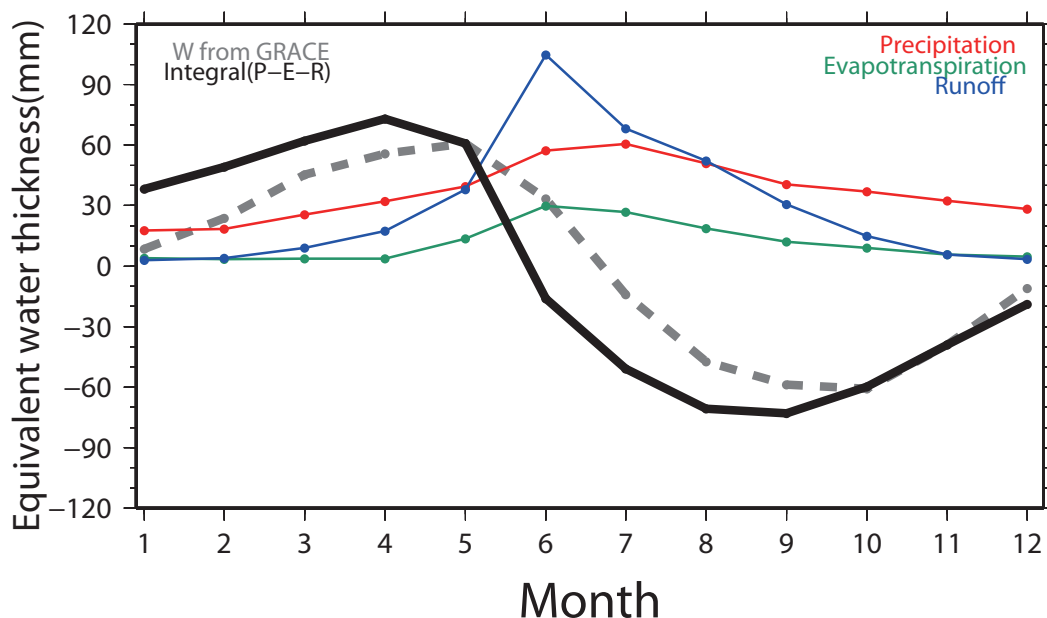
Fig. 5.7: Average seasonal changes in the Ob river basin. it shows the best agreement when the reduction factor f was 0.565.

However, it shows poorer agreement for the Yenisei river basin even with the most suitable reduction factor (f) of 0.330 [Fig. 5.6]. In order to see what is responsible for the poor agreement, I split the studied region into the upstream and downstream regions at a point shown in Fig. 5.8 (b). I then calculated averaged seasonal changes in upper and lower regions separately [Figs. 5.8 (b), 5.9]. The downstream region of the Yenisei river shows a reasonable agreement. However, the upstream region showed a fairly bad agreement. The poor agreement as seen in Fig. 5.6 may hence come from the upstream region. There are several large-scale hydroelectric dams in the upper region of the Yenisei river. Among others, the Bratsk reservoir and the Krasnoyarsk reservoir are one of the largest reservoirs in Siberia with 169 km^3 and 73.3 km^3 water capacities [Yang et al., 2004]. In Fig. 5.9 (a), we can see that the runoff does not show sharp increase associated with the spring thaw because upper region of the Yenisei river does not freeze. The runoff shows stationary values throughout a year there owing to the regulation of the flow by the dams. The shapes of the Bratsk and the Krasnoyarsk reservoirs are located very close the border of the river basin area. GRACE signals from these dams might have been partially suppressed because we used a spatial averaging filter.
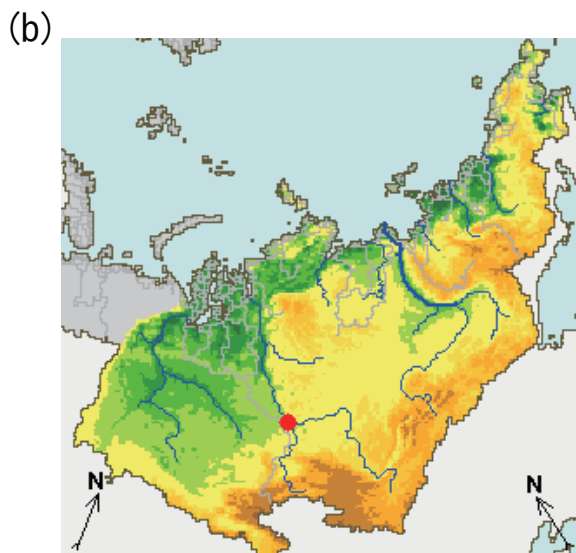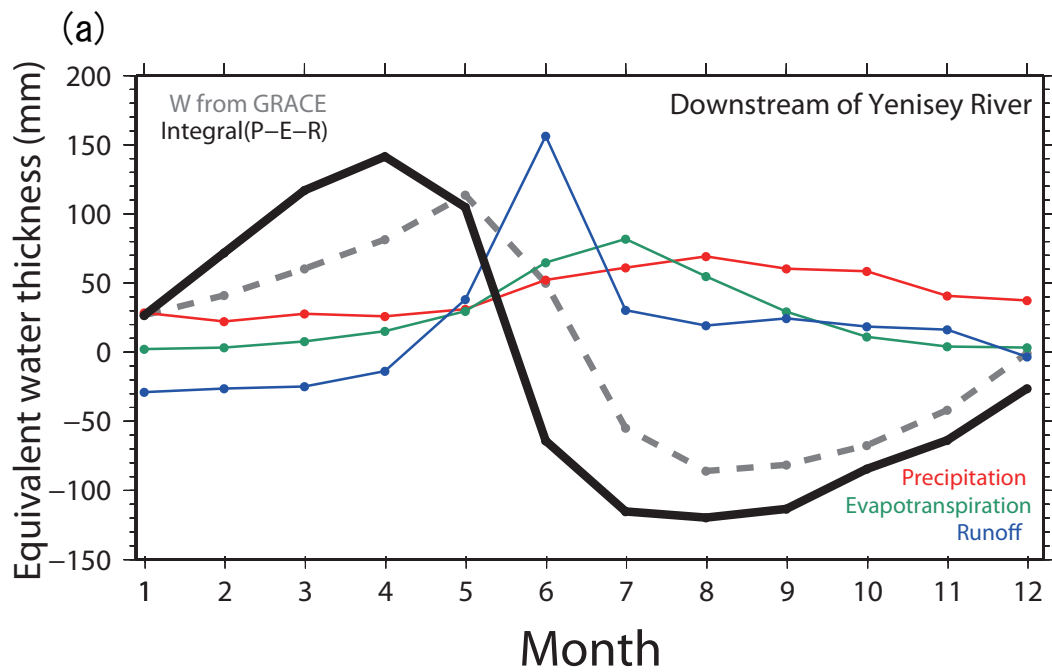
Fig. 5.8: (a) Average seasonal changes in the downstream of the Yenisei river basin. The dividing of the downstream and upstream part is shown by the red dot point in map (b) [http://rims.unh.edu/data.shtml]. The reduction factor f was assumed to be 0.750.
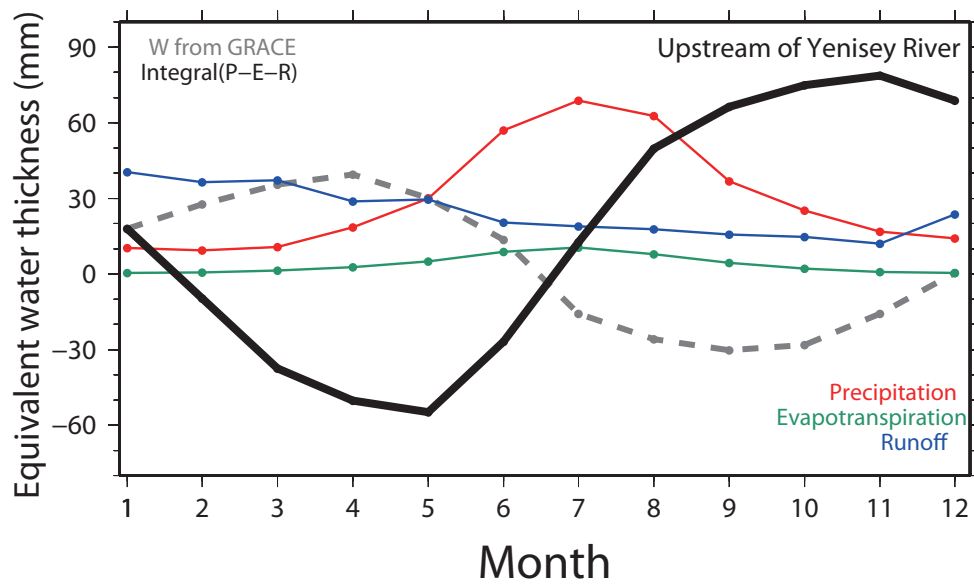
Fig. 5.9: Average seasonal changes in the upstream of the Yenisei river basin. The reduction factor f was assumed to be 0.100, but this value hardly makes sense since it does not close the water budget.

5.4 Increase of water storage in Siberia

While the melting of ice glaciers and ice sheets on land contribute to sea level rise, GRACE data show that significant inter-annual mass increase has occurred in the Siberian permafrost region over the last 7 years [Fig. 5.11]. The mass increase of these river basins are 30.7 gigaton/yr, 12.9 gigaton/yr, and 9.6 gigaton/yr in the Lena, Yenisei, and Ob river basins, respectively [Fig. 5.10]. The total increase is comparable to a half of the annual glacial mass loss in Alaska. Chao et al., [2008] suggested that water impoundments in artificial reservoirs worldwide significantly reduced the rate of global sea level rise. The Siberian permafrost might play the same role, impounding water and reducing global sea level rise as a huge natural reservoir.
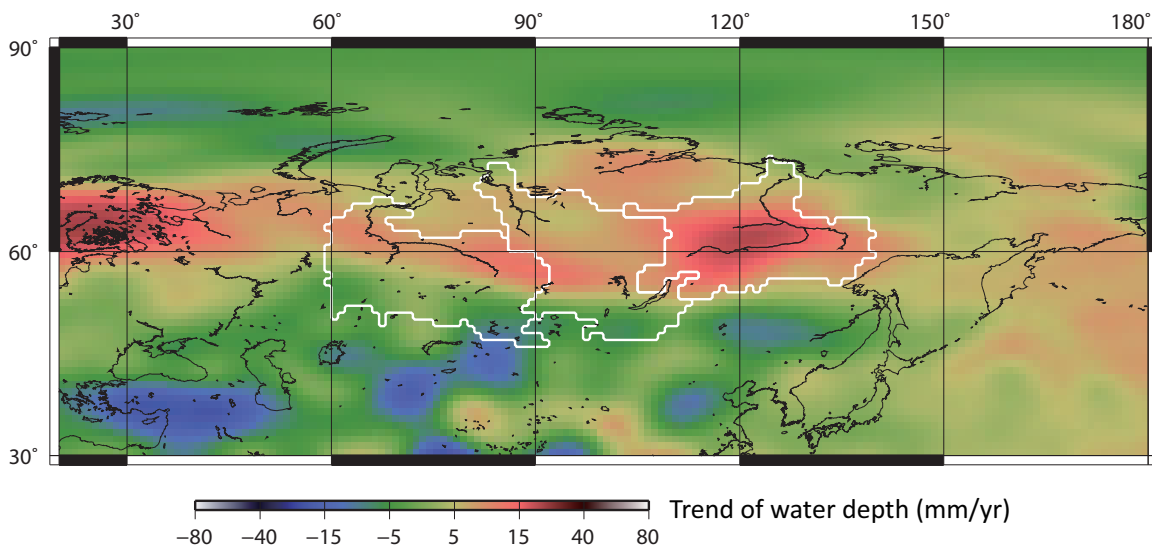
Fig. 5.10: Inter-annual change of equivalent water thickness using GRACE data. GRACE shows significant inter-annual mass increases in the three river basins over the last 7 years (30.7, 12.9, and 9.6 Gt/year in the Lena, Yenisei, and Ob river basins, respectively.)

Here we integrate $P - E - R$ to derive changes in W, which can be compared with the GRACE data. Since runoff data in the Yenisei river basin may have some problems as described in the previous section, I discuss only the Lena river basin and the Ob river basin. Figs. 5.12 and 5.13

suggest that the two data sets of independent origin show good agreement both in the intra- and inter-annual changes in the Lena river basin. The rates of mass increase are 10.68 ± 1.15 mm/yr from GRACE and 11.8 ± 1.1 mm/yr from the integration of $(P - E - R)$ there. On the other hand, the Ob river basin shows an increase trend by 6.79 ± 1.96 mm/yr from GRACE and 14.8 ± 1.67 mm/yr from the ground-based observations. It does not agree well, but the both data sets show clear linear increase there.

Although the GRACE data can go back only to 2003, the ground-based data are available from 1990 to present. Applying the same reduction factor for E to data before 2003, we could discuss how water storage (i. e., integral of $(P - E - R)$) has changed since 1990 [Figs. 5.14, 5.15]. Comparison between water storage in the Lena river basin and global surface temperature anomaly from NCDC [Figs. 5.14, 5.15] suggests that the water storage tends to increase in accordance with the global surface temperature. Especially, in the large ENSO episode during 1997-1998, the water storage shows a remarkable increase. In contrast, the Ob river basin does not show such a significant correlation between water storage and temperature.

Next I consider the reason why the water storage is increasing in the Siberian permafrost region, especially in the Lena river basin. Recent precipitation shows marked increase in the Lena river basin [Fig. 5.16]. Blue and red curves show monthly and annual precipitation data, respectively. As precipitation increases, runoff also increases, and the time series of runoff in the Lena river basin [Fig. 5.17] show steady increases. According to Iijima et al., [2009], increased precipitation enhances soil temperature, and their in-situ observation confirmed such increases at points near Yakutsk in eastern Siberia. They suggested the two mechanisms to increase soil temperature, i.e. (1) higher insulation effects of the snow from atmospheric cooling, and (2) the increased latent heat of wet soil due to increased precipitation.
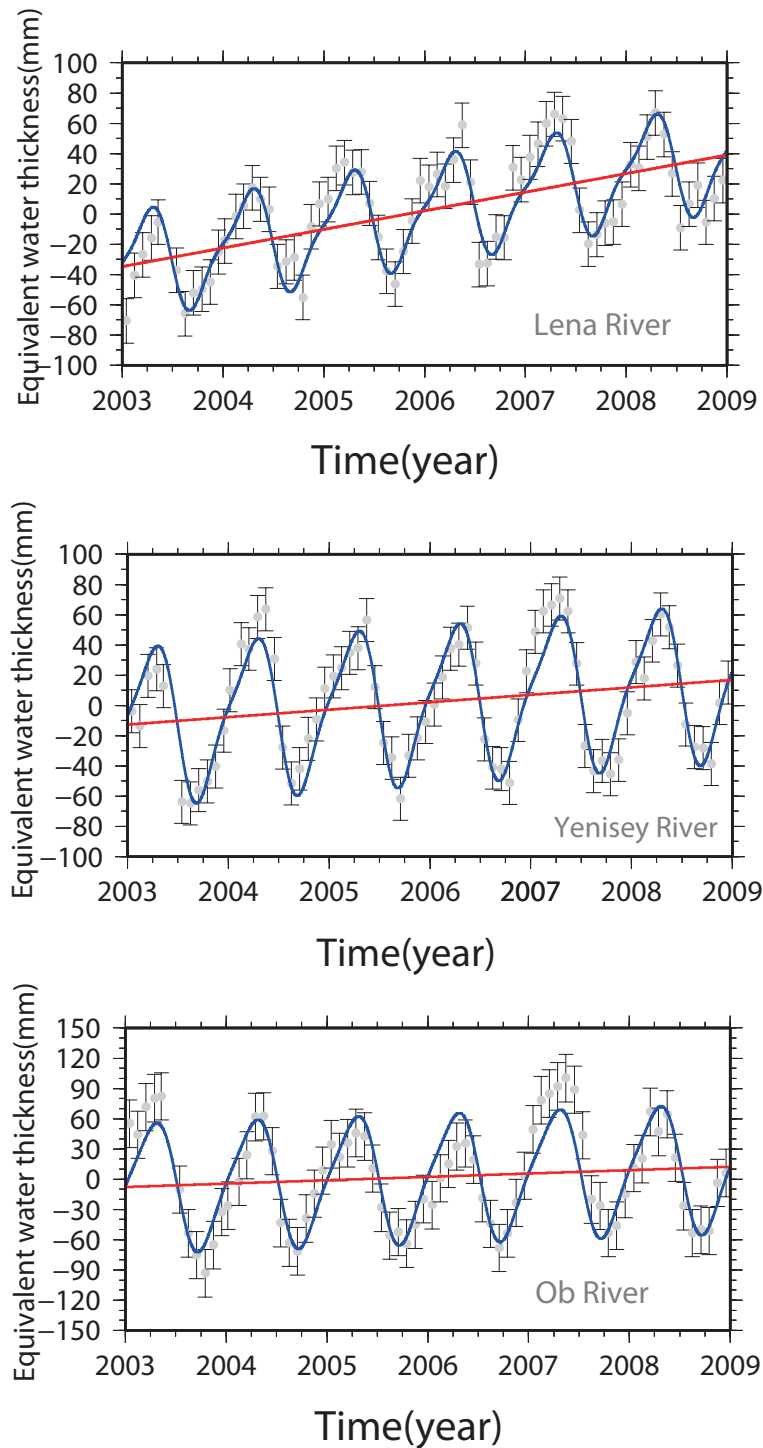
Fig. 5.11: Time series of water storage in the Lena (top), Yenisei (middle), Ob (bottom) river basins from the GRACE data. Blue curves are modeled with linear and seasonal changes. Red lines show estimated linear trends in individual river basins.
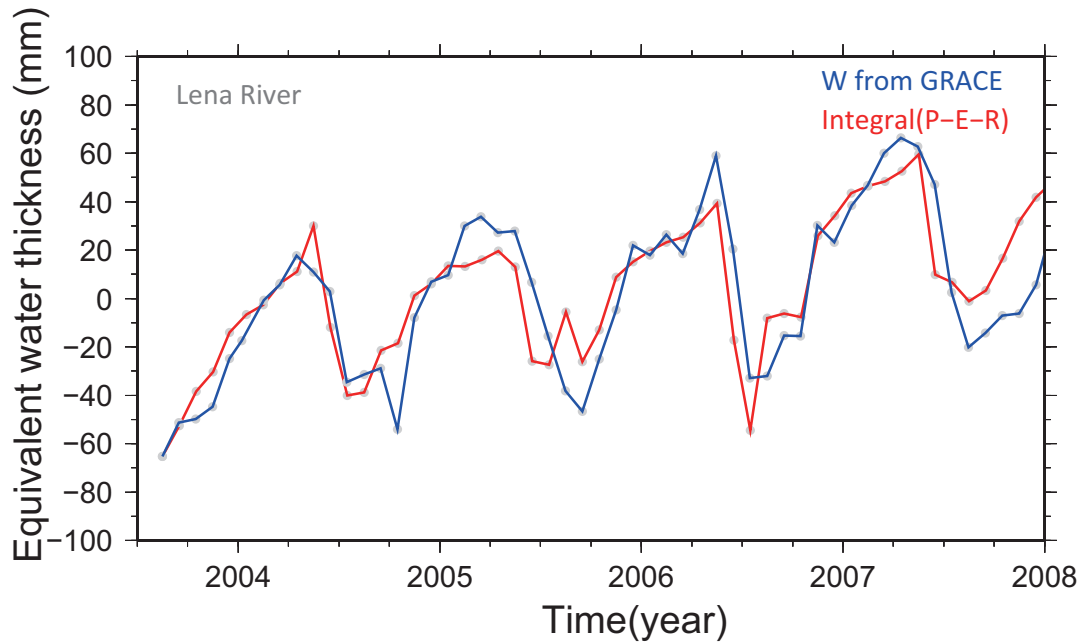
Fig. 5.12: Inter-annual water storage variation in the Lena river basin
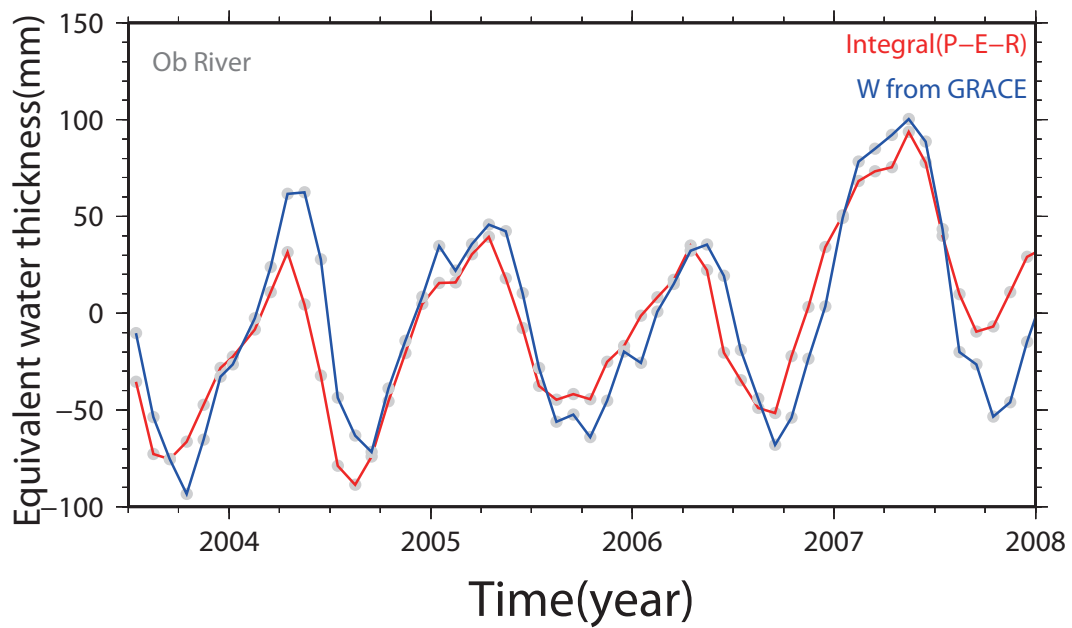
Fig. 5.13: Inter-annual water storage variation in the Ob river basin
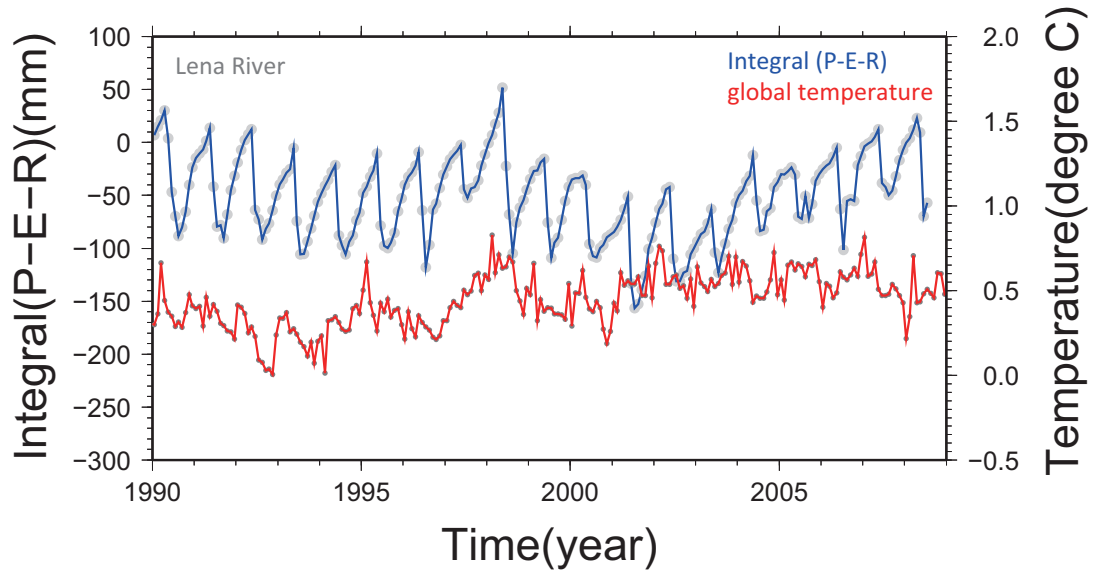
Fig. 5.14: (Blue) Time-series of water storage since 1990 derived from precipitation, evapotranspiration and runoff data in the Lena river basin. (Red) Time-series of global surface temperature anomaly from NCDC.
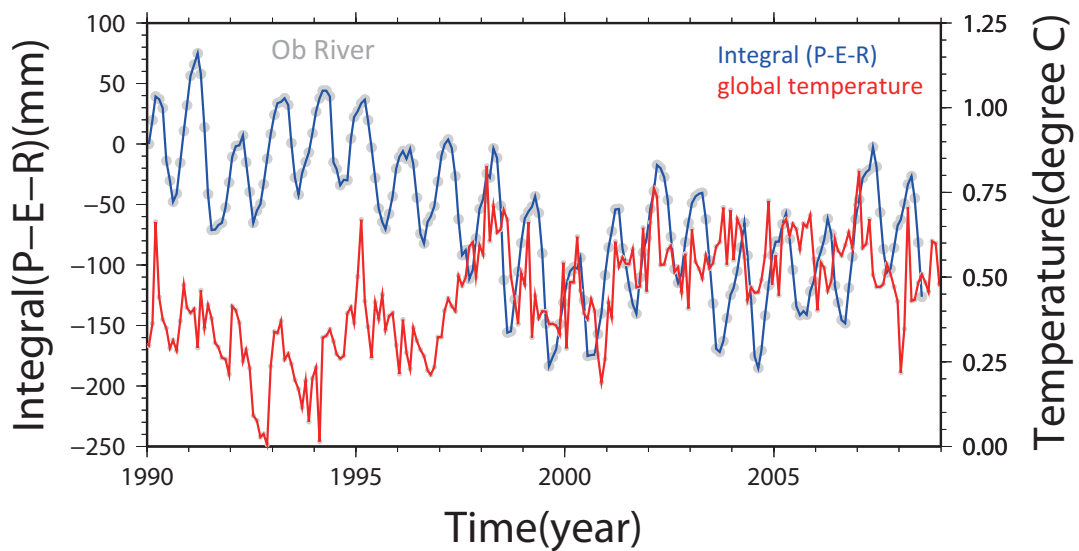
Fig. 5.15: (Blue) Time-series of water storage since 1990 derived from precipitation, evapotranspiration and runoff data in the Ob river basin. (Red) Same as Fig. 5.14.

Sugimoto et al. [2003] reported that the soil was almost saturated with water due to large amount of summer rains during August in 1999 at a point near Yakutsk by direct field observations. The current water storage level far exceeds the level in 1999 in the Lena river basin [Fig. 5.14]. Such a behavior might suggest the increase in the water capacity in permafrost. By repeating freezing and melting, "alas", a large depression, develops on the soil surface. Visual observations in Lena river basin tell us the areas of lakes within many alases are expanding for these years [Iijima et al., 2009]. This may contribute to store water on the soil surface.
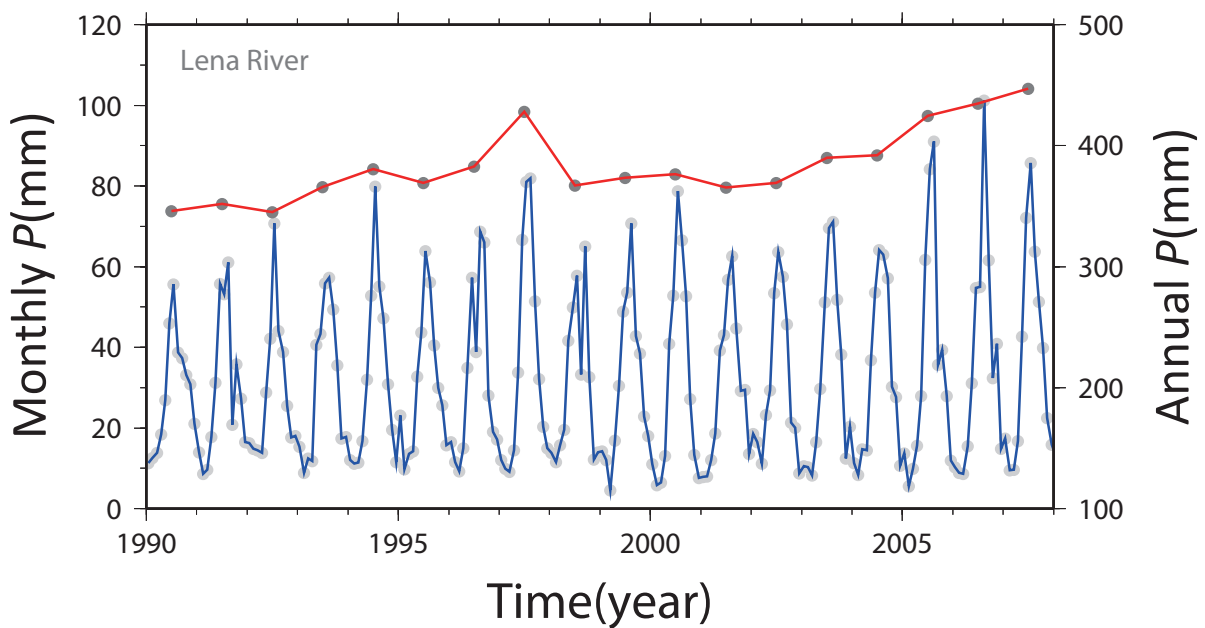
Fig. 5.16: Time series of precipitation in the Lena river basin. Monthly and annual precipitations are shown in blue and red, respectively.

In addition, about 80% of the Lena river basin is covered with continuous permafrost, whereas the Ob river basin has a permafrost coverage of only $\sim$ 30%[Fig. 5.2] [Papa et al., 2008]. Active layer is the layer near surface in permafrost that melts in summer and freezes in winter [Fig. 5.18]. Active layer plays an important role to help larch trees grow in such a dry environment. The layer
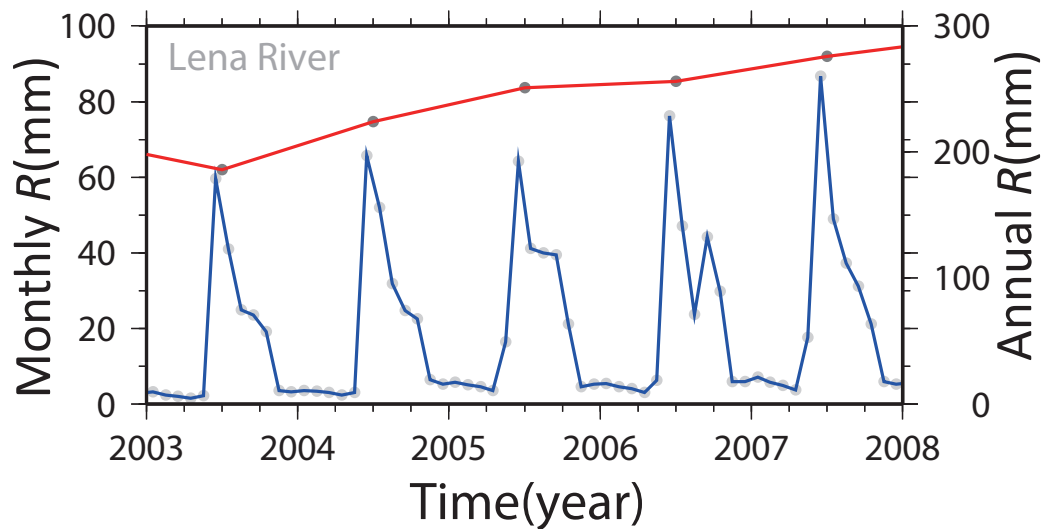
Fig. 5.17: Time series of runoff in the Lena river basin. Runoff has been increasing reflecting increasing precipitation in this region. Same as Fig. (5.16).

can keep soil water as ice over the winter, and this water can be used by the trees in the next summer when the amount of rains are insufficient [Sugimoto et al., 2002].

It is well known that the degradation of the permafrost influences global climate. For example, thickening of the active layer could trigger the release of significant amounts of greenhouse gases, e.g. methane, to the atmosphere [Fukuda, 1994]. In this study, I try to discuss how thickening of the active layer in permafrost influences the environment in terms of terrestrial water storage. According to the Iijima et al., 2009, the active layer has been thickening by ~ 4.9 cm/year from 2003 to 2007. Assuming (i) the volume difference between ice and water of 8%, and (ii) saturate water content in soil (~ 1/3), the specific capacity of water storage could increase by up to ~ 1.3mm per year.

In order to see a relation between input parameter, P, and output parameters, E and R, I calculate annual input and outputs in the Lena river basin [Fig. 5.19] and the Ob river basin [Fig.
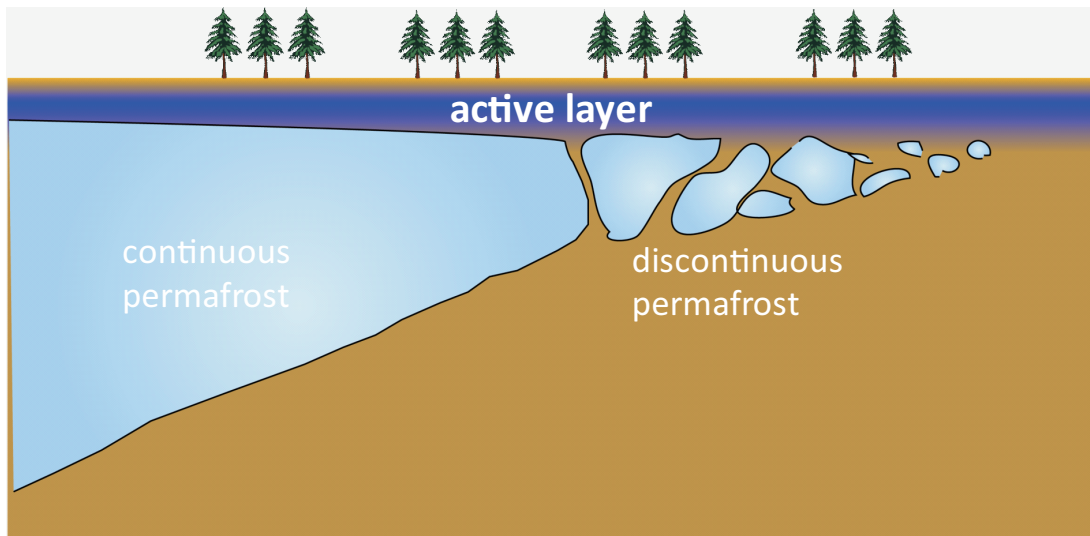
Fig. 5.18: The image of active layer in permafrost

5.20]. As shown in Fig. 5.20, sometimes input is higher than output, and output is higher in other times, keeping natural water balance. On the other hand, input has been higher than output all the time since 2002 in the Lena river basin. This result may suggest that increased water storage is caused by not only increased input but also increased water capacity.
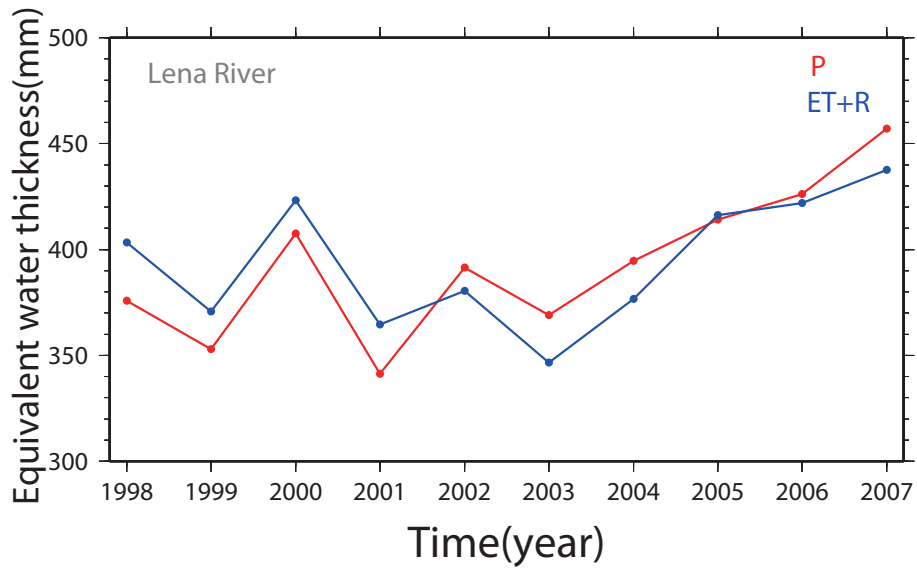
Fig. 5.19: The relationship between *P* and (*E+R*) in the Lena river basin.
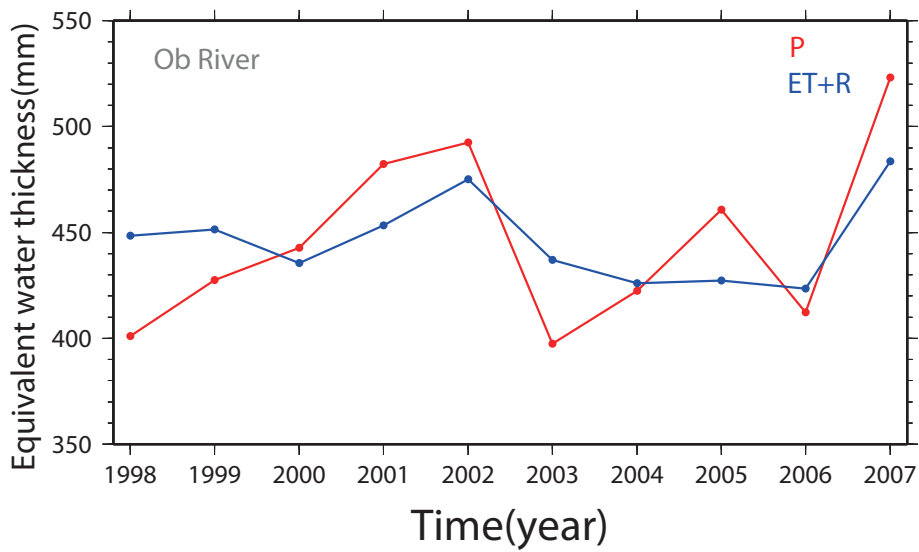
Fig. 5.20: The relationship between *P* and (*E+R*) in the Ob river basin.

5.5 Conclusions

Now that GRACE can observe terrestrial water storage directly, it enables us to discuss hydro-logical dynamics in places which has not been studied adequately such as permafrost regions. As for seasonal changes, water storage from GRACE gravity data and ground-based data show good agreement in the Lena and Ob river basins. The agreement was poor in the Yenisei river basin. This might be due to the water mass concentration at artificial reservoirs because our land masks are designed to evaluate water storage assuming constant EWT in the basin. In inter-annual timescales, three Siberian river basins show increasing trend in water storage, comparable to a half of the glacial mass loss in Alaska. The increase is the largest in the Lena river basin, which would have been caused by the two factors, i.e. increased precipitation, and increased water capacity. In the warming earth where ice melting lets sea level rise, Siberian permafrost might play a role to partially slow down this process by keeping large amount of water on its surface.

6 Conclusion

Using the GRACE data, I studied inter-annual, seasonal and transient changes in the Earth's gravity field. I summarize the main conclusions of this thesis as follows:

Chapter 3: Coseismic/postseismic geoid height changes due to the 2004 Sumatra-Andaman Earthquake

1. Coseismic and postseismic geoid height changes are detected by GRACE in the 2004 Sumatra-Andaman Earthquake.

2. The postseismic geoid height change is characterized by slow uplift with time constant of ~ 0.6year.

3. The postseismic changes can be explained by pore fluid diffusion (and partly by afterslip), but geoid changes by viscous mantle relaxation will emerge in future.

Chapter 4: Acceleration signals in GRACE time-variable gravity in relation to inter-annual hydrological changes

1. Significant acceleration and deceleration (quadratic) signals are found in the GRACE data both in wave number and space domains.

2. The trend of precipitation shows similar pattern to the quadratic changes in the GRACE data.

3. Spatial patterns of quadratic terms agree fairly well between the GRACE data and hydrological model outputs.

4. GRACE gravity data can provide independent assessment as to the quality and validity of the hydrological models for inter-annual applications.

Chapter 5: Seasonal and inter-annual gravity changes in the Siberian permafrost region from GRACE

1. Significant increases of water storage in the Lena and Ob river basins are found in the GRACE data.

2. Such increases are due to (1) the increase in precipitation, and (2) expansion of the soil water capacity.

3. The Siberian permafrost is accommodating large volume of water (a half of the glacial mass loss in southeastern Alaska) in its soil and on its surface.

4. Permafrost may partly reduce the global sea level rise by acting as a natural reservoir.

The GRACE mission launched in 2002 has made it possible to quantify time-variable gravity field globally for the first time. This is extremely important for comprehensive understanding of present day mass redistributions on and in the Earth. It expanded the application of gravity studies from a tool to study the Earth's interior to a new sensor to study hydrospheric and cryospheric dynamics. This "new eye" to see time-variable gravity would help us solve complex geophysical phenomena in various time and spatial scales.

7 References

Akaike, H., 1973. Information theory and an extension of the maximum likelihood principle. Proceeding of the Second International Symposium on Information Theory, Budapest, Akademiai Kiado, pp. 267-281.

Ammon, C.J., Ji, C., Thio, H.-K., Robinson, D., Ni, S., Hjorleifsdottir, V., Kanamori, H., Lay, T., Das, S., Helmberger, D., Ichinose, G., Polet, J., Wald, D., 2005. Rupture process of the 2004 Sumatra-Andaman Earthquake. Science 308, 1133-1139.

, 2004.   309pp.

Banergee P., Pollitz, F., Nagarajan, B., Burgmann, R., 2007. Coseismic Slip Distributions of the 26 December 2004 Sumatra-Andaman and 28 March 2005 Nias Earthquakes from GPS Static Offsets, BSSA. 97. 1A. S86–S102. doi:10.1785/0120050609.

Bettadpur, S., 2003. Level-2 gravity field product user handbook, GRACE 327-734. CSR Publ. GR-03-01, 17 pp, Univ. Of Texas at Austin, Austin, Texas.

Bettadpur, S., 2007. CSR level-2 processing standards document for product release 04 GRACE. 327-742.

Bindoff, N.L. et al., 2007. Observations: Oceanic Climate Change and Sea Level. In: Climate Change 2007, The Physical Science Basis. Contribution of Working Group I to the Fourth Assessment Report of the Intergovernmental Panel on Climate Change, Cambridge Univ. Press, Chap.5.

Cazenave, A., Dominh, K., Guinehut, S., Berthier, E., Llovel, W., Ramillien, G., Ablain, M., Larnicol, G., 2009. Sea level budget over 2003-2008: A reevaluation from GRACE space gravimetry, satellite altimetry and Argo, Global and Planetary Change, 65, 1-2, 83–88, DOI: 10.1016/j.gloplacha.2008.10.004.

Chambers, D.P., 2006. Observing seasonal steric sea level variations with GRACE and satellite altimetry, J. Geophys. Res., 111, C03010, doi:10.1029/2005JC002914.

Chao, B.F., 2005. On inversion for mass distribution from global (time-variable) gravity field. J. Geodynamics 39, 223-230. doi:10.1016/j.jog.2004.11.001.

Chao, B.F., Wu, Y.H., Li, Y.S., 2008. Impact of Artificial Reservoir Water Impoundment on Global Sea Level. Science, 320. 5873. 212–214. doi:10.1126/science.1154580.

Chen, J.L., Tapley, B.D., Wilson, C.R., 2006. Alaskan Mountain Glacial Melting Observed by Satellite Gravimetry. Earth Planet. Sci. Lett. 248, 368-378. doi: 10.1016/j.epsl.2006.05.039.

Chen, J.L., Wilson, C.R., Famiglietti, J.S., Rodell, M., 2007a. Attenuation Effects on Seasonal Basin-Scale Water Storage Change From GRACE Time-Variable Gravity, J. Geodesy. 81. 4. 237-245. 10.1007/s00190-006-0104-2.

Chen, J.L., Wilson, C.R., Tapley, B.D., Blankenship, D., Ivins, E., 2007b. Patagonia Icefield Melting Observed by GRACE, Geophys. Res. Lett., Vol. 34, No. 22, L22501, 10.1029/2007GL031871.

Chen, J.L., Wilson, C.R., Tapley, B.D., Grand, S., 2007c. GRACE Detects Coseismic and Postseismic Deformation from the Sumatra-Andaman Earthquake, Geophys. Res. Lett. 34. 13. L13302 10.1029/2007GL030356

Cheng, M., Ries, J., 2007. GRACE Technical Note no.5: Monthly estimates of C20 from 5 SLR satellites. (http://podaac.jpl.nasa.gov/grace/documentation.html).

Choosakul, N., Saito, A., Iyemori, T., Hashizume, M., 2009. Excitation of 4-min periodic ionospheric variations following the great Sumatra-Andaman earthquakes in 2004, J. Geophys. Res., 114. A10313, doi:10.1029/2008JA013915, 2009.

Cox, C.M, Chao, B.F., 2002. Detection of large-scale mass redistribution inthe terrestrial system since 1998, Science, 297, 831-833.

Crowley, J.W., Mitrovica, J.X.., Bailey, R.C., Tamisiea, M.E., Davis, J.L., 2006. Land water storage within the Congo Basin inferred from GRACE satellite gravity data. Geophys. Res. Lett. 33, L19402, doi:10.1029/2006GL027070.

Cummins, P.R., Hirano, S., Kaneda, Y., 1998. Refined coseismic displacement modeling for the 1994 Shikotan and Sanriku-oki earthquakes. Geophys. Res. Lett. 25, 3219-3222.

de Linage, C., et al., 2009. Separation of coseismic and postseismic gravity changes for the 2004 Sumatra-Andaman earthquake from 4.6 yr of GRACE observations and modelling of the coseismic change by normal-modes summation. Geophys. J. Int. 176. 695–714. doi: 10.1111/j.1365-246X.2008.04025.x

de Viron, O., Panet I., Mikhailov, V., Van Camp, M., Diament, M., Retrieving earthquake signature in grace gravity solutions. 2008. Geophys. J. Int. 174. 1. 14–20 doi:10.111/j.1365-264X.2008.03807.x

Dingman, S.L., 2002. Physical Hydrology. Second Edition, Prentice-Hall, New Jersey, 646pp.

Fukuda, M., 1994. Methane flux from thawing Siberian permafrost (ice complexes) results from field observation. Eos, Trans. Am. Geophys. Union 75-86.

Garcia, D., Chao, B.F., Del Rio, J., Vigo I., Garcia-Lafuente, J., 2006. On the steric and mass-induced contributions to the annual sea level variations in the Mediterranean Sea, J. Geophys. Res. 111, C09030. doi:10.1029/2005JC002956.

Hamon, R.W., 1963. Computation of direct runoff amounts from storm rainfall. Int. Assoc. Sci. Hydrology, Publication 63.

Han, S.C., Shum, C.K., Bevis, M., Ji, C., Kuo, C.Y., 2006. Crustal dilatation observed by GRACE after the 2004 Sumatra-Andaman earthquake. Science 313, 658-666. doi:10.1126/science.1128661.

Hasegawa, T., Fukuda, Y., Fu, G., Sun, W., Tanaka, Y., Yamamoto, K., 2009. Gravity Changes Associated with the 2004 Sumatra-Andaman earthquake - Comparison between GRACE and SNRVEI model. JPGU 2009. D106-005. Abstract.

Hashimoto, M., Choosakul, N., Hashizume, M., Takemoto, S., Takiguchi, T., Fukuda, Y., Fujimori, K., 2006. Crustal deformations associated with the great Sumatra-Andaman earthquake deduced from continuous GPS observation, Earth Planets Space. 58. 127–139.

Heki, K., Miyazaki, S., Tsuji, H., 1997. Silent fault slip following an interplate thrust earthquake in the

Japan Trench. Nature 386, 595-597.

Heki, K., Otsuka, Y., Choosakul, N., Hemmakorn, N., Komolmis, T., Maruyama, T., 2006. Detection of ruptures of Andaman fault segments in the 2004 Great Sumatra Earthquake with coseismic ionospheric disturbances. J. Geophys. Res. 111, B09313, doi:10.1029/2005JB004202.

Heki, K., 2007. http://www.ep.sci.hokudai.ac.jp/ heki/pdf/Phys_inter.pdf

Hirata, K., Satake, K., Tanioka, Y., Kuragamo, T., Hasegawa, Y., Hayashi, Y., Hamada, N., 2006. The 2004 Indian Ocean tsunami: Tsunami source model from satellite altimetry. Earth Planets Space 58, 195-201.

Hu, Y., Wang, K., He, J., Klotz, K., Khazaradze, G.,2004. Three-dimensional viscoelastic finite element model for postseismic deformation of the great 1960 Chile earthquake. J. Geophys. Res. 109, B12403, doi:10.1029/2004JB003163.

Hughes, K. L., Masterlark, T., Pore pressure recovery and coulomb stress evolution following the 2004 M9.2 Sumatra-Andaman Earthquake, 2009 AGU Fall Meeting, T23B-1923, Abstract.

Iijima, Y., Fedorov, A. N., Park, H., Suzuki, K., Yabuki, H., Maximov, T. C., Ohata, T., 2009. Abrupt Increases in Soil Temperatures following Increased Precipitation in a Permafrost Region, Central Lena River Basin, Russia. Permafrost and Periglac. Process. doi: 10.1002/ppp.662

Imanishi, Y., Sato, T., Higashi, T., Sun, W., Okubo, S., 2004. A Network of Superconducting Gravimeters Detects Submicrogal Coseismic Gravity Changes. Science. 306. 5695. 476–478. doi:10.1126/science.1101875.

Imanishi, Y., Tamura, Y., Ikeda, H., Okubo, S., 2009. Permanent gravity changes recorded on superconducting gravimeters from earthquakes in central Japan - The Noto Hantou and Niigataken Chuetsu-oki events in 2007. J. Geodynamics. 48. 3–5. 260–268. doi:10.1016/j.jog.2009.09.013.

Ishii, M., Shearer, P. M., Houston, H., Vidale, J. E., 2005. Extent, duration and speed of the 2004 Sumatra-Andaman earthquake imaged by the Hi-Net array, 435, 7044, 933–936. doi:10.1038/nature03675.

Iwamori, H.,1998. Transportation of H2O and melting in subduction zones. Earth Planet. Sci. Lett. 160,

65-80.

Jekeli, C., 1981. Alternative methods to smooth the Earth's gravity field. Department of Geodetic Science and Surveying, Ohio State University, Columbus.

Jonsson, S., Segall, P., Pedersen, R., Bjornsson, G.,2003. Post-earthquake ground movements correlated to pore-pressure transients. Nature 424, 179-183.

Kaula, W.M., 1966. Theory of Sattelite Geodesy, applications of satellites to Geodesy, Blaisdell Publishing Company.

Kazama, T., Okubo, S., 2009. Hydrological modeling of groundwater disturbances to observed gravity: Theory and application to Asama Volcano, Central Japan, J. Geophys. Res., 114, B08402, doi:10.1029/2009JB006391.

Kelley, K.A., Plank, T., Grove, T.L., Stolper, E.M., Newman, S., Hauri, E.,2006, Mantle melting as a function of water content beneath back-arc basins. J. Geophys. Res. 111, B09208, doi:10.1029/2005JB003732.

Lemke, P., et al., 2007. Observations: Changes in Snow, Ice and Frozen Ground. In: Climate Change 2007,The Physical Science Basis. Contribution of Working Group I to the Fourth Assessment Report of the Intergovernmental Panel on Climate Change. Cambridge Univ. Press, Chap.4.

Luthcke, S. B., Zwally, H. J., Abdalati, W., Rowlands, D. D., Ray, R. D., Nerem, R. S., Lemoine, F.G., McCarthy, J. J., Chinn, D. S., 2006. Recent Greenland ice mass loss by drainage system from satellite gravity observations. Science 314, 1286-1289. doi:10.1126/science.1130776.

Matsuo, K., Heki, K., 2010. Time-variable ice loss in Asian high mountains from satellite gravimetry, Earth Planet. Sci. Lett. 290, 30-36, doi:10.1016/j.epsl.2009.11.053, 2010.

Morishita, Y., Heki, K., 2008. Characteristic precipitation patterns of El Nino/La Nina in time-variable gravity fields by GRACE. Earth Planet. Sci. Lett. 272, 677–682. doi:10.1016/j.epsl.2008.06.003.

Nawa, K., Suda, N., Fukao, Y., Sato, T., Aoyama, Y., Shibuya, K., 1998. Incessant excitation of the Earth's free oscillations, Earth Planets Space, 50, 3-8.

Nawa, K., Suda, N., Yamada, I., Miyajima, R., Okubo, S., 2009. Coseismic change and precipitation effect in temporal gravity variation at Inuyama, Japan: A case of the 2004 off the Kii peninsula earthquakes observed with superconducting gravimeter. J. Geodynamics. 48. 1. 1–5. doi:10.1016/j.jog.2009.01.006.

Nerem, R. S., Chao, B. F., Au, A. Y., Chan, J. C., Klosko, S. M., Pavlis, N. K., Williamson, R. G., 1993. Temporal variations of the Earth's gravitational field from satellite laser ranging to Lageos. Geophys. Res. Lett., 20(7), 595–598.

Nur, A., Booker, J.R., 1972. Aftershocks caused by pore fluid flow? Science 175, 885-887.

Okada, Y., 1992. Internal deformation due to shear and tensile faults in a half-space. Bull. Seism. Soc. Am. 82, 1018-1040.

Ogawa, R., and Heki, K., 2006. On the Non-seasonal Gravity Changes From GRACE and Velocities of GPS Stations, Journal of the Geodetic Society of Japan, Vol. 52, No. 4, pp297-208.

Ogawa, R., Heki, K., 2007. Slow postseismic recovery of geoid depression formed by the 2004 Sumatra-Andaman Earthquake by mantle water diffusion. Geophys. Res. Lett. 34, L06313. doi:10.1029/2007GL029340.

Oki, T., Musiake, K., Matsuyama, H., Masuda, K., 1995. Global atmospheric water balance and runoff from large river basins. Hydrol. Proc. 9, 655-678. doi: 10.1002/hyp.3360090513.9.

Panet et al., 2007. Coseismic and post-seismic signatures of the Sumatra 2004 December and 2005 March earthquakes in GRACE satellite gravity, Geophys. J. Int. 171. 1. 177–190. doi:10.1111/j.1365-246X.2007.03525.x

Papa, F., Prigent, C., Rossow, W.B., 2008. Monitoring Flood and Discharge Variations in the Large Siberian Rivers From a Multi-Satellite Technique. Surv. Geophys. 29:297-317. doi:10.1007/s10712-008-9036-0.

Park, J., et al., 2005. Earth's Free Oscillations Excited by the 26 December 2004 Sumatra-Andaman Earthquake. 308, 5725, 1139–1144. doi:10.1126/science.1112305.

Peltier. W.R. 2004. Global Glacial Isostasy and the Surface of the Ice-Age Earth: The ICE-5G(VM2)

Model and GRACE, Earth Planet. Sci., 32. 111-149. doi:10.1146/annurev.earth.32.082503.14435

Penman, H.L., 1948. Natural evaporation from open water, bare soil, and grass. Royal Society of London Proceedings, Series A, 193:120-145.

Peterson B.J., Homes, R.M., McClelland, J.W., Vorosmarty, C.K., Lammers, R.B., Shiklomanov, A.I., Shiklomanov, I.A., Rahmstorf, S., 2002. Increasing River Discharge to the Arctic Ocean. Science. 298.

Pollitz, F. F., Banerjee, P., Burgmann, R., Hashimoto, M., Choosakul, N., 2006. Stress changes along the Sunda trench following the 26 December 2004 Sumatra-Andaman and 28 March 2005 Nias earthquakes, Geophys. Res. Lett., 33, L06309, doi:10.1029/2005GL024558.

Rodell, M. and Houser, P. R., Jambor, U., Gottschalck, J., Mitchell, K., Meng, C.J., Arsenault, K., Cosgrove, B., Radakovich, J., Bosilovich, M., Entin, J.K., Walker, J.P., Lohmann, D., Toll, D., 2004. The Global Land Data Assimilation System. Bull. Am. Meteorol. Soc. 85, 381–394.

Saito, M., 1983. http://wwwsoc.nii.ac.jp/geod-soc/contents/book/program.html

Steffen, H., Gitlein, O., Denker, H., Muller, J., Timmen, L., 2009. Present rate of uplift in Fennoscandia from GRACE and absolute gravimetry. Tectonophysics. 474, 69-77. doi:10.1016/j.tecto.2009.01.012 474.

Strassberg, G., Scanlon, BR., Rodell, M., 2007. Comparison of seasonal terrestrial water storage variations from GRACE with groundwater-level measurements from the High Plains Aquifer (USA) G, VOL. 34, L14402, doi:10.1029/2007GL030139.

Sugimoto, A., Yanagisawa, N., Naito, D., Fujita, N., Maximov, T.C., 2002. Importance of permafrost as a source of water for plants in east Siberian taiga. Ecological Research. 17. 493–503.

Sugimoto, A. et al., 2003. Characteristics of soil moisture in permafrost observed in East Siberian taiga with stable isotopes of water. Hydrol. Process. 17. 1073–1092. doi:10.1002/hyp.1180.

Swenson, S., Wahr, J., 2002. Methods for inferring regional surface-mass anomalies from Gravity Recov-

ery and Climate Experiment (GRACE) measurements of time-variable gravity, J. Geophys. Res., 107(B9), 2193, doi:10.1029/2001JB000576.

Swenson, S., Wahr, J., 2006. Post-processing removal of correlated errors in GRACE data. Geophys. Res. Lett. 33, L08402. doi:10.1029/2005GL025285.

Swenson, S., Wahr, J., 2007. Multi-sensor analysis of water storage variations of the Caspian Sea. Geophys. Res. Lett. 34, L16401. doi:10.1029/2007GL030733.

Syed, T.H., Famiglietti, J.S., Rodell, M., Chen, J., Wilson, C.R., 2008. Analysis of terrestrial water storage changes from GRACE and GLDAS. Water Resour. Res. 44, W02433.　doi:10.1029/2006WR005779.

Tamisiea, M. E., Mitrovica, J.X., Davis, J.L., 2007. GRACE gravity data constrain ancient ice geometries and continental dynamics over Laurentia. Science 316, 881-883. doi:10.1126/science.1137157.

Tanioka, Y., Yudhicara, Kusunose, T., Kathiroli, S., Nishimura, Y., Iwasaki, S., Satake, K., 2006. Rupture process of the 2004 great Sumatra-Andaman earthquake estimated from tsunami waveforms. Earth Planets Space 58, 203-209.

Tapley, B.D., Bettadpur, S., Ries, J.C., Thompson, P.F., Watkins, M.M., 2004. GRACE measurements of mass variability in the earth system. Science 305, 503-505. doi: 10.1126/science.1099192.

Thornthwaite, C. W., Mather, J. R. 1955. The Water Balance. Publications in Climatology, 8, No. 1. centerton, NJ: Lab. of climatology.

Velicogna, I., Wahr, J., 2006. Acceleration of Greenland ice mass loss in spring 2004. Nature 443, 329-331. doi:10.1038/nature05168.

Vigny, C., Simons, W.J.F., Abu, S., Bamphenyu, R., Satirapod, C., Choosakul, N., Subarya, C., Socquet, A., Omar, K., Abidin, H.Z., Ambrosius, B.A.C., 2005. Insight into the 2004 Sumatra-Andaman earthquake from GPS measurements in southeast Asia. Nature 436, 201-204.

Wahr, J., Molenaar, M., Bryan, F., 1998. Time variability of the Earth's gravity field: Hydrological and oceanic effects and their possible detection using GRACE. J. Geophys. Res. 103, 30205-30229.

Yang, D., Ye, B., Kane, D. L., 2004. Streamflow changes over Siberian Yenisei River Basin, Journal of Hydrology, Volume 296, Issues 1-4, 20 August 2004, 59-80, 0022-1694, doi:10.1016/j.jhydrol.2004.03.017.

Ye, B., Yang, D., Zhang, Z., Kane, D.L., 2009. Variation of hydrological regime with permafrost coverage over Lena Basin in Siberia. J. Geophys. Res., 114. D07102. doi:10.1029/2008JD010537.

Yoder, C.F., Williams, J.G., Dickey, J.O., Schutz, B.E., Eanes, B.J., Tapley, B.D., 1983. Seular variation of the Earth's gravitational Harmonic J_2 coefficient from Lageos and non tidal acceleration of Earth rotation, Nature 303, 757-762.

Zhang, Z.Z., Chao, B.F., Lu, Y., Hsu, H.T., 2009. An effective filtering for GRACE time-variable gravity: Fan filter. Geophys. Res. Lett. 36, L17311. doi:10.1029/2009GL039459.